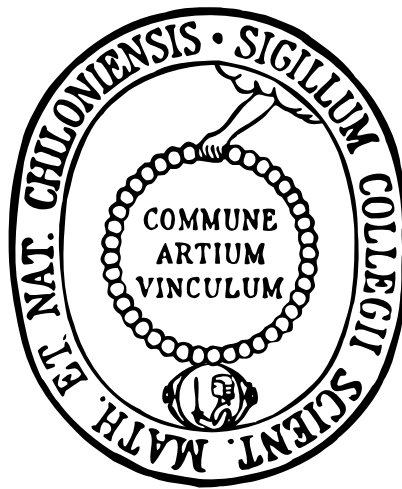# ENERGY SPECTRA OF NEAR RELATIVISTIC GALACTIC COSMIC RAYS AND SOLAR ENERGETIC PARTICLES

-

EXTENDING THE MEASUREMENT CAPABILITIES OF EPHIN

Dissertation
zur Erlangung des Doktorgrades
der Mathematisch-Naturwissenschaftlichen Fakultät
der Christian-Albrechts-Universität zu Kiel
vorgelegt von

PATRICK KÜHL

– Kiel, Juli 2017 –

ABSTRACT

Measurements of the energy spectra of particles in the heliosphere are of major importance in order to understand basic physical acceleration and transport processes. Furthermore, understanding their temporal variations is crucial with regard to their impact in dosimetry for future manned space missions. The two main components of particles in the heliosphere with energies above 100 MeV are the sporadic Solar Energetic Particle (SEP) events and Galactic Cosmic Rays (GCR), which have their intensity and energy spectrum modulated by the Sun on time scales of up to several years. Both, SEP and GCR spectra have been measured for decades by various space instruments below 100 MeV and by indirect ground-based observations sensitive to energies above several GeV. Recently, the Alpha Magnetic Spectrometer (AMS) and the Payload for Antimatter Matter Exploration and Light-nuclei Astrophysics (PAMELA) have provided measurements from several hundreds of MeV to higher energies with unprecendented precision. The energy range between 100 MeV and the energy range of AMS and PAMELA, however, remains poorly covered by space instrumentation. Furthermore, magnetospheric effects as well as the limited mission time of these instruments restrict the use of AMS and PAMELA data for the heliosheric astroparticle community.

In this work, the observable energy range of the Electron Proton Helium Instrument (EPHIN) onboard the Solar and Heliospheric Observatory (SOHO) was increased with detailed simulations of the instrument and its response to energetic particles. Since the developed method can be applied to data already taken by the instrument, energy spectra for protons between 100 MeV and above 1 GeV were derived for the entire SOHO mission and therefore significantly extend the available data sets for SEP events and GCRs in terms of energy and time coverage. The new measurement capabilities have been implemented for the high energy component of SEP events [see Kühl et al., 2015a, 2017] and the solar modulation of GCRs [see Kühl et al., 2015c, 2016]. For both particle populations, the systematic uncertainties of the method were evaluated and the results have been compared to various other missions.

The annual proton spectra from 1995 to 2014 have been derived in an energy range from 250 MeV up to 1.6 GeV and discussed with a focus on drift effects. Furthermore, the possibility to apply the new method to Helium and heavy ions has been examined.

SEP events have been investigated by statistical means utilizing the continous measurements from EPHIN. For this purpose, the SEP events with an increase in the intensity of protons above energies of 500 MeV which occured between 1995 and 2015 have been identified. The spectral properties of these events have been calculated and analysed with special emphasis on whether or not the event has been detected by ground-based instruments, i.e. Neutron Monitors (NMs).

ZUSAMMENFASSUNG

Messungen der Energiespektren von Teilchen in der Heliosphäre sind wichtig um sowohl deren Beschleunigungs- und Transportprozesse zu untersuchen als auch den Beitrag dieser Teilchen zur Strahlungsdosis zukünftiger bemannter Raumfahrtmissionen abschätzen zu können. Die beiden Hauptkomponenten von Teilchen in der Heliosphäre mit Energien über 100 MeV sind die unregelmäßig auftretenden solaren energiereichen Teilchen (SEP) Ereignisse und die Galaktische Kosmische Strahlung (GCR), deren Intensität und Energiespektrum durch die solare Modulation auf Zeitskalen von bis zu mehreren Jahren beinflusst wird. Diese Teilchen wurden unterhalb von 100 MeV von zahlreichen Instrumenten auf Raumsonden und über mehreren GeV indirekt auf dem Erdboden gemessen. Die Instrumente Alpha Magnetic Spectrometer (AMS) und Payload for Antimatter matter Exploration and Light-nuclei Astrophysics (PAMELA) lieferten erstmals präzise Messungen im Energiebereich von mehreren 100 MeV aufwärts. Durch magnetosphärische Effekte und die geringe Missionsdauer dieser Instrumente ist ihr Nutzen für die heliosphärische Astroteilchenphysik jedoch begrenzt.

In dieser Arbeit wurde der Energiebereich des Electron Proton Helium Instruments (EPHIN) auf dem Solar and Heliospheric Observatory (SOHO) mittels Simulationen des Instrumentes und dessen Ansprechverhalten auf energiereiche Teilchen signifikant erweitert. Da sich die entwickelte Method auf bereits gemessene Daten des Instrumentes anwenden lässt, wird der Datensatz über SEP Ereignisse und die GCRs dadurch im Hinblick auf Energie- und Zeitabdeckung signifikant erweitert.

Mittels der entwickelten Methode können Energiespektren von Protonen von 100 MeV bis über 1 GeV für die gesamte SOHO Mission (und damit mehr als 20 Jahre) berechnet werden.

Auf Basis dieser erweiterten Messfähigkeiten wurden energiereiche SEP Ereignisse [Kühl et al., 2015a, 2017] und die solare Modulation der GCR [Kühl et al., 2015c, 2016] untersucht. Für beide Teilchenpopulationen wurden die systematischen Unsicherheiten mittels Simulationen und Vergleichen mit anderen Missionen untersucht.

In den GCR Studien wurden die jährlichen Proton Spektren vom 1995 bis 2014 in einem Energiebereich von 250 MeV bis 1.6 GeV berechnet und Drifteffekte an Hand dieser Daten untersucht. Außerdem wurde untersucht, in wie weit sich die entwickelte Methode auf Helium und schwere Ionen erweitern lässt.

SEP Ereignisse wurden in einer statistischen Analyse untersucht. Hierfür wurden alle Ereignisse mit einem Intensitätsanstieg von Protonen über 500 MeV zwischen 1995 und 2015 identifiziert. Die spektralen Eigenschaften dieser Ereignisse wurden dann berechnet und analysiert, insbesondere im Hinblick darauf, ob ein Ereignis auch von Instrumenten auf dem Erdboden, im speziellen Neutronen Monitoren (NM), gemessen wurde.

PUBLICATIONS: PEER REVIEWED JOURNALS

Proton Intensity Spectra During the Solar Energetic Particle Events of May 17, 2012 and January 6, 2014

P. Kühl, S. Banjac, N. Dresing, R. Goméz-Herrero, B. Heber, A. Klassen and C. Terasa, Astronomy & Astrophysics, Volume 576, id. A120, 9 pp. (2015), DOI: 10.1051/0004-6361/201424874   Own contribution: 80%

Annual Cosmic Ray Spectra from 250 MeV up to 1.6 GeV from 1995 – 2014 Measured with the Electron Proton Helium Instrument onboard SOHO

P. Kühl, R. Goméz-Herrero and B. Heber, Solar Physics, Volume 291, Issue 3, pp.965-974 (2016), DOI: 10.1007/s11207-016-0879-0   Own contribution: 90%

Solar Energetic Particle Events with Protons Above 500 MeV Between 1995 and 2015 Measured with SOHO/EPHIN

P. Kühl, N. Dresing, B. Heber and A. Klassen, Solar Physics, Volume 292, Issue 1, art. id.10, 13 pp. (2017), DOI: 10.1007/s11207-016-1033-8 Own contribution: 85%

Cosmic Ray Transport in Heliospheric Magnetic Structures. I. Modeling Background Solar Wind Using the CRONOS Magnetohydrodynamic Code

T. Wiengarten, J. Kleimann, H. Fichtner, P. Kühl, A. Kopp, B. Heber and R. Kissmann, The Astrophysical Journal, Volume 788, id. 80, 16 pp. (2014), DOI: 10.1088/0004-637X/788/1/80   Own contribution: 10%

Cosmic-Ray Transport in Heliospheric Magnetic Structures. II. Modeling Particle Transport through Corotating Interaction Regions

A. Kopp, T. Wiengarten, H. Fichtner, F. Effenberger, P. Kühl, B. Heber, J.-L. Raath and M. S. Potgieter, The Astrophysical Journal, Volume 837, id. 37, 9 pp. (2017), DOI: 10.3847/1538-4357/aa603b   Own contribution: 5%

PUBLICATIONS: CONFERENCE PROCEEDINGS

Extended Measurement Capabilities of the Electron Proton Helium Instrument aboard SOHO - Understanding Single Detector Count Rates

P. Kühl, S. Banjac, B. Heber, J. Labrenz, R. Müller-Mellin and C. Terasa, Central European Astrophysical Bulletin, Vol. 39, p. 119-124 (2015)

Own contribution: 60%

Galactic Cosmic Ray Quiet Time Spectra from 300 MeV up to Above 1 GeV Measured with SOHO/EPHIN

P. Kühl, N. Dresing, J. Gieseler, B. Heber and A. Klassen, Proceedings of Science, ICRC2015, id. 224   Own contribution: 90%

Simultaneous Analysis of Recurrent Jovian Electron Increases and Galactic Cosmic Ray Decreases

P. Kühl, N. Dresing, P. Dunzlaff, H. Fichtner, J. Gieseler, R. Goméz-Herrero, B. Heber, A. Klassen, J. Kleimann, A. Kopp, M. Potgieter, K. Scherer and R. D. Strauss, Central European Astrophysical Bulletin, Vol. 37, p. 643-648 (2013)

Own contribution: 60%

Spectrum of Galactic and Jovian Electrons

P. Kühl, N. Dresing, P. Dunzlaff, F. Effenberger, H. Fichtner, J. Gieseler, R. Goméz-Herrero, B. Heber, A. Klassen, J. Kleimann, A. Kopp, M. Potgieter, R. D. Strauss and T. Wiengarten, Proceedings of the 33rd International Cosmic Rays Conference, Vol. 5, p. 3480-3484 (2013)

Own contribution: 70%

Forbush Decreases Associated to Stealth Coronal Mass Ejections

B. Heber, C. Wallmann, D. Galsdorf, K. Herbst, P. Kühl, M. Dumbovic, B. Vršnak, A. Veronig, M. Temmer, C. Müstl and S. Dalla, Central European Astrophysical Bulletin, Vol. 39, p. 75-82 (2015)

Own contribution: 30%

Proton Energy Spectra During Ground Level Enhancements as Measured by EPHIN aboard SOHO

B. Heber, N. Dresing, K. Herbst, A. Klassen, P. Kühl and R. Goméz-Herrero, Proceedings of Science, ICRC2015, id. 119

Own contribution: 30%

GEANT 4 Simulation of the Helios Cosmic Ray Telescope E6: Feasibility of Chemical Composition Studies

J. Marquardt, B. Heber, M. Hörlöck, P. Kühl and R. F. Wimmer- Schweingruber, Journal of Physics: Conference Series, Volume 632, Issue 1, article id. 012016 (2015)

Own contribution: 10%

The Chemical Composition of Galactic Cosmic Rays During Solar Minimum of Solar Cycle 20/21 - Helios E6 Results

J. Marquardt, B. Heber, P. Kühl, and R. F. Wimmer-Schweingruber, Proceedings of Science, ICRC2015, id. 123

Own contribution: 10%

Jovian Electrons In The Inner Heliosphere: A Parameter Study On Intensity Profiles Near Earth

A. Vogt, P. Dunzlaff, B. Heber, A. Kopp, P. Kühl, and D. T. Strauss, Proceedings of Science, ICRC2015, id. 207

Own contribution: 10%

Improved 3He/4He Isotope Separation in EPHIN Data Based on Simulations

C. Berndt, B. Heber, S. Banjac and P. Kühl, Proceedings of Science, ICRC2015, id. 207

Own contribution: 75%

EPHIN Anisotropy Measurement Capability

S. Banjac, R. Goméz-Herrero, B. Heber, P. Kühl and C. Terasa, Journal of Physics: Conference Series, Volume 632, Issue 1, article id. 012048 (2015)

Own contribution: 10%

CONTENTS

ACRONYMS

AMS	Alpha Magnetic Spectrometer
ACE	Advanced Composition Explorer
AU	Astronomical Unit
BESS	Balloon-borne Experiment with Superconducting Spectrometer
CIR	Co-rotating Interaction Region
CME	Coronal Mass Ejection
COSTEP	Comprehensive Suprathermal and Energetic Particle Analyzer
EPHIN	Electron Proton Helium Instrument
FD	Forbush Decrease
FFS	Force-Field Solution
GCR	Galactic Cosmic Rays
GOES	Geostationary Operational Environmental Satellites
GLE	Ground Level Enhancement
HMF	Heliospheric Magnetic Field
IMP8	Interplanetary Monitoring Platform-8
LIS	Local Interstellar Spectrum
NM	Neutron Monitor
PAMELA	Payload for Antimatter Matter Exploration and Light-nuclei Astrophysics
SOHO	Solar and Heliospheric Observatory
SEP	Solar Energetic Particle

INTRODUCTION

1.1 HELIOSPHERIC ASTROPARTICLE PHYSICS

Since the discovery of Cosmic Rays by Hess [1912], many space-borne, balloon- and ground-based experiments have greatly increased our astrophysical knowledge and understanding by measuring particles in the solar system with energies ranging from a few keV up to the ZeV range (10^{21}eV). The broad energy range suggests that the observed particles are accelerated at different sources and by various physical processes as illustrated in Fig. 1.

Galactic Cosmic Rays (GCR) are accelerated at supernova remnants [e.g. Blasi, 2013] and measured with energies within the MeV range up to ZeV. While the GCR flux outside of the heliosphere is considered to be constant over time, measurements in the inner heliosphere reveal temporal variations anticorrelated with the solar activity [Heber and Potgieter, 2006; Heber et al., 2006]. Understanding the physical processes responsible for the solar modulation of GCRs - for the first time described theoretically by Parker [1958, 1959] - is one of the main aspects of heliospheric astroparticle physics.

The second major topic in the field are Solar Energetic Particle (SEP) events. These sporadic increases in the particle intensity by several orders of magnitude in the energy range up to above 1 GeV are related to magnetic reconnection in solar flares and shock acceleration in Coronal Mass Ejections (CMEs) [e.g. Reames, 2013].

Pick-up ions are neutral atoms from the local interstellar medium or of heliospheric origin that are ionized by solar photons (for the most part in the *UV* range) or due to charge exchange in the inner heliosphere before being picked up by the solar wind. In the classical picture these ions are transported to the heliospheric termination shock by the solar wind, where they are accelerated by diffusive shock acceleration to energies up to 5-100 MeV/nucleon [Drake et al., 2010]. Undergoing the same transport processes as GCR, these anomalous cosmic rays can be observed in the inner heliosphere. Note that recent measurements of the Voyager spacecraft have challenged that classical picture regarding the acceleration site and processes [Stone et al., 2005, 2008].

Particle acceleration is also possible in planetary magnetospheres. The most prominent example are jovian electrons forming one of the main contributions to the observed electron intensities in the energy range of 0.2 to 25 MeV [Heber et al., 2007]. Studies regarding jovian electrons and their energy spectra have been performed in the scope of this work and are published in Kühl et al. [2013b,a]; Vogt et al. [2015]. Furthermore, acceleration can occur in the interplanetary medium. The interaction of a fast solar wind stream with a preceding slow stream can create Co-rotating Interaction Regions (CIRs). These structures with varying plasma parameter can not only influence the propagation of energetic particles but also
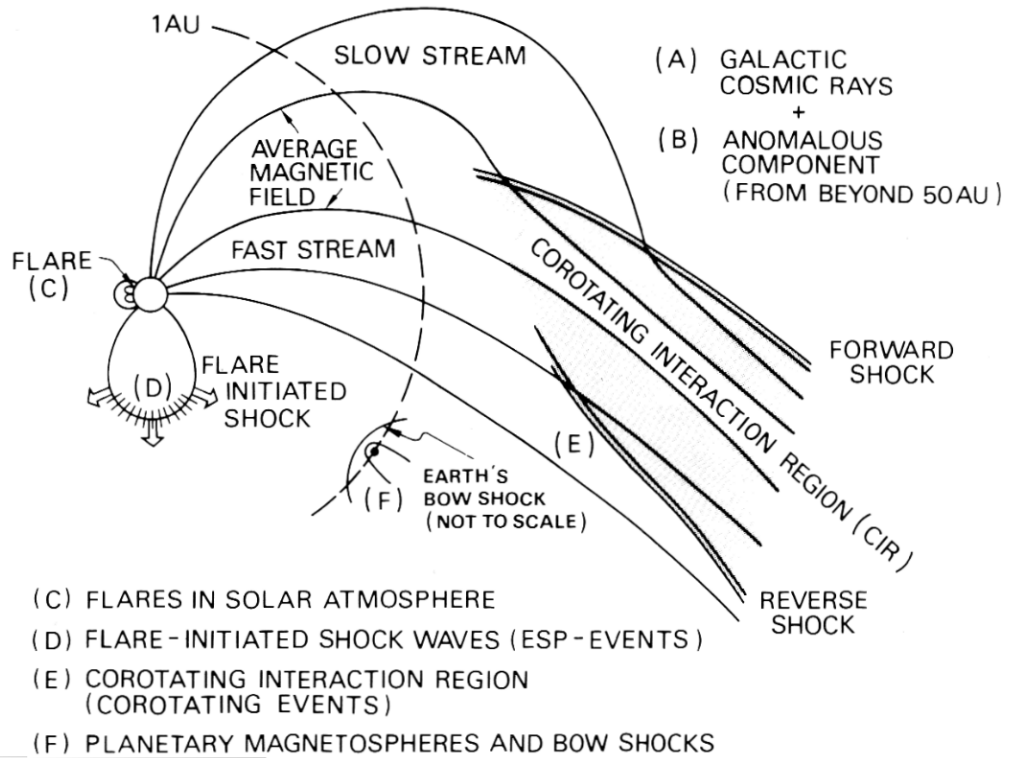
Figure 1: Sketch of the various particle populations in the heliosphere (taken from Kunow et al. [1991]).

accelerate particles to energies of above 1 MeV/nucleon via shock acceleration [Fisk and Lee, 1980]. In the scope of this work, CIRs and their influence on the propagation of energetic particles have been studied and published in Wiengarten et al. [2014]; Kopp et al. [2017].

The large energy range as well as the different sources and acceleration processes indicate the complexity of heliospheric astroparticle physics and the different field of physics related to it. Of special interest are the acceleration of the different particle populations and their propagation through the heliosphere for which various parameters such as charge states, isotopic and elemental compositions, anisotropies and the energy spectra are measured. The latter has proven to be one of the most valuable tools since the spectral shape can be directly related to acceleration processes [Giacalone and Neugebauer, 2008] and transport effects such as adiabatic cooling [Moraal, 2013].

1.2 MOTIVATION OF THIS THESIS

In recent years, the next generation of astroparticle instruments like the Alpha Magnetic Spectrometer (AMS) [Aguilar et al., 2015] and the Payload for Antimatter Matter Exploration and Light-nuclei Astrophysics (PAMELA) [Adriani et al., 2013] have started a new era of astroparticle physics with measurements of unprecedented precision and energy coverage. While being primarily designed for the search of dark matter and the investigation of high energy physics, their measurements in the energy range from several hundreds of MeV up to several GeV are of significant scientific value for the heliospheric astroparticle community, particularly regarding the energy spectra of the solar modulated GCRs as well as SEP events. However, the instrumental design as well as their position in the Earth's magnetosphere restrict the measurements to relatively high energies. Since the majority of interplanetary particle instruments are limited to energies below 100 MeV, the intermediate energy range is poorly explored with the exception of some instruments like the Interplanetary Monitoring Platform-8 (IMP8) and the Geostationary Operational Environmental Satellites (GOES) that provide only very limited capabilities to bridge this energy gap.

It is the aim of this thesis to extend the energy range of the Electron Proton Helium Instrument (EPHIN) aboard the Solar and Heliospheric Observatory (SOHO) to higher energies to further bridge this gap in the energy regime from 100 MeV to 1 GeV. This extended energy range allows to compare and intercalibrate EPHIN with AMS and PAMELA at high energies as well as various measurements below 100 MeV and to provide the community with continuous measurements over the entire cosmic ray energy range.

In particular, the data of EPHIN was measured continuously over more than 20 years and can be used for studies on how the solar modulation does affect the GCR spectrum. Especially our knowledge and understanding of the heliospheric drift effects depend on the availability of long-term observations since they are related to the polarity of the Heliospheric Magnetic Field (HMF) that changes with a periodicity of two solar cycles ($\sim$ 22 years).

Furthermore, an extension of the energy range of EPHIN provides new insights on SEP events with particles accelerated to several hundreds of MeV. While most high energy SEP event studies are focussed on describing individual events, it is possible to perform statistical analysis of multiple measured particle spectra based on the continuous data from EPHIN.

Last but not least, the SOHO mission has one distinct advantage with respect to AMS and PAMELA which is its orbit around the Lagragian point 1 well outside of the Earth's magnetosphere. While the main objectives of AMS and PAMELA (dark matter and cosmic rays with energies above several tens of GeV) are not influenced by the magnetosphere due to their high rigidity, the deflection gets more and more important with decreasing energy. Therefore both missions can only measure particles at lower energy during orbit periods of high latitude where particles can enter the magnetosphere over the magnetic poles with lower rigidity. Due to this reduction in statistics and/or time resolution certain features of SEP events such as the velocity dispersion can not be observed in detail. EPHIN

Instrument	AMS-02	PAMELA	EPHIN
mass	7500 kg	470 kg	3.55 kg
dimensions	500 x 400 x 300 cm^3	height: 130 cm	35 x 22 x 19 cm^3
power consumption	2500 W	355 W	1.85 W
averaged data rate	10 Mbit/sec	1.4 Mbit/sec	172 bit/sec
geometry factor	4500 cm^2 sr	21.5 cm^2 sr	4.5 cm^2 sr
proton energy range	0.5 - 2000 GeV	0.08 - 700 GeV	5 - 53 MeV
spacecraft	ISS	Resurs DK1	SOHO
altitude	$\approx$ 400 km	350-600 km	$1.5 \cdot 10^6$ km (L1)
launch date	May 2011	Jun 2006	Dec 1995

Table 1: Comparison between the AMS-02 [Kountine, 2012; Bindi, 2015], PAMELA [Picozza et al., 2007] and EPHIN [Müller-Mellin et al., 1995] instruments.

aboard SOHO on the other hand is free of these limitations and can not only complement measurements of these missions for SEP studies but investigate the transport of particles through the magnetosphere in combined studies.

In order to extend the energy range for EPHIN, it is necessary to develop a method that identifies the particle type and total energy of particles with energies above 50 MeV/nucleon. Furthermore the response of the instrument to these particles has to be derived in order to calculate the physical intensity rather than a simple count rate.

The challenges for such an extension are obvious when comparing the instrumental and engineering properties of AMS and PAMELA to EPHIN as presented in table 1. It is obvious that EPHIN is a different class of instrument than AMS, with differences of more than three orders of magnitudes regarding not only the mass, power consumption and data rate but also the geometrical response of the instrument. Note that the entire SOHO spacecraft with its mass of 610 kg is still ten times lighter than the AMS instrument.

However, recent studies have shown that the measurement capabilities of EPHIN can be extended by utilizing sophisticated GEANT4 simulations of the instrument and its response to energetic particles. Kühl et al. [2015b] have shown that the very high count rates of each individual detector (up to 25000 counts/minute) can be used in order to investigate small intensity variations such as Forbush Decreases (FDs) with high time resolution as well as GCR modulation. In a similar approach, Curdt and Fleck [2015] have used the engineering data of the SOHO spacecraft itself as records of GCRs and SEP events. Furthermore, Banjac et al. [2015] have shown that the pitch-angle distribution of particles measured by EPHIN can be derived using the segmentation of the first two detectors and a magnetic field measurement from the Advanced Composition Explorer (ACE) [Stone et al., 1998] extrapolated to SOHO.

ENERGETIC PARTICLES IN THE HELIOSPHERE

2.1 GALACTIC COSMIC RAYS

Galactic Cosmic Rays (GCR) are energetic particles, which consist of mainly protons with about 10 % fraction of helium nuclei and small abundances of heavier elements, electrons and positrons with energies within the MeV range up to $\approx 10^{21}$ eV. The main acceleration process for energies up to 10^{15} eV is shock acceleration in super nova remnants [Blasi, 2013]. Although the GCR flux in the Galaxy is considered to be constant over time, it is well known that at energies below 30 GeV the flux in the heliosphere is anti-correlated with the 11-year and 22-year solar-activity cycle due to solar modulation [e.g. Heber and Potgieter, 2006; Heber et al., 2006; Lifter et al., 2002].

Fig. 2 shows the count rate of the Kiel Neutron Monitor (NM) and the monthly averaged sunspot number. NMs measure secondary particles created by interactions of GCRs in the Earth's atmosphere and are often used as proxy for the overall GCR intensity because they provide continuous measurements over several decades. As shown, a clear anti-correlation between the NM count rate and the sunspot number, which itself is a proxy for the solar activity, is present. Besides these 11-year variations, an influence of drift effects depending on the Heliospheric Magnetic Field (HMF) polarity (indicated by the coloured background, cf. Krainev and Kalinin [2014]) can be observed: While the count rate in A^- cycles features a sharp maximum, a plateau-like shape can be observed in A^+ cycles. The relevant processes of the solar modulation can be described by the helio-
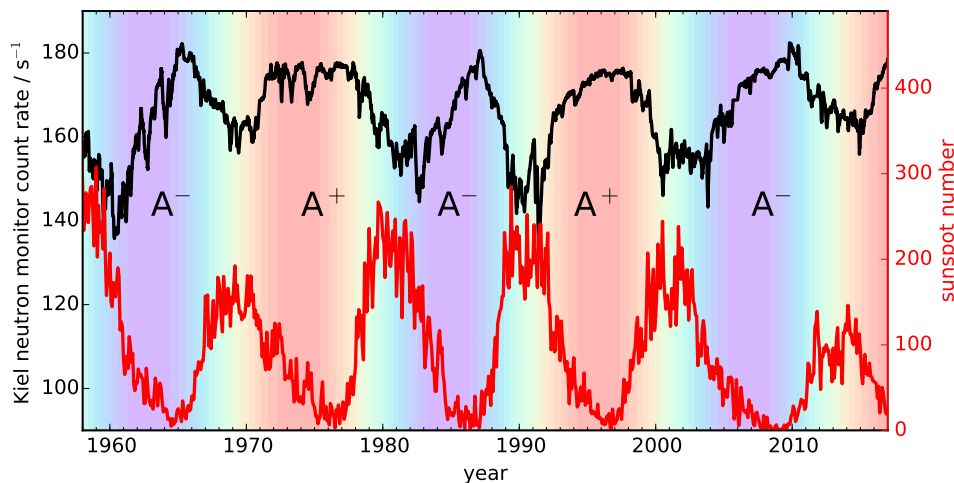
Figure 2: Count rate of the Kiel NM (black, left hand axis, http://www.nmdb.eu/) and monthly smoothed sunspot number (red, right hand axis, http://sidc.oma.be/silso/datafiles) over more than five decades. The coloured background indicates the polarity of the HMF (A^+ and A^-).

spheric transport equation first derived by Parker [1965], which is based on the equations of motion of charged particles in fluctuating magnetic fields and on the assumption of an isotropic GCR flux. In a rewritten form by Potgieter [2013] this equation reads:

$$\underbrace{\frac{\partial f}{\partial t}}_{a} = -(\underbrace{\mathbf{V}}_{b} + \langle \mathbf{v}_d \rangle) \cdot \nabla f - \underbrace{\nabla \cdot (\mathbf{K}_s \cdot \nabla f)}_{d} + \underbrace{\frac{1}{3}(\nabla \cdot \mathbf{V})\frac{\partial f}{\partial \ln P}}_{e}, \tag{1}$$

where $f(\mathbf{r}, P, t)$ is the GCR distribution function depending on rigidity P, time t and the position in the heliosphere $\mathbf{r}$. Since a solar rotation ($\sim$ 28 days) and the travel time of a solar wind parcel to the edge of the heliosphere ($\sim$ 1 year) are sufficiently smaller than the time-scales of the solar activity ($\sim$ 11 years), a steady-state solution with $\partial f/\partial t = 0$ (part a) is often considered. The remaining terms describe the convection depending on the solar wind velocity $\mathbf{V}$ (part b), drift effects due to gradient and curvature drifts in the global HMF resulting in the averaged particle drift velocity $\langle \mathbf{v}_d \rangle$ [Webber and Lockwood, 1988] (part c), diffusion given by the symmetrical diffusion tensor $\mathbf{K}_s$ (part d) and the adiabatic energy change (part e). Since it is not possible to solve the equation analytically, the majority of theoretical studies address the solar modulation by means of simulations [e.g. Jokipii and Kopriva, 1979; Le Roux and Potgieter, 1995; Manuel et al., 2011].

A simplified approximation of the modulated GCR spectra is the Force-Field Solution (FFS) as first derived by Gleeson and Axford [1967, 1968b], which gives reasonable results for energies above 150 MeV [Gleeson and Urch, 1973]. With the neglection of drift effects, the estimation of the adiabatic deceleration with the Compton-Getting effect [Gleeson and Axford, 1968a] and the assumption of a radial symmetric heliosphere as well as no local sources of GCRs, the intensity J of a particle type i with a kinetic energy T is given by

$$J_i(T, \Phi) = J_{LIS,i}(T + \Phi)\frac{T(T + 2E_{0,i})}{(T + \Phi)(T + \Phi + 2E_{0,i})}. \tag{2}$$

$J_{LIS,i}$ represents the Local Interstellar Spectrum (LIS), i.e. the spectrum outside of the heliosphere. Although the latest results of the Voyager mission were able to reduce uncertainties about the modulation volume (i.e. the size of the heliosphere) as well as the LIS [Stone et al., 2013], it is important to note that the choice of a LIS model can have a significant effect on the results [see Herbst et al., 2010, 2017].

The modulation function $\Phi = (Ze/A)\phi$, with Z, A being the charge and mass number of the particle, is proportional to the so-called Force-Field parameter ϕ, which itself correlates with the solar activity with typical values withing the range of 100-2000 MV [Usoskin et al., 2011]. Assuming that the rigidity (P) and radial distance (r) dependency of the diffusion coefficient is separable in the form

$$\kappa(r, P) \propto \kappa_1(r)\kappa_2(P) \tag{3}$$

and that the rigidity dependence can be estimated with
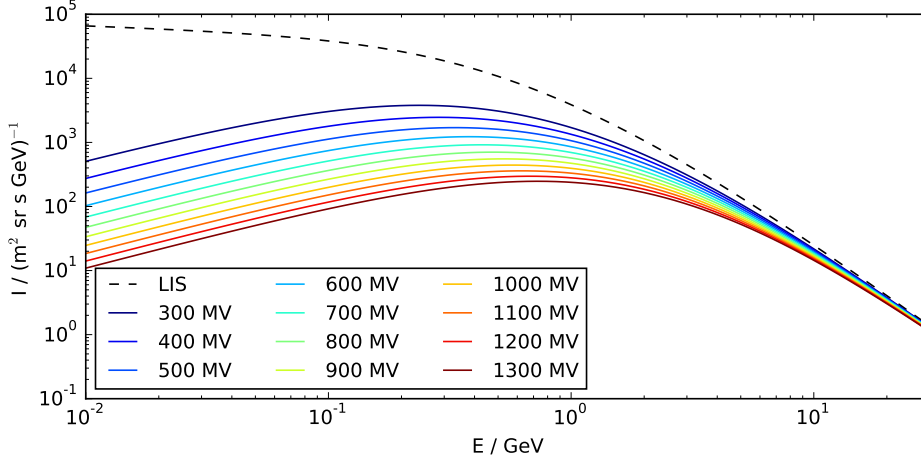
$$\kappa_2(P) \propto P \tag{4}$$

Figure 3: The proton LIS given by Burger et al. [2000] and the modulated spectra near the Earth approximated with the FFS for various modulation potentials ϕ.

the modulation potential ϕ is given by

$$\phi(r) = \int_r^{r_b} \frac{V(r')}{3\kappa_1(r')} dr' \qquad (5)$$

with $V(r)$ being the solar wind velocity. While the heliospheric boundary r_b can be considered to be either the solar wind termination shock (≈ 90 Astronomical Unit (AU)) or the heliosheath, the lower boundary is mostly set to Earth (1 AU) since the majority of FFS studies is based on measurements performed near the Earth. A comprehensive review of the derivation of the FFS can be found in Caballero-Lopez and Moraal [2004, and references therein].

In Fig. 3 the resulting modulated spectra of Eq. 2 are shown for protons, using the LIS given by Burger et al. [2000]. While the variation of the intensity at lower energies ($10 < E < 300$ MeV) can be as large as two orders of magnitude, the intensity at high energies ($E \gg 10$ GeV) is barely modulated at all.

The simplicity of the FFS is both, the main advantage and disadvantage of the method. For various applications, describing the modulated GCR spectra near the Earth with just a single parameter ϕ for a given particle type and LIS is quite convenient, i.e. for the study of cosmogenic nuclides [Matthiä et al., 2013; Herbst et al., 2017] or radiation doses caused by GCRs [Mertens et al., 2013]. However, neither drift effects nor local modulation due to either CIRs or CMEs can be described by the FFS. Furthermore, Corti et al. [2016] found that the rigidity dependency of the diffusion coefficient is more complex than what is assumed in Eq. 4 .

In recent years, the spectrum of GCRs has been measured by next generation particle detectors such as AMS [Alcaraz et al., 2000], AMS-02: [Aguilar et al., 2015] and PAMELA [Adriani et al., 2013] in space as well as by various balloon campaigns like Balloon-borne Experiment with Superconducting Spectrometer (BESS) [Shikaze et al., 2007] and BESS-Polar [Abe et al., 2015]. While the high precision and large energy range of these instruments represent new challenges for solar modulation models [Potgieter et al., 2014], they do not provide continuous observations over the 22-year HMF cycle, which is important in order to understand the role of drift effects.

2.2 SOLAR ENERGETIC PARTICLES

In contrast to the continuous flux of GCRs which varies on time scales of several years, the particle intensity in the interplanetary medium can increase by several orders of magnitude within several minutes during Solar Energetic Particle (SEP) events. The events are more likely to occur during solar maximum [Nymmik, 1999] and can consist of various particle species which are accelerated near the Sun from supra thermal (few keV) up to relativistic (few GeV) energies [Desai and Giacalone, 2016].

Wild et al. [1963] were the first to propose two different acceleration processes for SEPs, currently believed to be magnetic reconnection during solar flares and shock acceleration at Coronal Mass Ejection (CME) -driven shocks [Reames, 2013; Cliver, 2016]. In the following, an introduction to the basic concepts of both event classes and the related particle observations is given. For a more detailed review the reader is referred to Reames [1996, 1999, 2013]; Kallenrode [2003], a comprehensive historical review is given by Shea and Smart [1990].

The left panel of Fig. 4 shows remote sensing observations of the Sun at a wavelength of 195 Å from the *Extreme Ultraviolet Imaging Telescope* [EIT, Delaboudinière et al., 1995] on board SOHO measured on July 14th, 2000. In the center of the disk, a solar flare can be observed as a point source with such a high photon intensity that the signal overflows to adjacent pixels. Solar flares are related to magnetic reconnection processes in the low solar corona. The majority of the particles accelerated in these structures remain confined, causing characteristic photon emissions in the X-ray and UV range lasting for several minutes to hours as they are decelerated while streaming into regions of denser plasma. A fraction of the accelerated particles, however, can escape the acceleration region along open magnetic field lines, streaming into the interplanetary medium. The composition of these particles is typically electron- and iron-rich with a large ^{3}He/^{4}He ratio due to resonant wave-particle interaction in the acceleration region [Cane and Richardson, 2003].
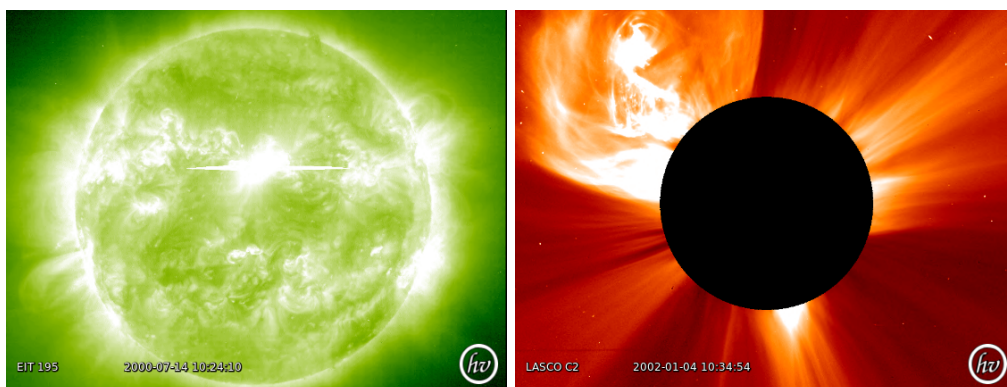

Figure 4: Left: A flare observed near the center of the solar disc on July 14th, 2000 with the SOHO/EIT instrument at a wavelength of 195 Å. Right: A CME observed on January 4th, 2002 with the SOHO/LASCO C2 white-light coronograph (structure in the upper left corner). Both images have been created with https://helioviewer.org.
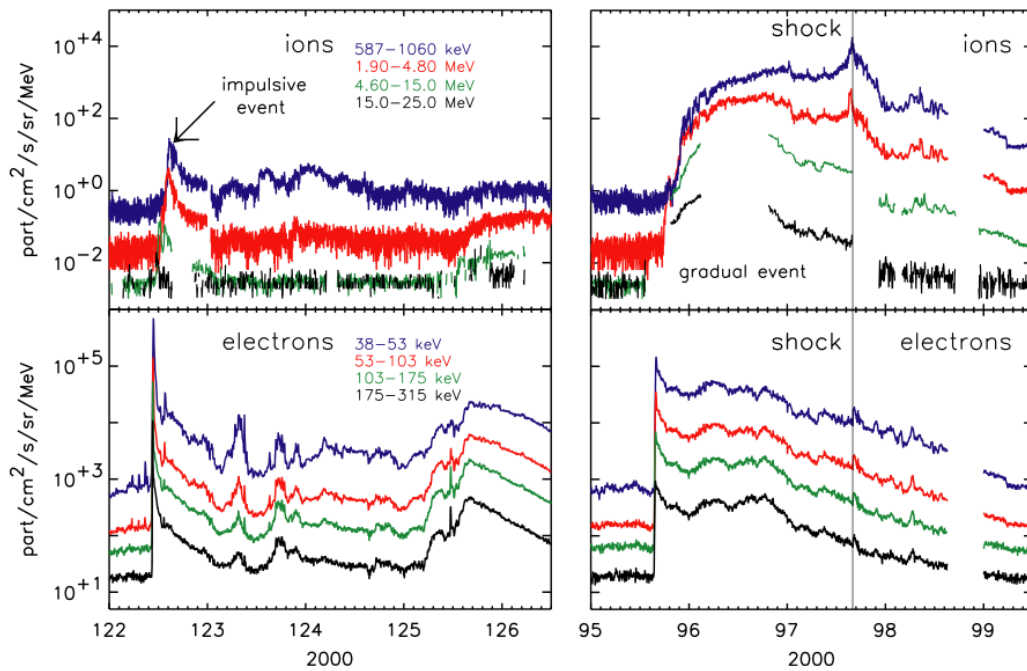
Figure 5: Intensity-time profiles of ions and electrons for an impulsive (left) and a gradual event (right) as measured by ACE/EPAM. Figure taken from Lario [2005].

The second major acceleration process is shock acceleration at CME driven shocks [Webb and Howard, 2012]. The right panel of Fig. 4 shows a white-light coronographic image taken by the *Large Angle and Spectrometric Coronagraph* C2 [LASCO, Brueckner et al., 1995] of a CME on January 4th, 2002. The measured photon intensity is dominated by Thomson scattering by free electrons and hence the figure can be interpreted as a line of sight integration of the electron density [Quémerais and Lamy, 2002]. The intensity increase in the top-left corner can be identified as a CME. During the expansion of the CME in the interplanetary medium, shocks at which particles can be accelerated efficiently can be formed.

Due to the different acceleration mechanisms and regions, the flare- and CME-related SEPs differ not only in their composition but in their intensity-time profiles. Typical examples of both events can be seen in the panels of Fig. 5. In the left panel an SEP event related to a solar flare is shown. An impulsive increase in both, proton and electron intensities, that lasts for several hours is observable. In the right panel, a SEP event is shown that is caused by a CME with a gradual increase in the proton intensity and a maximum of particles when the shock passes the spacecraft, indicating a persistent acceleration of particles. Due to these measurements, flare and CME related events are often referred to as impulsive and gradual events, respectively.

However, it has to be noted that this textbook classification does not reflect the reality of all SEP events since fast CMEs are often associated with flares. Furthermore, a variation from event to event is also probable. Hence, distinguishing the different contributions for a single event can be rather difficult, especially considering that the injection into and the transport in the interplanetary medium of the SEPs has to be taken into account as well [Lario, 2005]. In order to disen-

	Impulsive	Gradual
Particles:	Electron-Rich	Proton-Rich
^{3}He/^{4}He	~1	~0.0005
Fe/O	~1	~0.1
H/He	~10	~100
Duration	Hours	Days
Events/Year	~1000	~10

Table 2: Main characteristics of impulsive and gradual SEP events in comparison (adapted from Cliver [2009]).

tangle these different effects, the combination of remote-sensing observation and in-situ measurements is necessary [Cliver, 2009]. For the latter, the investigation of the elemental composition of an event is of major importance as indicated by Table 2. Here some of the main characteristics of both event types are summed up. As can be seen, measurements of the ^{3}He to ^{4}He ratio or the Iron to Oxygen ratio can be used to distinguish between both event types. Another important measurement is the energy spectra of the particles, which are directly related to the acceleration process [e.g. Tripathi et al., 2013]

One specific subclass of SEP events are those with sufficient intensity increases at high energies such that their resulting cascades of secondary particles in the Earth's atmosphere result in an increase in the count rate of NMs. Due to the continuous measurements of NMs, these so-called Ground Level Enhancements (GLEs) have been measured for more than seven decades with the first one already reported in 1946 by Forbush [1946]. In total 71 GLEs have been observed by now, an average of one GLE per year with a higher likelihood during solar maximum conditions. The biggest GLE observed occured on February 23, 1956 [Reames, 2013] and while it has been found that the majority of GLEs are related to gradual SEPs events [Reames, 1999], Aschwanden [2012] points out that "*the question arises about the location of the responsible acceleration site: coronal flare reconnection sites, coronal CME shocks, or interplanetary shocks*".

A valuable tool to shed some light on this discussion is the study of the energy spectra of GLEs. Although simulation-based calculations of the SEP energy spectrum from NM measurements have been proven to be possible [Mishev et al., 2014], the results are rather difficult to interpret due to the fact that the count rate of NMs is not only influenced by the Earth's magnetic field itself [Lockwood and Debrunner, 1999] but is also found to be sensitive to the arrival direction of particles due to deflection by the magnetosphere [Shea and Smart, 1990]. Hence, direct measurements of the energy spectra of a statistical sample of GLEs are necessary.

Recent measurements from PAMELA [Bazilevskaya et al., 2013] and AMS [Bindi, 2015] have shown the high energy component of SEP spectra with unprecedented precision. However, due to the rare occurrence of SEPs with energies near or even above 1 GeV, continuous measurements over several decades are necessary in order to obtain a larger sample of events.

MEASUREMENT TECHNIQUES

3.1 ENERGY LOSS IN MATTER

Energetic particles deposit a fraction of their kinetic energy during the passage of dense matter due to various processes depending on their initial energy. Figure 6 shows the stopping power (i.e. the differential energy loss divided by the density of the target material) of positive muons in copper. Indicated by the verticle lines are the energies at which different processes dominate. For a wide range of energies ($0.05 < \beta\gamma < 500$), the dominating process is the excitation and ionization of the target material due to inelastic scattering with electrons of the target's atoms. Since the analysis in this thesis focuses on protons in the energy range from 5 MeV ($\beta \cdot \gamma \approx 0.1$) up to 1600 MeV ($\beta \cdot \gamma \approx 2.5$), other processes are not discussed and the reader is referred to the comprehensive review of all processes given by Longair [1992].

Although the energy loss caused by inelastic scattering is a stochastic process [Landau, 1944], the average energy loss can be derived based on the momentum transfer of the projectile to the electrons of the target atom as first described by Bethe [1930]. The derivation is based on fundamental work from Bohr [1913, 1915] and has been later improved by Bloch [1933] resulting in the Bethe-Bloch equation. Further corrections have been described by Weaver and Westphal [2002] and a detailed review of the calculations is given by Fano [1963].
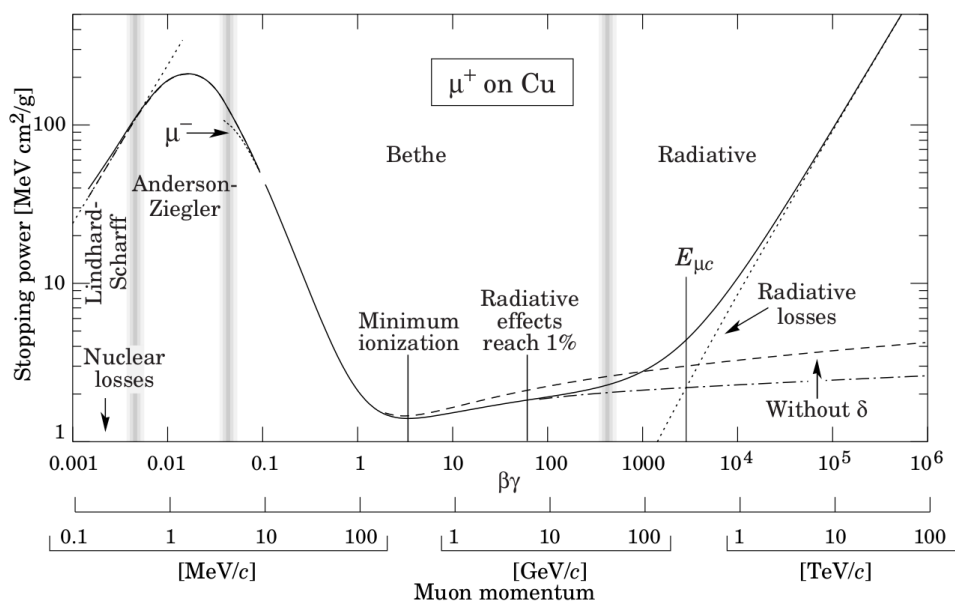

Figure 6: Stopping power for positive muons in copper as function of $\beta\gamma$=p/Mc [fig. 27.1 in Nakamura and Particle Data Group, 2010]

The classical, non-relativistic derivation assumes that the electrons in the material are free and at rest. Furthermore, it is assumed that the projectile particle is not deflected since its mass is significantly larger than the mass of the electrons. Note that the latter assumption as well as the neglected Bremsstrahlung are the main reasons why electrons can not be described by the Bethe-Bloch equation.

The momentum transfer of a particle with charge ze, mass m and velocity v passing an electron in the target material at the distance of b is given by

$$\Delta p = \int F dt = q \int E'_\perp \frac{dt}{dx} dx = \frac{q}{v} \int E_\perp dx = \frac{2ze^2}{bv}. \tag{6}$$

Only the perpendicular component of the electric field $E'_\perp$ has been considered while the components parallel to the direction of movement have been neglected since they are canceled out for symmetry reasons. The last conversion uses the divergence theorem. Based on this equation the energy transfer as a function of the impact parameter b is

$$\Delta E(b) = \frac{(\Delta p)^2}{2m_e} = \frac{2z^2 e^4}{m_e b^2 v^2} \tag{7}$$

For the energy loss all electrons with an impact parameter between b and $b + db$ have to be considered taking into account the electron density N_e:

$$-dE(b) = \Delta E(b) N_e dV = \Delta E(b) N_e 2\pi b\, db\, dx = \frac{4\pi z^2 e^4}{m_e v^2} N_e \frac{db}{b} dx \tag{8}$$

Integrating over the impact parameter from b_{min} to b_{max} results in

$$-\frac{dE}{dx} = \frac{4\pi z^2 e^4}{m_e v^2} N_e \ln\left(\frac{b_{max}}{b_{min}}\right) \tag{9}$$

Based on the maximum impuls transfer of a central collision ($\Delta p = 2m_e v$) the minimal impact parameter is found to be $b_{min} = \frac{ze^2}{m_e v^2}$. Requiring the minimal energy transfer to equal the mean excitation potential of the material I defines $b_{max} = \sqrt{\frac{2}{m_e I}} \frac{ze^2}{v}$. With these boundaries, Eq. 9 translates to the non-relativistic Bethe-Bloch equation:

$$-\frac{dE}{dx} = \frac{2\pi z^2 e^4}{m_e v^2} N_e \ln\left(\frac{2m_e v^2}{I}\right) \tag{10}$$

Taking into account relativisitic and quantum mechanical effects [Longair, 1992], the Bethe-Bloch equation reads

$$-\frac{dE}{dx} = \frac{4\pi}{m_e c^2} \cdot \frac{N_e z^2}{\beta^2} \cdot \left(\frac{e^2}{4\pi\epsilon_0}\right)^2 \cdot \left(\ln\left(\frac{2m_e c^2 \beta^2}{I \cdot (1 - \beta^2)}\right) - \beta^2\right), \tag{11}$$

The electron density described by

$$N_e = \frac{z_t \cdot \rho}{a_t \cdot u} \tag{12}$$

adds material constants such as the target's density ρ as well as the target's charge and mass number z_t and a_t respectively.
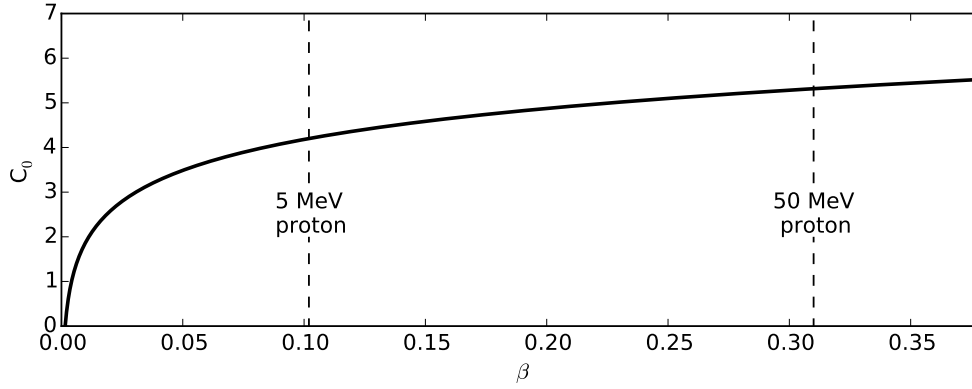
Figure 7: C_0 (defined in equation 13) as function of β derived for silicon (I=172 eV).

Apart from the target's material, the differential energy loss dE/dx also depends on the projectile's charge z and velocity $\beta = v/c$ allowing the identification of particles using an appropriate detector set-up that can measure the differential as well as the total energy loss with the dE/dx-E method.
 The method is based on the assumption that

$$C_0 := \left(\ln \left(\frac{2m_e c^2 \beta^2}{I \cdot (1 - \beta^2)} \right) - \beta^2 \right) \tag{13}$$

is constant for non-relativistic particles. Figure 7 presents C_0 as a function of the projectile's velocity β. The vertical lines show β for protons with an energy of 5 and 50 MeV, respectively. Since the actual energy loss of a particle is a stochastic process with a Landau distribution, the variation of C_0 is negligible in this energy range. Hence, for a given target material and for particles in this velocity range we find

$$dE/dx \propto \frac{z^2}{\beta^2} \propto \frac{z^2}{v^2}. \tag{14}$$

For non-relativistic particles the kinetic energy of the particle is given by

$$E = \frac{1}{2} \cdot m \cdot v^2 \tag{15}$$

and hence

$$dE/dx \cdot E \propto z^2 \cdot m. \tag{16}$$

Therefore, the product of the differential energy loss and the total kinetic energy is characterized by the mass m and charge z of the detected particle for a given target material. Hence, this dE/dx-E method can be used to distinguish between different particle types. Since Eq. 16 depends not only on the charge but also on the mass of the projectile, the method can be also used to distinguish between different isotopes such as ^{3}He and ^{4}He.

3.2   THE ELECTRON PROTON HELIUM INSTRUMENT

As mentioned in Chapter 1 and 2, characteristics such as isotopic composition, energy spectra and pitch-angle distributions are necessary in order to understand the physics of SEP events (see Section 2.2) and the modulation of GCRs (see Section 2.1). For that purpose, it is the aim of particle detectors to measure these quantities. However, due to the strict limitations regarding mass and power consumption on spacecrafts, most instruments are only able to measure a set of these quantities at limited ranges such as a defined energy range or only a subset of ions. To overcome these limitations, most missions feature a set of different instruments specializing on different quantities and ranges.

The Solar and Heliospheric Observatory (SOHO) mission launched on December 2, 1995 goes beyond that idea, featuring not only a set of in-situ particle detectors but also remote sensing instrumentation [Domingo et al., 1995]. One of the in-situ instruments of the collaborative mission between ESA and NASA is the Electron Proton Helium Instrument (EPHIN) instrument [Müller-Mellin et al., 1995] as part of the Comprehensive Suprathermal and Energetic Particle Analyzer (COSTEP) detector suite. A second unit of the instrument was later installed on the *Chandra* spacecraft. A cross-section and a photograph of the EPHIN instrument are shown in Fig. 8. The instrument consists of a stack of six silicon solid state detectors (labelled *A* to *F*), with the first two detectors being segmented in order to improve the identification of different isotopes and to decrease dead-time effects during time periods of high intensities. A scintillator (*G*) is enclosing this stack as anti-coincidence, restricting particles to enter the instrument along the axis of
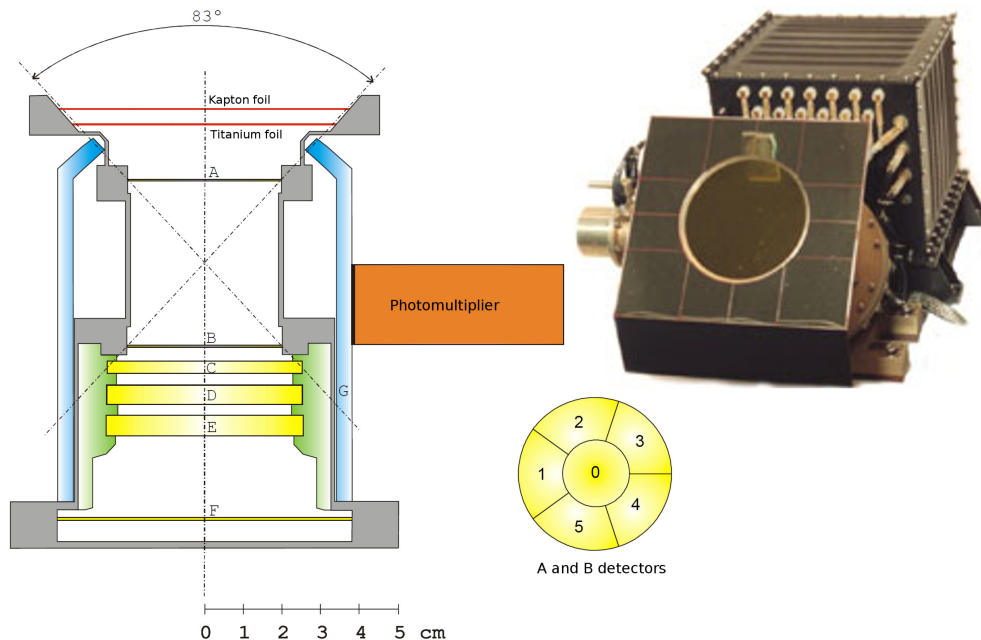

Figure 8: Sketch of the EPHIN instrument [adapted from Gómez-Herrero, 2003] (left) and a photograph of the instrument (right). The segmentation of the detectors *A* and *B* is also indicated (bottom).
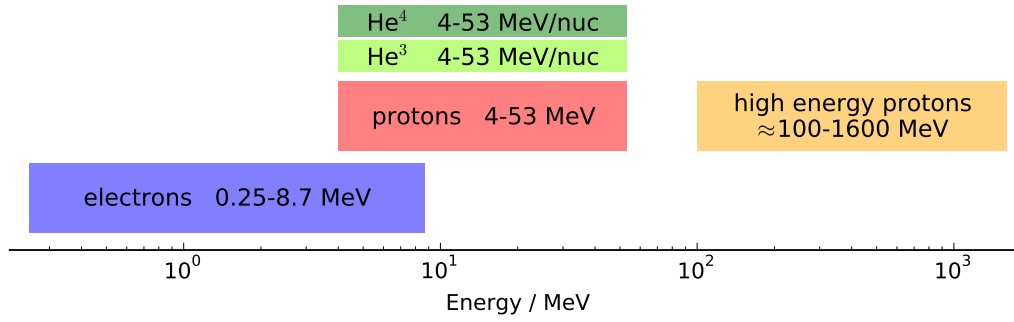
Figure 9: The nominal measurement capabilities of EPHIN for electrons (blue), protons (red) and Helium (green) taken from Müller-Mellin et al. [1995]. The energy range of high energy particles investigated in this thesis is also marked (orange).

symmetry. For the nominal measurements, particle that trigger neither the anti-coincidence G nor the detector F while at least triggering the first two detectors (A and B) are analysed in order to calculate the energy dependent intensity of electrons and protons as well as of Helium isotopes. The energy ranges for these measurements are shown in Fig. 9. The lower limits are defined by the minimal kinetic energy a particle is required to have in order to penetrate the detector A and trigger detector B. The upper limit is given by the energy at which a particle penetrates the entire detector stack and triggers detector F.

For these stopping particles, the identification of the particle is done by the dE/dx-E method (see Chapter 3.1). Since detector A of the EPHIN instrument is very thin (150μm) and the angle of incidence is limited due to the coincidence conditions (see Fig. 8), the energy deposition in this detector E_A can be considered as differential energy loss. With detector F as anti-coincidence for these measurements, the sum of the energy losses of the detectors A throughout E equals the total kinetic energy of the particle (E_{total}). The product of those quantities can thus be used as particle identification.

As an example, a histogram of the product of differential energy loss and total kinetic energy measured at October 31, 2004 is shown in Fig. 10. Note that a ^{3}He rich SEP event occured on that day, resulting in a high ^{3}He/^{4}He ratio compared to measurements of the GCR background. The shown coincidence conditions require particles to trigger detectors A and B while not reaching detector C and corresponds to energies between 4.3 and 7.8 MeV/nucleon for protons and Helium isotopes. The red, lightgreen and darkgreen vertical lines indicate the expected dE/dx-E values based on the Bethe-Bloch equation for protons, ^{3}He, and ^{4}He at energies of 7.8 MeV/nucleon, respectively. The particle populations of electrons, protons as well as different isotopes of helium (^{3}He and ^{4}He) can be clearly seen in the histogram and are in good agreement with the expected values. Note, that the histogram is more ragged at lower energies (especially at the electron peak) due to the digitalization process of the instrument.

In order to calculate the intensity of the different particle species I based on the measured count rate of this particle C, the response R of the instrument has to be taken into account. Considering a single particle type, the measured count rates
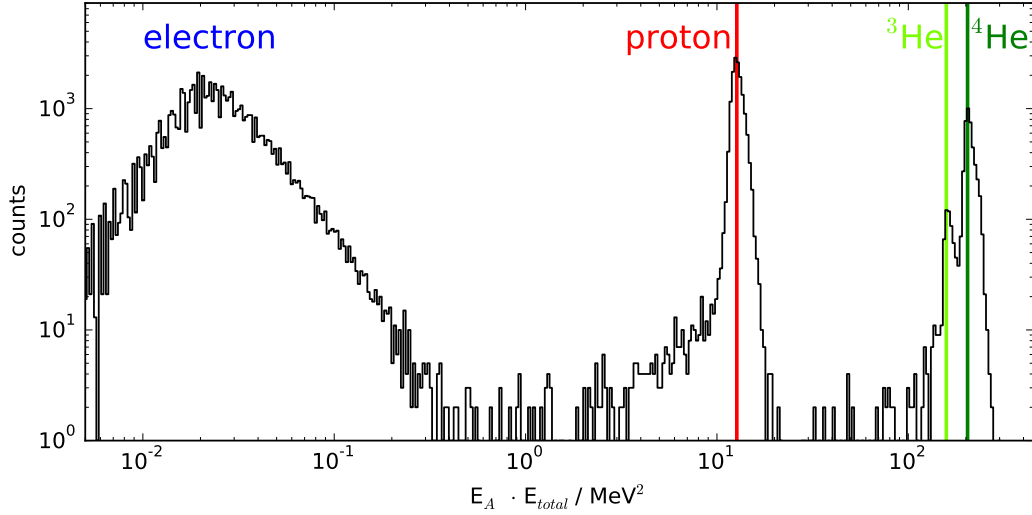
Figure 10: Histogram of the product of the energy-loss in detector A (E_A) and the total energy (E_{total}) for particles that have stopped in detector B measured at October, 31, 2004.

$c_0,..,c_n$ are related to the particles intensities at different energies $i_0,..,i_j$ via the response matrix $\mathbf{R}$:

$$
\begin{pmatrix} c_0 \\ \vdots \\ c_n \end{pmatrix} = \begin{pmatrix} r_{0,0} & .. & r_{0,j} \\ \vdots & \vdots & \vdots \\ r_{n,0} & .. & r_{n,j} \end{pmatrix} \times \begin{pmatrix} i_0 \\ \vdots \\ i_j \end{pmatrix}
\tag{17}
$$

Note that in reality, any defined coincidence has also a non-zero response for all other particles species further complicating the calculation of the intensities. For an ideal detector with $n = j$, however, the elements on the main diagonal of $\mathbf{R}$ would be constant ($r_{0,0}=r_{1,1}=...=r_{n,j}=G$) and all other elements would be zero. The constant response G is called the geometry factor of an instrument.

Based on Sullivan [1971, Eq. 9], the geometry factor of a telescope consisting of two circular detectors can be calculated via

$$
G = \frac{1}{2}\pi^2 \left(R_1^2 + R_2^2 + l^2 - ((R_1^2 + R_2^2 + l^2)^2 - 4R_1^2 R_2^2)^{1/2} \right)
\tag{18}
$$

depending on the distance between the two detectors l as well as the radii R_1, R_2 of the two detectors.

For detectors A and B of EPHIN with $R_A = R_B = 19$ mm and $l = 42.9$ mm this results in $G_{EPHIN}=5.1$ cm^2 sr. However, in order to derive the actual energy dependent response of the instrument, physical processes of the transport of energetic particles through matter such as scattering have to be considered by means of simulations and/or calibration measurements.

3.3 SIMULATIONS OF EPHIN UTILIZING GEANT4

GEANT4 [**Ge**ometry **an**d **T**racking, GEANT4 collaboration, 2006; Agostinelli et al., 2003] is a Monte Carlo simulation toolkit for the passage of energetic particles through matter including various physical processes such as electromagnetic and hadronic interactions of the particles. Due to the large number of physical processes included in the toolkit, it is widely used in the fields of high energy, nuclear and medical physics. In astroparticle physics, GEANT4 is often utilized in order to understand and improve instruments and their response to energetic particles.

For the purpose of this work, a digital replica of EPHIN including not only the geometrical but also material properties has been created. Fig. 11 shows this instrument together with simulation results of a beam of 100 protons with initial kinetic energies of 40 MeV. For purpose of clarity, any material not related to one of the detectors (e.g. the aluminium housing) is not shown in the figure, although included in the simulation. In addition to protons (blue), secondary electrons created due to interaction with the detector material are shown (red). The simulation derives the energy deposit in any defined volume, e.g. the solid state detectors (*A* to *F*) as well as the anti-coincidence scintilator (*G*) for every single particle. Furthermore, the particle source can be adopted such that the primary particles are not generated in a beam-like distribution as shown in Fig. 11 but isotropically in order to calculate response functions and to reflect the actual measurements of particles such as GCRs, which are known to be isotropically distributed in the near Earth environment [Potgieter, 2013].
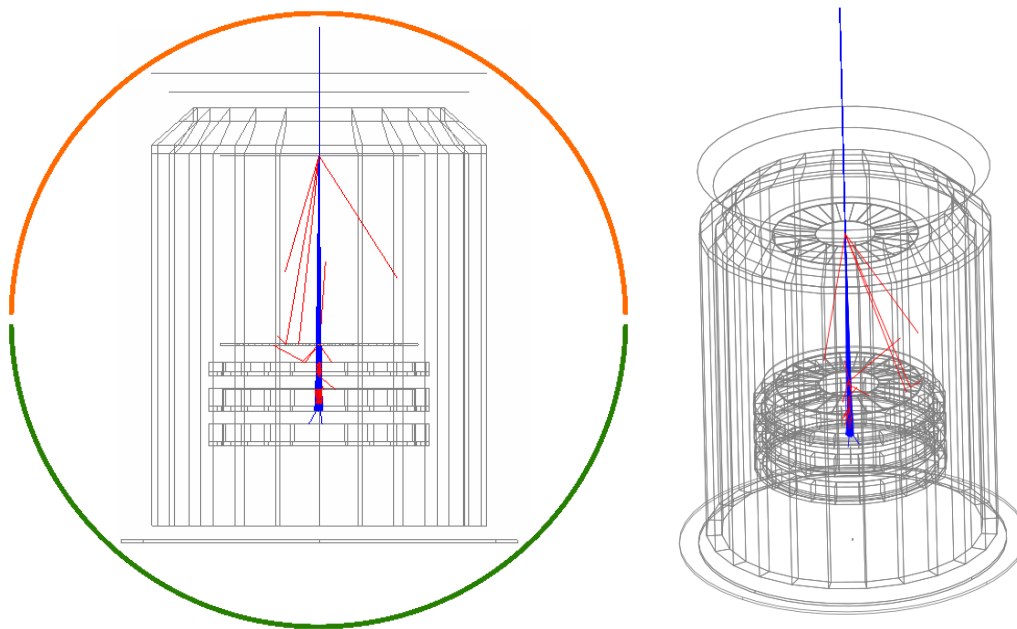

Figure 11: Left: GEANT4 simulation of a beam of 100 protons with 40 MeV in the EPHIN detector. The orange and green semicircles represent the *forward* and *backward* hemispheres, respectively; Right: 3D view of the same simulation.
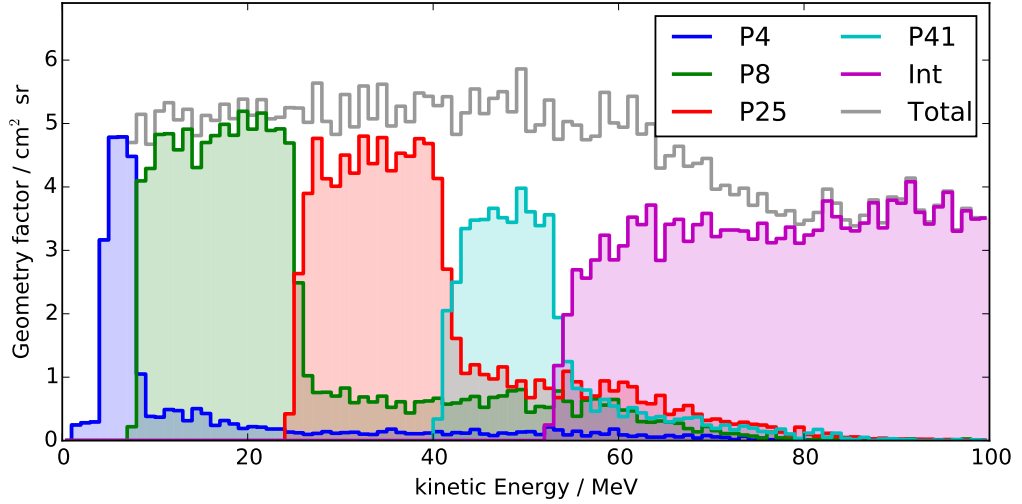
Figure 12: Energy dependent geometry factor of different coincidences for protons based on GEANT4 simulations.

Using an isotropic particle source, the geometry factor of the EPHIN instrument can be calculated by applying the different energy thresholds of the instrument [Müller-Mellin et al., 1995] for each coincidence channel to the simulated energy losses in the detectors. A particle is considered detected if it deposits more energy in a detector than the required threshold. The geometry factor G can then be calculated from the number of particles counted $n_{counted}$ [Sierks, 1997, and references therein] by

$$G = \frac{n_{counted}}{n_{simulated}} \pi A_{source} \qquad (19)$$

with the total number of particles simulated $n_{simulated}$ and the area of the source A_{source} from which particles are emitted. By simulating different particle types (e.g. electron, proton, helium) and various kinetic energies, energy dependent responses can be calculated for every particle type.

In Fig. 12, the resulting response is shown for protons and different instrumental channels. The channels P4, P8, P25 and P41 correspond to protons stopping in the B, C, D and E detector, respectively. Above $\approx$ 53 MeV, protons penetrate the entire detector stack (i.e. detector A throughout F are triggered) and are counted in the integral channel. The sum of the different channels, i.e. the response of the instrument as a whole, is also presented.

The simulation results for the P4 channel are slightly below the theoretical estimate of G_{EPHIN}=5.1 cm² sr as derived in Section 3.2. An explanation for this reduction is particle interaction in the material, especially scattering that can change the direction of a particle such that the particle does not hit a detector [Sierks, 1997]. The geometry factor of the P25 and especially the P41 are significant lower than the results for the P4 and P8. However, the total response of the instrument, i.e. the sum of all channels, remains constant since all channels feature finite responses even at higher energies, at which the particles are expected to be counted in a deeper coincidence channel. This instrumental behaviour can
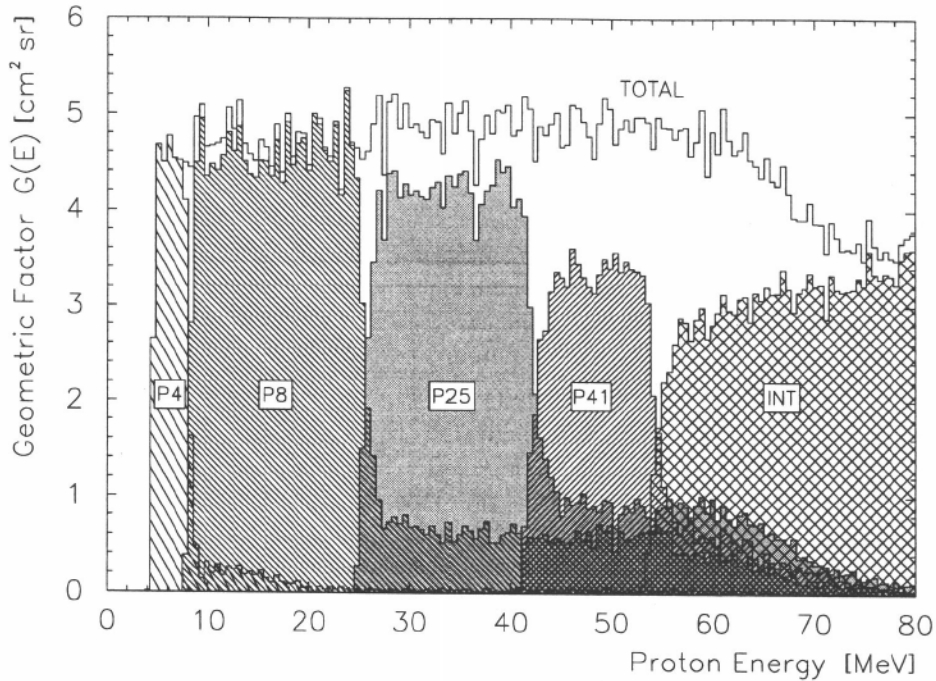
Figure 13: Energy dependent geometry factor of different coincidences for protons based on GEANT3 simulations (Fig. taken from Sierks [1997]).

be explained by the sketch of EPHIN shown in Fig. 8: Since the detectors *C*, *D* and *E* have the same radii, the opening angle of telescope geometry is getting smaller for the deeper coincidences, reducing the geometry factor. Particles with a large incidence angle with respect to the axis of symmetry of the detector can therefore also be detected in lower coincidences despite having an energy high enough to penetrate deeper than the given coincidence since their trajectory ends in the detector mounting rather than in the next detector.

The response functions in Fig. 12 are in agreement to previous GEANT3 simulations done by Sierks [1997] presented in Fig. 13, however showing minor differences in the energy range below 4 MeV. While the computations by Sierks [1997] show no particle detection below 4 MeV, the GEANT4 results indicate a small response of the EPHIN instrument due to the production of δ electrons (also referred as "knock-on electrons"). δ electrons are created when a charged particle passes through matter and "*pulls out*" the electron of the atom via coulomb interaction, providing the electron with sufficient energy to escape the potential well of the atom [Skutlartz and Hagmann, 1983]. This process was not included in the GEANT3 code but was introduced with the GEANT4 version, which could explain the differences in the simulations.

Since protons above ≈ 53 MeV are counted in the integral channel, EPHIN is in principle sensitive to protons above this energy. The integral channel, however, is also sensitive to electrons above 10 MeV and Helium particles above 55 MeV/nucleon and since the particles deposit only a fraction of their total energy in the detector, the dE/dx-E method (Sections 3.1, 3.2) can not be used to distinguish

between the different particle types. Furthermore, in contrast to particles in the stopping proton channels (P4, P8, P25 and P41) with their clearly defined directionality due to the anti-coincidence of both the *F* and *G* detector, particles counted in the integral channel can enter the instrument from both directions along the axis of symmetry. Since the SOHO spacecraft behind the instrument represents a significant amount of shielding for the particles coming from this direction, it is necessary to implement this material in the simulation as well. For this purpose, it is useful to discuss the simulation individually for each of the two hemispheres [see Kühl et al., 2015c]. In the analysis of the simulation results discussed in Chapters 4, 5 and 6, the simulations in these hemispheres will be labelled as *forward* and *backward* for particles coming from the nominal viewing direction and through the spacecraft, respectively, as indicated in Fig. 11.

In addition to data of different coincidences between its detectors, the EPHIN instrument measures counts per minute for every single detector also individually in order to identify the noise level of each detector. In Fig. 14 the temperature of the instrument as well as the count rate for each of its detectors are shown from 1995 till 2017. In the early mission phase, around 1997, the count rate of the E detector increased from roughly thousand to more than a million counts per minute due to noise and was therefore removed from all coincidence conditions. A similar increase in noise can be found for the D detector since 2013. Furthermore, there is a clear correlation between the count rate of the first detector (A) and the temperature of the electronic box of the instrument, which is determined by the distance to the sun and hence the photon flux. This effect indicates a dependence of the noise in detector A on the temperature and photon flux which is not seen in the early phases of the mission due to the existence of shielding kapton and titanium foils on top of the detector (see Fig. 8) which have degraded over time.

Although these effects are interesting from an instrumental point of view, single counter rates can be also utilized for scientific studies. The high statistics (up to 25000 counts/minute for the anti-coincidence of EPHIN, i.e. detector G) allow to investigate small Forbush Decreases (FDs) [Richardson et al., 1996] and SEP events can be easily identified by large and rapid increases in the count rate as is clearly visible during solar maximum in Fig. 14. Furthermore, the count rates reflect the solar modulation of GCRs (cf. Section 2.1) with an 11-year variation especially pronounced for the detectors F and G. In the scope of this work, as a first application, a study on stealth CMEs utilizing the single detector count rates has been performed and published in Heber et al. [2015].

The measurements of the single counter have been analysed utilizing the expected GCR spectrum from the Force-Field Solution (FFS) (cf. Section 2.1) and the energy dependent response of the detector F derived from GEANT4 simulations. The results have been published in:

EXTENDED MEASUREMENT CAPABILITIES OF THE ELECTRON PROTON HELIUM INSTRUMENT ABOARD SOHO - UNDERSTANDING SINGLE DETECTOR COUNT RATES
P. Kühl, S. Banjac, B. Heber, J. Labrenz, R. Müller-Mellin and C. Terasa, Central European Astrophysical Bulletin, Vol. 39, p. 119-124 (2015)

Own contribution: 60 %
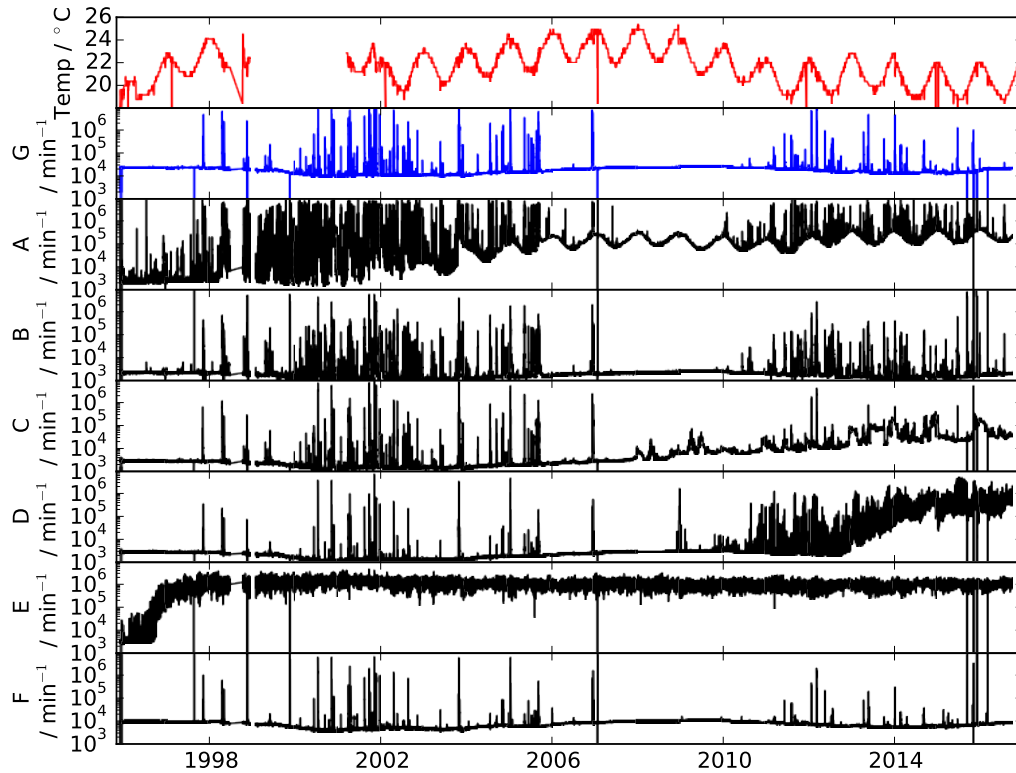
Figure 14: Temperature of the EPHIN instrument as well as single counter count rates of its detectors.

Short overview of the publication

A short introduction of the use of single counter rates is followed by a brief introduction of the EPHIN instrument. In the results section, the energy dependent response of the *F* detector is presented following its convolution with the expected GCR spectra based on the FFS. The resulting expected count rates are compared with the measured count rates of the EPHIN instruments on both, the SOHO and *Chandra* spacecraft. The key findings of the publication are:

- detector *F* is mainly sensitive to ions above 50 MeV per nucleon with the response function rising with energy

- the calculated count rate and its variations before 2006 and after 2011 are in agreement with the measurements of both EPHIN instruments, aboard SOHO and *Chandra*

- the count rates are underestimated between 2006 and 2011 (solar minimum, A^- epoch) most likely due to the fact that the FFS neglects drift effects

EXTENDED MEASUREMENT CAPABILITIES OF THE ELECTRON PROTON HELIUM INSTRUMENT ABOARD SOHO - UNDERSTANDING SINGLE DETECTOR COUNT RATES

P. Kühl[1], S. Banjac[1], B. Heber[1], J. Labrenz[1], R. Müller-Mellin[1] and C. Terasa[1]

[1]*Institute for Experimental and Applied Physics, Christian-Albrechts-University Kiel, Germany*

Abstract. Forbush (1937) was the first to observe intensity decreases lasting for a few days utilizing ionization chambers. A number of studies on Forbush decreases (FDs) have been performed since then utilizing neutron monitors and space instrumentation. The amplitude of these variations can be as low as a few ‰. Therefore intensity measurements need to be of high statistical accuracy. Richardson et al. (1996) suggested therefore to utilize the single counter measurements of the guard counters of the IMP 8 and Helios E6 instruments. Like the above mentioned instruments the Electron Proton Helium INstrument (EPHIN) provides single counting rates. During the extended solar minimum in 2009 its guard detector counted about 25000 counts/minute, allowing to determine intensity variations of less than 2‰ using 30 minute averages. We performed a GEANT 4 simulation of the instrument in order to determine the energy response of all single detectors. It is shown here that their energy thresholds are much lower than the ones of neutron monitors and therefore we developed a criterion that allows to investigate FDs during quiet time periods.

Key words: Galactic Cosmic Rays - Forbush Decreases - Mesurements

1.   Introduction

Galactic cosmic rays are energetic charged particles that are entering the heliosphere from outside. On their way they are getting modulated by the turbulent heliospheric magnetic field embedded in the expanding solar wind. These variations occur on different timescales. Forbush Decreases (FDs, Forbush, 1937; Hess and Demmelmair, 1937) are associated to the interplanetary counter part of coronal mass ejections (ICMEs) and Corotating Interaction Regions (CIRs). Due to the limited geometric factor of the scientific channels of most spacecraft instrumentation, FDs have been inves-
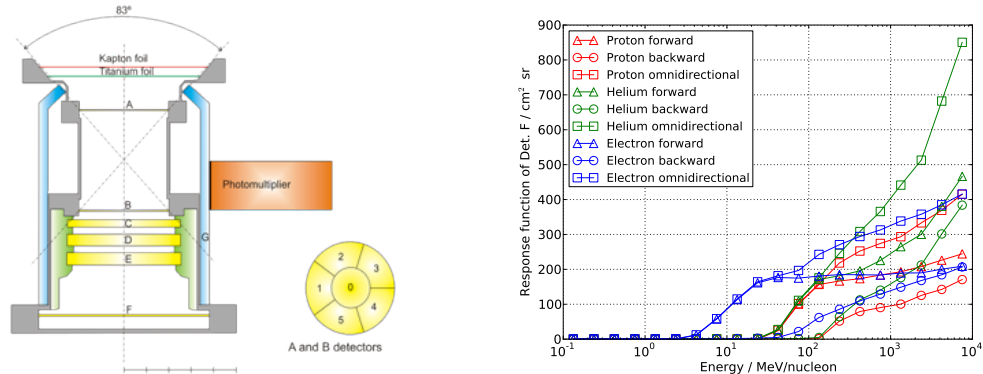
UNDERSTANDING SINGLE DETECTOR COUNT RATES

Figure 1: Left: Sketch of the EPHIN sensor. Right: Response function of the single detector F based on the GEANT 4 simulation.

tigated by means of neutron monitors (e.g. Belov et al., 2014). Richardson et al. (1996) showed that single detector counting rates of spacecraft instruments, like Helios E6 (Kunow et al., 1977) or aboard IMP 8 (McGuire et al., 1986), are suitable for FD analysis. In contrast to neutron monitors spacecraft data suffer neither geomagnetic nor atmospheric variation (Papaioannou et al., 2010) and are sensitive to energetic particles of lower energies. During quiet times their count rates are dominated by the variation of galactic cosmic ray protons and alpha particles and follow the intensity-time profile of >60 MeV/nuc. ions. In order to quantify the response function of the single detectors of the Electron Proton Helium INstrument (EPHIN) we present here the results of a GEANT 4 Simulation of the instruments aboard the SOHO and Chandra satellite (section 3.1).

2. Instrumentation

Launched on December 2, 1995 and on July 23, 1999 the SOHO and Chandra missions were successfully brought into orbit around L1 and in a highly elliptical orbit around the Earth, respectively. While EPHIN is part of the scientific payload aboard SOHO, its spare flight unit was mounted as a radiation monitor on Chandra, providing real time information on the radiation environment to the spacecraft allowing to turn off the cameras during the radiation belt crossings and during large solar energetic particle events. While the instrument on SOHO is still operating, data from the Chandra unit are

UNDERSTANDING SINGLE DETECTOR COUNT RATES

only useful for periods for which the sensor temperature drops below 45° C. Due to Chandra's orbit with a perigee of 16,000 km and apogee of 139,000 kilometers the spacecraft spends only a fraction of time in interplanetary space. However, both data sets are of unique value because of their potential use for correlated space weather studies. As shown in Fig. 1 left the EPHIN telescope aboard SOHO and Chandra consists of 6 semiconductor detectors that are surrounded by a scintillation detector. During solar minimum detector F has a counting rate of more than 10000 counts/minute.

3.   Results

3.1.   GEANT 4 SIMULATION

While being superior in terms of statistics and time resolution compared to the coincidence channels, single counters do have the deficit of lacking any direct information about the energy deposition of measured particles. To account for this issue, one can exploit the fact that every single detector is in a different position in the instrument and thus the shielding for every detector due to the intrument and spacecraft structures differs, resulting in different energy response functions for each detector.
To calculate the response functions, a GEANT4 Monte Carlo simulation (Geant4-Collaboration, 2003) of the EPHIN instrument has been set up including not only the detectors but also the instrumental structures. To account for the shielding effect of the spacecraft, an aluminium block is added behind the instrument. The thickness of the block was chosen to be 10 cm as this is the approximated mass equivalent of aluminium based on the spacecraft total mass and dimension. Results for forward (isotropic particle source in front of the detector) and backward (isotropic particle source behind the detector and the spacecraft/aluminium block) incident particles are presented individually and compared to an omnidirectional isotropic flux. In Fig. 1 right, the response function derived from the simulations is shown for detector F. In detail, results for protons (red), helium (green) and electrons (blue) emitted by forward (triangles), backward (circles) and omnidirectional (squares) particle sources are presented. Based on the plot, it is evident that detector F is sensitive for ions above a threshold of 50 MeV. Due to the importance of scattering and production of secondaries for high energy particles, the response function of the detector rises with energy and
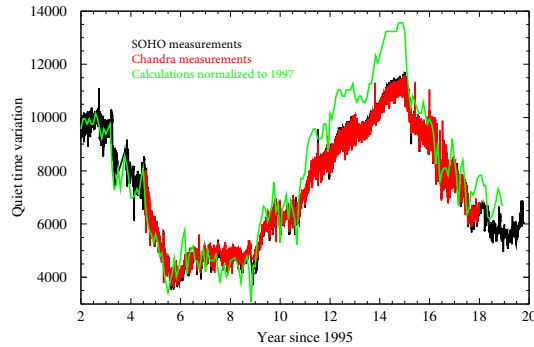
UNDERSTANDING SINGLE DETECTOR COUNT RATES

Figure 2: Measured and derived (force field solution folded with detector response) quiet time counting rates of the single detector F. Note, that the count rate of Chandra and the simulated count rate are multiplied with a factor 0.88 and 1.2, respectively

increases even above the geometry factor ($G_F = 157\ cm^2\ sr$ for each hemisphere, $G_F^{omni} = 2 \cdot G_F = 314\ cm^2\ sr$ for omnidirectional flux (based on Sullivan, 1971)). This effect is especially present for helium (above ≈ 400 MeV/nuc) compared to protons (above ≈ 2000 MeV).

3.2. COMPARISON TO IN-FLIGHT DATA

Due to the harsh conditions single detector rates for detectors A and G are not available from Chandra anymore. In order to determine quiet time conditions (i.e. timeperiods without solar energetic particle events (SEPs)) the same way for both instruments, single counting rates of detector F are analyzed. Due to the solar activity cycle, we expect the highest quiet time counting rate to occour during solar minimum in 2009. Furthermore, the influence of SEPs is neglectable in this year and hence, the entire year can be considered to be quiet time. For SOHO/EPHIN we derived an average of $\bar{c}_{2009} = 434$ counts/minute and $\sigma_{2009} = 23$ counts/minute. In order to determine the counting rates during quiet times for any given timeperiod, the mean value of the counting rate distribution only taking into account counting rates below $c_u \leq \bar{c}_{2009} + 4 \cdot \sigma_{2009} = 526$ counts/minute is calculated. Daily averaged quiet time count rates of detector F on SOHO (black curve) and Chandra (red curve) are displayed in Fig. 2. The count rate of detector F on Chandra is about 10% larger than the one aboard SOHO. The most probable reason for this is the different mass of the satellites and the

UNDERSTANDING SINGLE DETECTOR COUNT RATES

corresponding shielding. However, normalizing both in 2009 close to solar minimum we find a good agreement between both detectors for the whole period from 1999 to 2012. The modulation amplitude $\frac{c_{2009} - c_{2001}}{c_{2001}}$ is about 60% from solar minimum in 2009 to solar maximum in 2000/2001.

For further interpretation of the data, we followed the Ansatz by Caballero-Lopez and Moraal (2012) that is used to explain neutron monitor measurements during different latitude scans. In order to utilize the response functions $R(E)$ as yield functions we need to know the galactic cosmic ray spectra $I(E)$ at Earth for all periods of interest for different nuclei. A common approach to estimate the spectra for protons and helium is to apply the force field solution given by Usoskin et al. (2011). As described by Caballero-Lopez and Moraal (2012) the contribution of carbon and heavier nuclei can be accounted for when multiplying the helium spectra with a factor of 1.3. These spectra are then folded with the response functions. The result of folding is a count rate that is by 20% smaller than the measured counting rates. The green curve in Fig.2 shows the resulting count rate multiplied by 1.2. From the figure it is evident that the count rate of our simple model tracks the observed measurement aboard SOHO and Chandra very well for the period from 1997 to 2006. A strong deviation is observed from 2006 to 2011 during the last solar minimum. Since the modulation cycle is connected with the 22-year Hale cycle and not the 11-year sunspot cycle the 1997 and 2009 solar minima differ by the solar magnetic epoch. It is well known that the force field solution does not take into account drift effects that lead to the alternating peaked and flat time profiles observed during alternating solar minima. But not only the shape of the time profiles but also the shape of the energy spectra differ significantly leading to higher count rates at neutron monitor energies during an A<0-solar magnetic epoch in 2009 than in an A>0-solar magnetic epoch (1997). The opposite is true for energies below a few GeV (Potgieter et al., 2001). Due to this effect it is not a surprise that the modulation parameter derived from the neutron monitor network underestimates the modulation potential during an A<0-solar magnetic epoch.

4.   Summary and conclusion

Single detector measurements from EPHIN aboard SOHO and Chandra can be understood by deriving the response function as a function of energy.

UNDERSTANDING SINGLE DETECTOR COUNT RATES

The geometric factor for the single detector at about one GeV is in good agreement with the geometrical values. When folding the response function with the force field solution with different modulation potentials as given by Usoskin et al. (2011) the measured amplitude from solar minimum to maximum of about 60% during an A>0-solar magnetic epoch is reproduced. Thus the quiet time single detector counting rates of the EPHIN detectors F aboard SOHO and Chandra can be used as proxy for the modulation. Furthermore, they allow the analysis of small scale variations on short time scales thanks to very high count rate statistics. Variation of less than 1‰ and 1‰ can be investigated on the basis of 1 minute and 2 hour averaged count rates, respectively. From that point of view these detectors are ideally suited to analyze Forbush decreases. However, their response to particles of lower energies make them sensitive to solar energetic particle events masking the effects of the subsequent Forbush decrease.

Acknowledgements

References

Belov, A. et al.: 2014, *Solar Physics* **289**(1), 3949–3960.
Caballero-Lopez, R. A., and Moraal, H.: 2012, *Journal of Geophysical Research (Space Physics)* **117**(A), 12103.
Forbush, S. E.: 1937, *Physical Review* **51**(1), 1108–1109.
Geant4-Collaboration: 2003, *Nuclear Instruments and Methods in Physics Research Section A* **506**(3), 250 – 303.
Hess, V. F., and Demmelmair, A.: 1937, *Nature* **140**(3), 316–317.
Kunow, H. et al.: 1977, *Journal of Geophysics* **42**, 615–631.
McGuire, R. E. et al.: 1986, *Astrophysical Journal* **301**, 938–961.
Müller-Mellin et al.: 1995, *Solar Physics* **162**(1), 483–504.
Papaioannou, A. et al.: 2010, *Solar Physics* **266**(1), 181–193.
Potgieter, M. S. et al.: 2001, *Space Sci. Rev.* **97**, 295–307.
Richardson, I. G. et al.: 1996, *Journal of Geophysical Research* **101**(A), 13483.
Sullivan, J. D.: 1971, *Nuclear Instruments and Methods* **95**, 5.
Usoskin, I. G. et al.: 2011, *Journal of Geophysical Research* **116**(A), 2104.

EXTENSION OF THE EPHIN ENERGY RANGE

In order to understand the chain of physical processes from the acceleration of Solar Energetic Particles (SEPs) at or near the Sun to their injection into and their transport in the interplanetary medium, it is important to measure their energy spectrum near Earth (see Section 2.2). While a large number of space-borne instruments provide these measurements at intermediate energies (up to several tens of MeV), precise observations at higher energies have become available only recently with instruments like PAMELA and AMS. In contrast, the Electron Proton Helium Instrument (EPHIN) aboard the Solar and Heliospheric Observatory (SOHO) has a nominal energy range for protons from 4 MeV up to 53 MeV and spectral information above 53 MeV is difficult to consider for SEPs.

To overcome this limitation, a method to extend the proton energy range of EPHIN has been developed in this thesis. The aim of this method is to derive the proton spectrum for protons above 53 MeV that penetrate the entire instrument based on the measured energy losses in the detector stack. In order to achieve this, the particle type (e.g. mass and charge of the particle) as well as the kinetic energy of the detected particles have to be derived. For this purpose, a GEANT4 simulation (cf. section 3.3) has been set up in order to investigate the response of EPHIN to particles with energies above the nominal energy range.

One of the results of the simulations is the most likely energy loss in the instrument as a function of the type and energy of the particle as shown in Fig. 15. It can be concluded that energy losses between 0.4 and 1.5 keV/μm (marked by the shaded range) are almost solely caused by protons. Hence, for this energy losses, an identification of the type of the particle is not necessary. Furthermore, there is a clear functional relation between kinetic energy and the resulting energy loss (see Section 4.2 for a derivation). With this relationship, the most likely kinetic energy can be derived based on the measured energy losses, allowing to derive proton energy spectra.

The method and first results have been described and published in:

PROTON INTENSITY SPECTRA DURING THE SOLAR ENERGETIC PARTICLE EVENTS OF MAY 17, 2012 AND JANUARY 6, 2014
P. Kühl, S. Banjac, N. Dresing, R. Goméz-Herrero, B. Heber, A. Klassen and C. Terasa, Astronomy & Astrophysics, Volume 576, id. A120, 9 pp. (2015), DOI: 10.1051/0004-6361/201424874
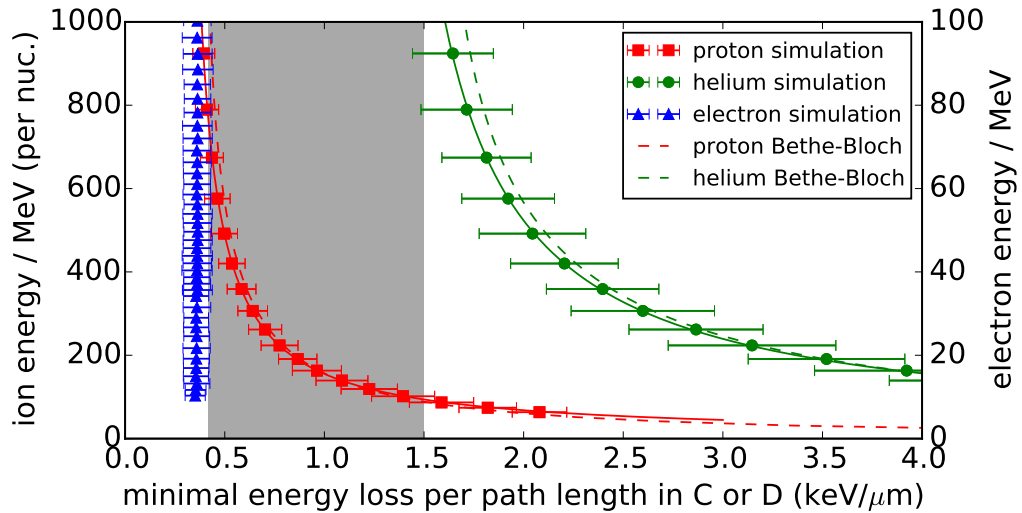
Own contribution: 80 %

Figure 15: Simulated kinetic energy of protons (red), helium (green) and electrons (blue) as a function of the resulting energy loss in EPHIN. Figure taken from Kühl et al. [2015a].

Short overview of the publication

An introduction of SEP events and EPHIN is followed by a detailed description of GEANT4 simulations of the instrument and their results. Based on these findings, a method to derive proton spectra above 50 MeV has been developed and is presented including a discussion on several issues such as backward penetrating particles. An estimation of the uncertainties for spectra during SEP events is performed before the method is applied for the May 17, 2012 and January 6, 2014 SEP events. For the first event, a comparison with PAMELA results [Bazilevskaya et al., 2013] has been performed as validation. Both events and the differences between the proton spectra are discussed with respect to findings from Thakur et al. [2014], who claimed that the later event should also be considered to be a GLE. The key findings of the publication are:

- EPHIN is capable of measuring the proton energy spectrum from 50 MeV up to 1 GeV during SEP events

- particles penetrating the SOHO spacecraft and EPHIN from behind can cause misleading energy losses in the detector

- the uncertainties in the proton spectra caused by these backward particles and by helium particles can be neglected during SEP events

- whether or not a SEP event is detected by multiple ground-based observatories such as NMs does depend on both, the spectral properties of the event and the viewing direction and cut-off rigidity of the available ground stations

**Astronomy
&
Astrophysics**

Proton intensity spectra during the solar energetic particle events of May 17, 2012 and January 6, 2014

P. Kühl[1], S. Banjac[1], N. Dresing[1], R. Goméz-Herrero[2], B. Heber[1],
A. Klassen[1], and C. Terasa[1]

[1] Institute for experimental and applied physics, University Kiel, 24118 Kiel, Germany
e-mail: kuehl@physik.uni-kiel.de
[2] Space Research Group, University of Alcalá, 28871 Alcalá de Henares, Spain

ABSTRACT

Context. Ground-level enhancements (GLEs) are solar energetic particle events that show a significant intensity increase at energies that can be measured by neutron monitors. The most recent GLE-like events were recorded on May 17, 2012 and January 6, 2014. They were also measured by sophisticated instrumentation in space such as PAMELA and the Electron Proton Helium INstrument (EPHIN) onboard SOHO. Since neutron monitors are only sensitive to protons above 400 MeV with maximum sensitivity at 1 to 2 GeV, the spectra of such weak GLE-like events (January 6, 2014) can only be measured by space instrumentation.
Aims. We show that the SOHO/EPHIN is capable of measuring the solar energetic particle proton event spectra between 100 MeV and above 800 MeV.
Methods. We performed a GEANT Monte Carlo simulation to determine the energy response function of EPHIN. Based on this calculation, we derived the corresponding proton energy spectra. The method was successfully validated against previous PAMELA measurements.
Results. We present event spectra from EPHIN for May 17, 2012 and January 6, 2014. During the event in May 2012, protons were accelerated to energies above 700 MeV, while we found no significant increase for protons above 600 MeV during the event on January 6, 2014.

Key words. instrumentation: detectors – Sun: flares – Sun: coronal mass ejections (CMEs) – solar-terrestrial relations – space vehicles: instruments

1. Introduction

Forbush (1946) reported the first solar energetic particle (SEP) event that is now called a ground-level enhancement (GLE). These events are produced when ions with energies above several hundred of MeVs create a nuclear cascade in the Earth atmosphere. As a consequence, detectors at ground level measure an increase above the galactic cosmic-ray background (GCRB). Since then, 71 GLEs have been reported that exceed the GCRB by barely a few percent. The largest measured increase of about 4500% above the GCRB was observed during GLE 5 on February 23, 1956 (Reames 2013). During solar cycle 24, only the event on May 17, 2012 was unambiguously measured by more than one neutron monitor. In addition to understanding the physics of GLEs, that is, the acceleration process, the recent paper by Thakur et al. (2014) claimed that the event on January 6, 2014 was GLE 72 and sparked a discussion on the definition of a GLE (Usoskin, priv. comm., see also www.nmdb.eu). The question of the definition whether a solar energetic particle event is recorded as a GLE or not depends on several factors; the measurement capabilities at ground level for magnetic and atmospheric cutoff rigidities, for instance, need to be lower than one GV. To overcome this situation, it would be better to rely on spacecraft measurements outside the Earth magnetosphere. Here we show that the Kiel Electron Proton Helium Instrument (EPHIN, Müller-Mellin et al. 1995) oboard the SOHO spacecraft

can indeed provide such energy spectra for selected particle events.

On May 17, 2012 at 01:25 UT, the NOAA active region 11476, located at N11W76, produced a class M5.1 flare (Gopalswamy et al. 2013; Shen et al. 2013). Around 01:50 UT, the worldwide network of neutron monitors[1] detected the first ground-level enhancement in solar cycle 24. The energy spectra as measured by the payload for antimatter-matter exploration and light-nuclei astrophysics (PAMELA; Picozza et al. 2007) have been reported by Bazilevskaya et al. (2013), indicating that protons with energies of up to one GeV and helium of up to 100 MeV/nucleon were accelerated during that event.

On January 6, 2014 STEREO A and B detected a flare in the extreme ultraviolet (EUV) at 7:30 UT with a double maximum at 7:55 UT and 8:15 UT that occurred 25 degree behind the western limb as seen from Earth. The event was associated with a coronal mass ejection (CME) and an EUV wave. Type II and III radio bursts were recorded by measurements on ground as well as in space. Eleven one-minute running-mean averages exceed the pre-event distribution at the South Pole neutron monitor and the bare counter at about 8:10 UT, which agrees well with the GOES observations (Thakur et al. 2014). Note that Thakur et al. (2014) reportet an onset time of 7:58 UT, indicating the uncertainty of different methods to determine the event onset. Since we did not
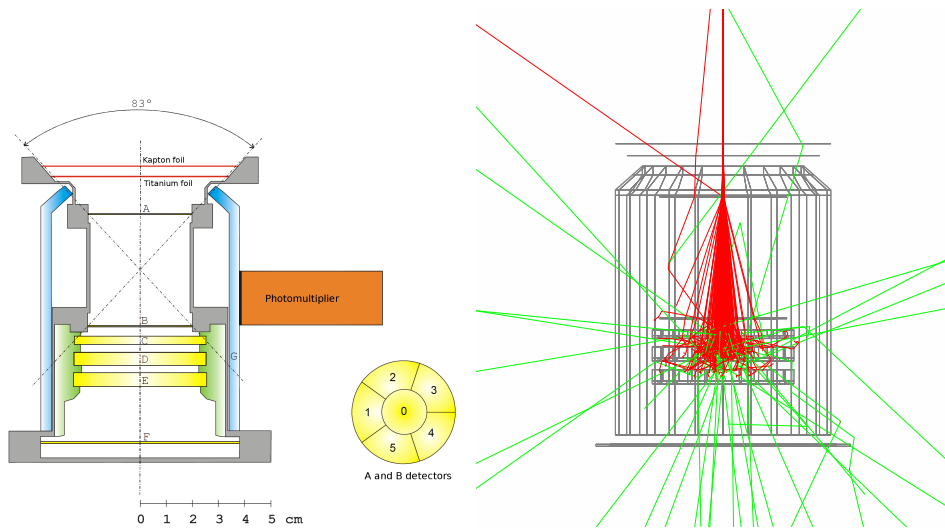
---

[1] http://www.nmdb.eu/

Fig. 1. *Left*: sketch of the EPHIN instrument. *Right*: instrument as modeled in the GEANT4 simulations including a beam of 100 electrons (5 MeV, red) as well as gamma secondaries (green). Note that the detailed housing shown in the left sketch is also included in the GEANT4 model. It is not shown here for greater clarity.

find any statistically significant intensity increase (above 4σ) for other neutron monitors such as Tixie Bay or McMurdo, it is an open question whether this event can be defined as ground-level enhancement number 72. To make significant progress here, it is essential to know the particle, that is, the proton energy spectra above the atmosphere. In this paper, we present a new method for extending the measurements capabilities of SOHO/EPHIN into the energy range from ~100 MeV to above 800 MeV for protons.

2. GEANT 4 simulation of the Electron Proton Helium Instrument

The Electron Proton Helium INstrument (EPHIN, Müller-Mellin et al. 1995) is part of the Comprehensive Suprathermal and Energetic Particle Analyzer (COSTEP) instrument suite onboard the Solar and Heliospheric Observatory (SOHO). SOHO was launched in December 1995 and has an orbit around the Lagrangian point L1. Figure 1 (left) shows a sketch of the instrument, which consists of six solid-state detectors (labeled A−F) enclosed in a scintillator that acts as anticoincidence (G). The measurements of EPHIN rely on the dE/dx−E method, which yields count rates for different ranges in the silicon detector stack. As described by Müller-Mellin et al. (1995), different ions and even isotopes can be identified based on the energy deposition in the first detector ΔE_A and the sum of the energy depositions E in all detectors. In addition to the total counts of these different coincidence conditions, energy losses in each detector are available for a statistical sample of individual particle tracks, allowing a detailed analysis of the measured particles including the calculation of energy spectra for electrons up to ≈10 MeV and ions up to ≈50 MeV/nucleon.

In addition, the instrument allows measuring penetrating particles that are combined in an integral channel. It is more challenging to calculate the energy for these particles because the total energy of the particle and the particle type are a priori unknown. Furthermore, the coincidence condition for penetrating particles can also be fulfilled by particles entering the instrument
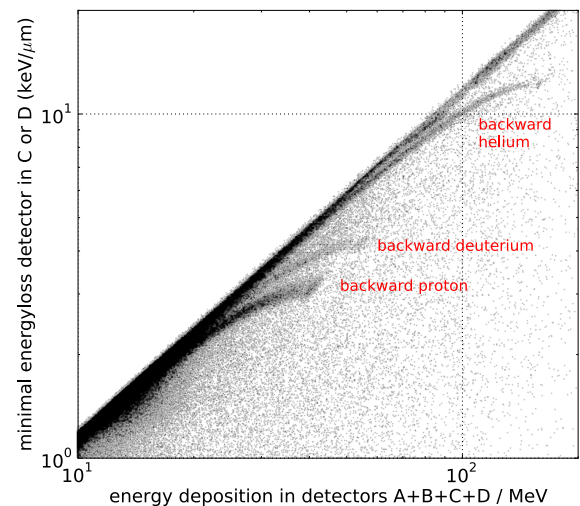

Fig. 2. Minimum of the energy loss in detectors C and D as a function of the total energy loss seen in the instrument in December 2009. The expected tracks for backward-penetrating particles (protons, deuterium, and helium) are marked. For details see text.

from behind. However, the statistical sample of energy losses does include penetrating particles. Based on these data, Fig. 2 displays the minimum energy loss per path length in detectors C and D (i.e., min(dE_c/b_c, dE_d/b_d) with dE_x energy loss in detector x and b_x the thickness of the detector) as a function of the total energy loss seen in the detector stack for the Galactic cosmic-ray background (data from December 2009). The tracks for backward-penetrating protons, deuterium, and helium have been identified and marked based on the Bethe-Bloch equation. These tracks merge with the tracks of forward-penetrating particles along the diagonal, and thus a separation between forward and backward penetrating particles is only possible in a limited

P. Kühl et al.: Proton intensity spectra during the May, 2012 and January, 2014 SEP events
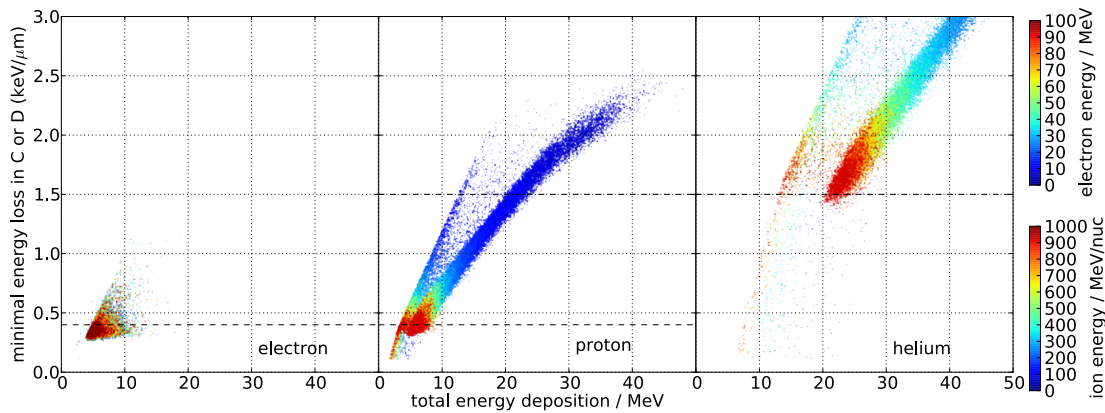

Fig. 3. Simulation results of the energy losses for electrons, protons, and helium particles. Note the different color scales for electrons and ions. For a colored version of the plot, we refer to the online version of this article.

energy range. Furthermore, backward-penetrating particles have to pass the spacecraft, which acts as an additional shielding, and thus the energy threshold of forward- and backward-penetrating particles differs substantially.

To address these problems, a GEANT4 Monte Carlo simulation that considers various processes such as electromagnetic and hadronic interaction of particles in matter and the production of secondary particles has been set up (GEANT4 Collaboration 2006, version 4.9.6.2). Different calculations for forward- and backward-penetrating particles were performed separately. Figure 1 (right) displays the instrument as it is implemented in the GEANT4 simulation (see also Böhm et al. 2007) with typical particle tracks calculated in the simulation. Shown are results for 5 MeV electrons (red trajectories) that scatter in the detector stack and produce secondary gamma rays (green). Since our focus is on solar energetic particle events that may be considered to be a GLE but are only recorded at neutron monitors with cut off rigidities below 2 GV, energies above 1 GeV per nucleon for ions and 100 MeV for electrons are not considered because it is unlikely that they are accelerated in these events. The assumed upper limit chosen for protons was confirmed for the event in May 2012 by Bazilevskaya et al. (2013), and since the event in January 2014 was observed by fewer neutron monitors with the lowest rigidity cutoff, its highest energy can be considered to be even lower. The upper limit for electrons is based on observations by Moses et al. (1989). The lowest energy that was simulated is defined by the necessary energy of a particle to penetrate the entire instrument (Müller-Mellin et al. 1995). Thus, we chose energies ranging from 50 MeV/nucleon to 1 GeV/nucleon for ions and from 10 MeV up to 100 MeV for electrons. Since no detailed information regarding the real mass distribution of the s/c is available, the shielding was estimated to be equivalent to 10 cm of aluminum based on spacecraft mass and geometry. Below we discuss the modeling results for forward- and backward-penetrating particles separately. This is realized by two simulations featuring a half-sphere located in front of and behind the instrument. Particles are then emitted equally distributed in angles over the half-sphere.

2.1. Forward-penetrating particles

Here we describe the results of the GEANT4 simulations using particles that incite the detector stack from the front. To cover the

energy space with the same probability, the intensity was chosen to be constant over energy. A year after the launch of SOHO, one of the detectors, detector E, started to become noisy, therefore it was decided to remove the detector from the coincidence logic as described in Müller-Mellin et al. (1995). Figure 3 shows from left to right the minimum of the energy depositions per path length of detectors C and D versus the total energy registered in the instrument for electrons, protons, and helium particles. The color of each dot represents the particle energy in the simulation as indicated by the color bars on the right. The minimum of the energy loss per path length of detectors C or D was used to reduce the influence of scattering. In the figure, two different particle tracks can be identified for the ions. The main population with higher total energy deposition is based on particles that deposit energy in every detector A−F, while the second track is caused by particles that pass through the detectors A−D and F, without energy deposition in detector E. From Fig. 1 it is obvious that only a small fraction of penetrating trajectories can miss detector E without hitting the anticoincidence. Furthermore, Fig. 3 indicates that the measured energy in detectors C and D is not affected by these trajectories because the energy losses in C and D at a given energy (color-coded in the figure) are the same for both tracks. Therefore we used the minimum of the energy loss per path length in C or D throuhgout instead of the total energy deposition E.

From Fig. 3 it is evident that there are overlaps of the proton signatures with both the electron and the helium signatures above or below the dashed lines, respectively. Since an independent particle identification is not possible, the proton spectra are contaminated by electrons and helium at low and high energies. In the intermediate region with energy depositions between 0.4 keV/μm and 1.5 keV/μm such contaminations are unlikely.

To explore the energy range that corresponds to that energy depositions, histograms of the energy deposition for different particles are presented in Fig. 4. The proton energies of 100 MeV and 800 MeV are chosen such that the mean of the energy loss distributions is clearly contained in the limits of 0.4 keV/μm and 1.5 keV/μm. Because the electron energy only slightly affects the energy depositions (see Fig. 3), the energy was chosen arbitrarily as 20 MeV. For the helium particles, an energy of 1 GeV per nucleon was selected because these high energies result in the smallest energy depositions per path length. The figure shows that energy depositions between 0.4 keV/μm and 1.5 keV/μm are mainly caused by protons in the energy range between 100 MeV
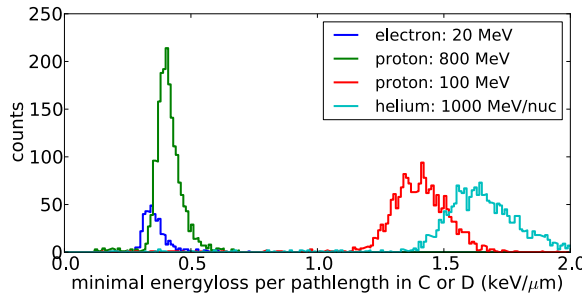
Fig. 4. Histogram of the energy deposition for electrons, protons, and helium particles based on mono-energetic simulations.

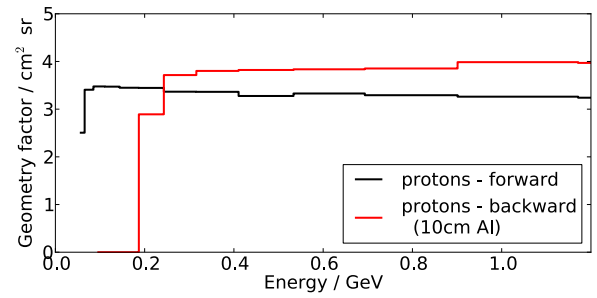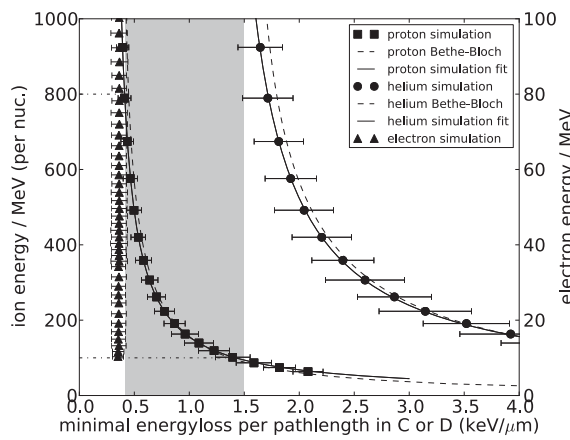**Fig. 5.** Simulated kinetic energy of the particles as function of the resulting energy deposition in the detector. Simulation results for forward-penetrating electrons (triangle, right axes), protons (squares), and helium particles (circles) are shown. In addition, calculations based on the Bethe-Bloch equation (dashed lines) and fit results (solid lines) for the ions are presented. The shaded area marks energy losses that are most propably caused by protons.

and 800 MeV. Since lower and higher energy depositions can only be caused by electrons or helium particles, respectively, the derived proton spectrum based on the method described in this work is limited to these energies.

Furthermore, the energy loss distributions for all particles tend to have a Gaussian shape, and hence the mean value and the standard deviation of the distributions can be used to facilitate the analysis further. Because we are interested in reconstructing the total energy of a particle based on the energy deposition, the simulated energy is shown as a function of the resulting energy deposition in Fig. 5. The figure shows in agreement with Fig. 4 that the main contribution of energy depositions between 0.4 keV/μm $\lesssim \frac{\mathrm{d}E}{\mathrm{d}x} \lesssim 1.5$ keV/μm (marked by the shaded area) is made by protons with energies between 100 MeV $\lesssim E \lesssim$ 800 MeV (indicated by dashed-dotted lines).

To calculate the total energy of the measured particles based on the energy depositions, inversion methods have often been used in the past (compare Böhm et al. 2007). Before applying such sophisticated mathematical methods, we start with a simple procedure based on the results above. Our approach is supported by the fact that the response function in the energy range of interest does not depend on energy (black curve in Fig. 6) and an analytic relation between energy deposition and total energy

Fig. 6. Geometry factors for forward- and backward- (10 cm aluminum shielding) penetrating protons.

can be expressed by a fit, as presented in Fig. 5. The function reads

$$E = a + b/(\mathrm{d}E - c), \qquad (1)$$

where E is the kinetic energy of the measured particle (in MeV per nuc.), dE (in MeV) corresponds to the energy deposition in the detector elements and a, b, c are variables. This function is motivated by the Bethe-Bloch equation with parameters a and c added to take relativistic corrections into account. Fitting this function to the simulation results for protons as shown in Fig. 5 defines the parameter to

$a = 4.65 \pm 1.06,$
$b = 1.09 \times 10^{-1} \pm 8.81 \times 10^{-4}$ and
$c = 2.74 \times 10^{-4} \pm 1.05 \times 10^{-6}.$

With this function, the total energy of penetrating protons in the given energy range can be derived. Based on the measured energy loss data, this results in a histogram of the total energy that can be converted into a spectrum exploiting the instrument geometry factor and considering the ratio of the total counts to the size of the statistical sample.

2.2. Backward-penetrating particles

A GEANT4 simulation as presented above was also performed for backward-penetrating particles by including an approximated shielding by the spacecrafts body of 10 cm aluminum behind the instrument. Particles were injected from a half-sphere behind the aluminum layer.

Figure 7 presents the simulation results for backward-penetrating particles. Similar to the forward-penetrating particles, two particle tracks can be identified for ions as some of them may miss detector E (see Fig. 3). For electrons, the shape of the energy-loss distribution does not change, and therefore, like forward-penetrating electrons, they do not contaminate the energy-loss histogram in the considered ranges.

For the ions, however, differences between forward and backward results occur. Regarding the total energy of the particles, energy loss is caused by backward-penetrating particles with higher energy than the energy loss caused by forward-penetrating particles. This effect can be explained by the fact that particles coming from behind the instrument have to penetrate the shielding and therefore will reach the instrument with only a fraction of their initial energy. The calculated geometry factors shown in Fig. 6 for backward- and forward-penetrating protons support this explanation. While protons need to have a kinetic

P. Kühl et al.: Proton intensity spectra during the May, 2012 and January, 2014 SEP events
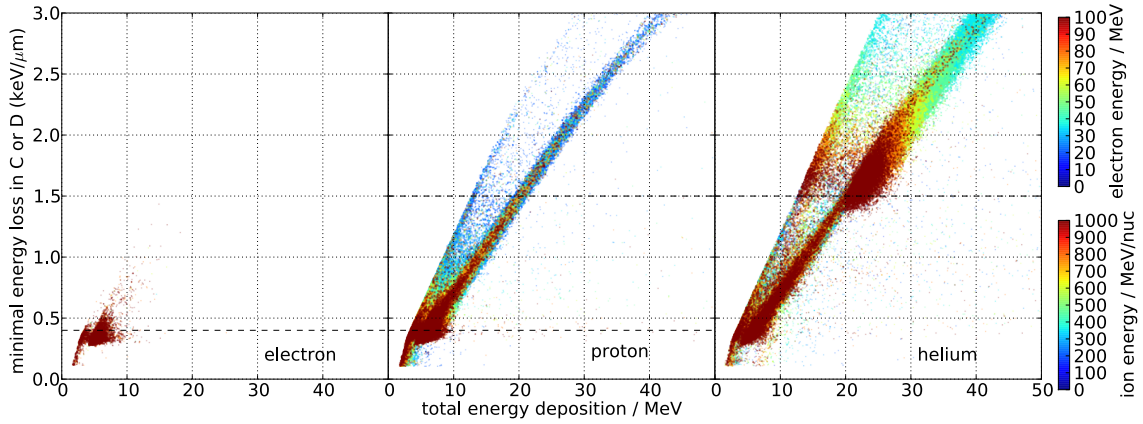

Fig. 7. Simulation results of the energy losses for backward-penetrating electrons, protons, and helium particles with 10 cm of aluminum shielding. Note the different color scales for electrons and ions. For a colored version of the plot, we refer to the online version of this article.
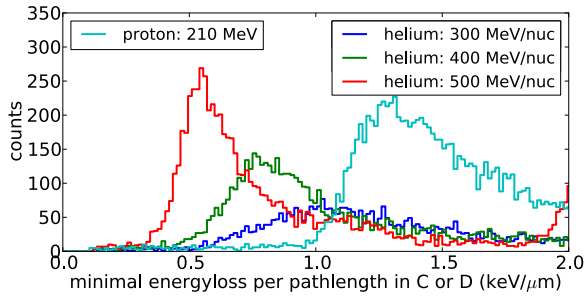

Fig. 8. Histograms of the energy deposition for backward-penetrating helium particles and protons with different energies. Above 300 MeV per nucleon, a population of secondary protons is clearly visible.

Fig. 9. Simulated kinetic energy of the particles as a function of the resulting energy deposition in the detector. Energy deposition in the detector based on the kinetic energy of the particle. Simulation results for forward- (filled) and backward- (open) penetrating electrons (triangle, right axes), protons (squares), helium particles (circles), and secondary protons (diamonds) are shown. In addition, calculations based on the Bethe-Bloch equation (dashed lines) and fit results (solid lines) for the ions are presented. The shaded area marks energy losses that are most probably caused by protons.

energy of ≈ 50 MeV to trigger the integral channel when coming from the front of the detector, backward-penetrating protons need to have at least ≈ 200 MeV to do so. This effect is confirmed by the energy loss histogram of 200 MeV backward-penetrating protons presented in Fig. 8: the distribution shows similar energy losses as for the 50 MeV forward-penetrating protons (Fig. 4). Furthermore, backward-penetrating ions can cause higher energy depositions in detectors C and D than forward-penetrating ions. This is because detectors A and B have a different material thickness (450 μm) than detectors E and F (5500 μm).

The results for helium do not only differ in terms of their total energy as a result of the shielding effect, but also in the distribution of energy losses in general. In contrast to the forward-penetrating helium, backward-penetrating helium can cause energy losses below the threshold, indicated by the dashed line, in a significant amount. The histograms of the energy deposition presented in Fig. 8 indicate that in addition to the expected high energy losses, a second distribution at typical energy losses of protons is caused by these backward-penetrating helium particles. The contamination of these secondaries starts to rise above energies of 300 MeV per nucleon of the primary helium particle. According to the simulation, these energy depositions are secondary protons created by helium particles in the shielding that then enter the instrument.
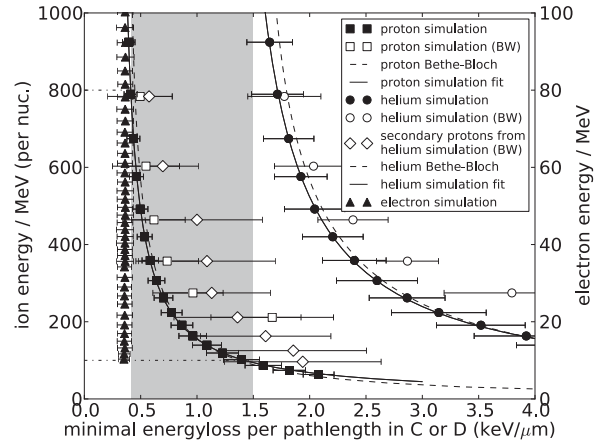
2.3. Combined signals and error estimations

In Fig. 9 the results from the backward simulations are summed as open symbols in addition to the results of the forward-penetrating simulations (filled symbols). Note that secondary protons created by primary helium distributions are presented individually. The figure indicates that backward-penetrating protons mimic forward-penetrating protons with lower energies, resulting in errors in the spectrum calculated by the method described above. However, as solar events are known to have soft spectra whose intensity quickly decreases with increasing energy (Mewaldt et al. 2012), low-energy protons are more likely than particles with higher energies that mimic them. To illustrate this point, Fig. 10 shows the energy-loss histograms for forward- and backward-penetrating protons resulting from
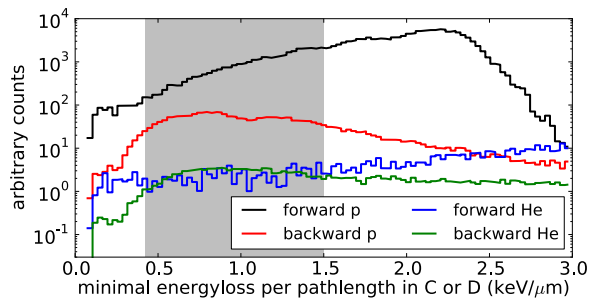
Fig. 10. Energy-loss histogram with $\gamma = -3$ for forward- and backward-penetrating protons and helium particles with a helium-to-proton ratio of 10%.

simulations based on a power-law spectrum $I(E) = I_0 \cdot \left(\frac{E}{E_0}\right)^{-\gamma}$ with a spectral index of $\gamma = 3$ as typically observed during solar events (excluding the time during the onset of the events, see Mewaldt et al. 2012). The range of energy losses taken into account for the spectrum calculated is marked by shading. The figure shows that under the considered circumstances the highest contribution of backward-penetrating protons occurs at low dE/dx and is in the order of 20%. At higher energy losses, the contribution is substantially lower (down to 2%) because of the shielding of the spacecraft.

In addition to the proton results, Fig. 10 presents energy-loss histograms for forward- and backward-penetrating helium (including the produced secondary protons) with similiar spectral shape and an assumed flux ratio $He/p = 10\%$. This flux ratio is a reasonable worst-case scenario based on ERNE measurements (Torsti et al. 1995), which we examined for the time periods of the events[2]. From the figure, it is obvious that the influence of helium particles is negligible as these particles only account for $\approx 1\%$ of the total counts, while up to $\approx 20\%$ of the counts are caused by backward-penetrating protons.

Based on this analysis, we conclude that the maximum systematic error of the intensity can be approximated to be 20%. Furthermore, the majority of the counts during time-periods with steep spectra are caused by forward-penetrating particles. Hence, we apply the geometry factor for forward penetrating protons as displayed in Fig. 6 for the spectrum calculations in the following sections.

3. Application to SEP events

In this section we apply the described procedure to two events observed on May 17, 2012 (GLE 71) and January 6, 2014. To validate our method, the spectrum for the GLE 71 is compared to PAMELA results.

3.1. Event on May 17, 2012

On May 17, 2012 at 01:25 UT, the NOAA active region 11476, located at N11W76, produced a class M5.1 flare. Around 01:50 UT, the worldwide network of neutron monitors[3] detected the first ground-level enhancement in solar cycle 24. Relativistic electrons measured by EPHIN started to rise at 1:51 UT and triggered the Relativistic Electron Alert System for Exploration

---

[2] Data accessible at http://www.srl.utu.fi/projects/erne/erne.html

[3] http://www.nmdb.eu/

(Posner et al. 2009). The event was detected by a few neutron monitor stations, with the strongest signal detected at the South Pole. Count rates of the Neutron Monitors Apatity and South Pole and the EPHIN intensity measured by the integral channel, 25–50 MeV protons and relativistic electrons, are displayed in Fig. 11 left. While the duration of the event as recorded by the neutron monitors is a few hours, the intensity time profile of the EPHIN measurements remained above background for several days. As a result of SOHO commanding, no data were available after 7:00 UT.

Remote-sensing observations from the terrestrial point of view and from STEREO have been extensively discussed by Gopalswamy et al. (2013) and Shen et al. (2013). Gopalswamy et al. (2013) noted that the M5.1 flare started, peaked, and ended at 01:25, 01:47, and 02:14 UT, respectively. A metric type II radio burst was reported at 01:32 UT. The coronagraphs on STEREO A and on SOHO first observed the CME at 01:40 UT and 01:48 UT. The event onset time for near relativistic protons was between $1:43\,\mathrm{UT} < t_{On} < 2:00\,\mathrm{UT}$ (see also Papaioannou et al. 2014). The energy spectra as measured by PAMELA (Picozza et al. 2007) have been reported by Bazilevskaya et al. (2013) and indicate that protons with energies of up to 900 MeV and helium of up to 100 MeV/nucleon have been measured by PAMELA.

Figure 11 right shows the pre-event GCR background (May, 16: 0:00-24:00 UT, black diamonds) and the event spectra for the GLE71 on May 17, 2012 (03:00-05:00 UT, red squares) measured by SOHO/EPHIN as calculated by the method described in Sect. 2. While the background spectrum shows artifacts, the background-subtracted event spectrum does not show any instrumental features. The artifacts in the background spectrum below ≈ 100 MeV correspond to energy losses $\gtrsim 1.5$ keV/μm, which are caused by high-energy helium particles. In the event spectrum, this contamination disappears because of the spectral shape and the low helium-to-proton ratio (compare Sect. 2.2).

To compare them with the EPHIN intensities, the values provided by Bazilevskaya et al. (2013) for the time period 03:39–03:49 UT are also shown in Fig. 11 right (blue circles). Note that our method is applied to a longer timeseries than the PAMELA spectrum because the temporal resolution of our method is limited for statistical reasons. While the intensities agree perfectly at energies above 300 MeV, they differ by less than two sigma at lower energies. It is important to note that the spectral slope as well as the overall magnitude agree reasonably well, and therefore, regarding the simplicity of our method compared with the complex instrumentation, the results are promising. Therefore, we also applied the method to the event on January 6, 2014.

3.2. Event on January 6, 2014

The SEP event on January 6, 2014 was associated with a flare that occurred 25 degrees behind the western limb at coordinates S15W115, a broad CME with angular width ≥ 200 degrees, and a large EUV wave.

The EUV flare and the dome-shaped EUV-wave (Warmuth 2007) were clearly observed by both STEREO spacecraft and the SDO. The spacecraft constellation as well as the magnetic connectivity to the flare location is displayed in Fig. 12. The flare starts at 07:30 UT, showing a double maximum at 07:55 and 08:15 UT, and was accompanied by a coronal and IP type II radio burst as observed by CALLISTO and IZMIRAN (onset at 07:43 UT at ≥ 400 MHz), and SWAVES, respectively. The flare-associated type III radio bursts occur simultaneously with and

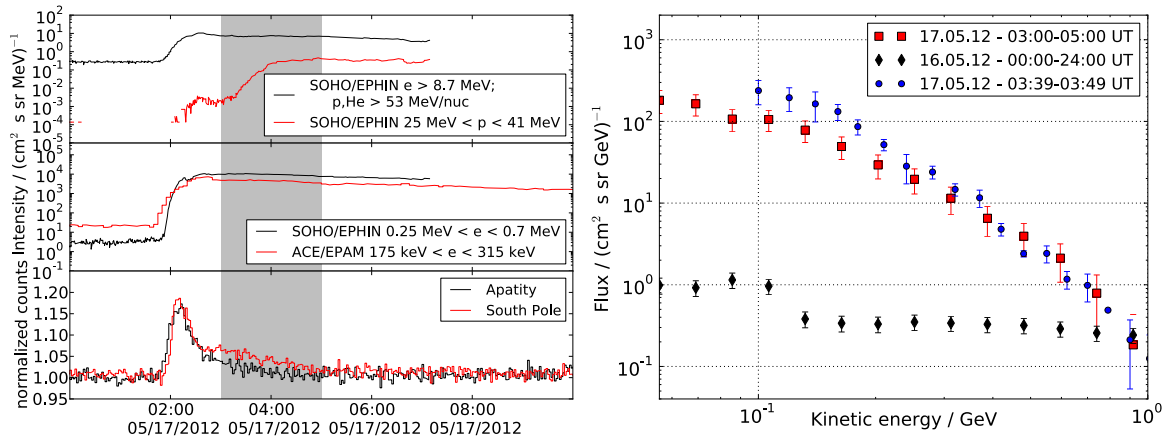P. Kühl et al.: Proton intensity spectra during the May, 2012 and January, 2014 SEP events

Fig. 11. *Left*: time profile of the GLE in May 2012. We present the integral channel and protons measured by SOHO/EPHIN (*top*), electrons measured by SOHO/EPHIN and ACE/EPAM (*middle*), and neutron monitor count rates. *Right*: calculated GCR background (black diamonds) and background-subtracted event spectrum (red squares). The PAMELA spectrum supplied by Bazilevskaya et al. (2013) is shown for comparison (blue circles).
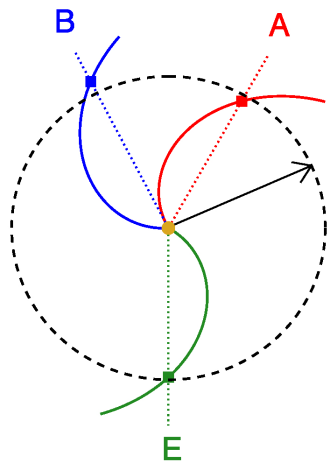

Fig. 12. Location of the flare (indicated by the arrow) with respect to the spacecraft constellation. The flare location was determined from the STEREO A image.

during the coronal/IP type II burst and were detected only at SWAVES at ≤16 MHz, suggesting that the type III generating electrons were accelerated and/or injected into the IP space by the propagating shock. Therefore it is plausible to assume that the type II/III bursts onset around 07:43 UT is the injection time of SEPs into IP space. The broad CME is discussed by Thakur et al. (2014). The associated in situ IP shock was detected at STA at 17:05 UT on January 8, but no in situ signatures were detected at STEREO B or at SOHO and ACE.

Figure 13 left displays the particle intensity time-profiles during the time period from 6 UT to 16 UT. In the lower panel, five-minute averages of the count rate of the South Pole neutron monitor are shown. The intensity of these particles remains above the Galactic cosmic-ray background from ∼8 to ∼10:45 UT, and the maximum intensity increase is ∼2%. In comparison to the neutron monitor, the middle panel displays the intensity time-profiles of near relativistic electron as measured by SOHO/EPHIN and ACE/EPAM. The energy range of EPHIN

and EPAM are 250 to 700 keV and 175 to 315 keV, respectively. The speed of these electrons is similar to that of the protons that caused the increase in the neutron monitor count rates. From the ACE measurements we found an onset time at 8:10 UT. Unfortunately, SOHO/EPHIN has a data gap during the event onset, with the first data available at 8:43 UT. The upper panel displays the time profile of the integral channel (black curve) and of 25 to 50 MeV protons (red curve). Marked by shading is the time from the beginning of data transmission at 8:43 to 10:45 UT, that is, the time period the neutron monitor count rates are higher than the GCR background.

The proton event spectrum is displayed in Fig. 13 right together with a background spectrum that was calculated for January 3, 2014. The GCR background spectrum again shows the contamination of relativistic helium at lower proton energies followed by a flat spectrum that is expected from the contribution of forward- and backward-penetrating protons. The event spectrum is characterized by a power-law-like distribution, with an increase of about two orders of magnitude below 100 MeV and a factor of 5 at 500 MeV with respect to the pre-event background. Above 500 MeV, the intensity values show a trend to be higher than the background, but the values are statistically limited. We were able to compare the GLE 71 spectrum with PAMELA measurements, but no proton spectra for this event are available to us. Thus it is important to discuss the potential influence of different components on our results. Relativistic helium is one of the components that may alter the result. If we assume as a worst case 10% for the helium-to-proton ratio, the calculated proton spectra above 700 MeV rule out a major contribution of helium. Electrons may alter the proton spectrum at higher energies. Since the contribution of electrons to the proton spectrum shows no strong energy dependence, a flattening of the calculated spectrum above 500 MeV is expected (see Fig. 9). Assuming a power law for the proton spectrum, the contribution of backward-penetrating particles should flatten the spectrum. However, as discussed above, the contribution of all these additional components is expected to be minor for solar energetic particle events (see Fig. 10).

From the flattening of the spectrum above 600 MeV, we conclude this spectral roll-over energy to be the highest energy to which particles are accelerated in the event. This finding is
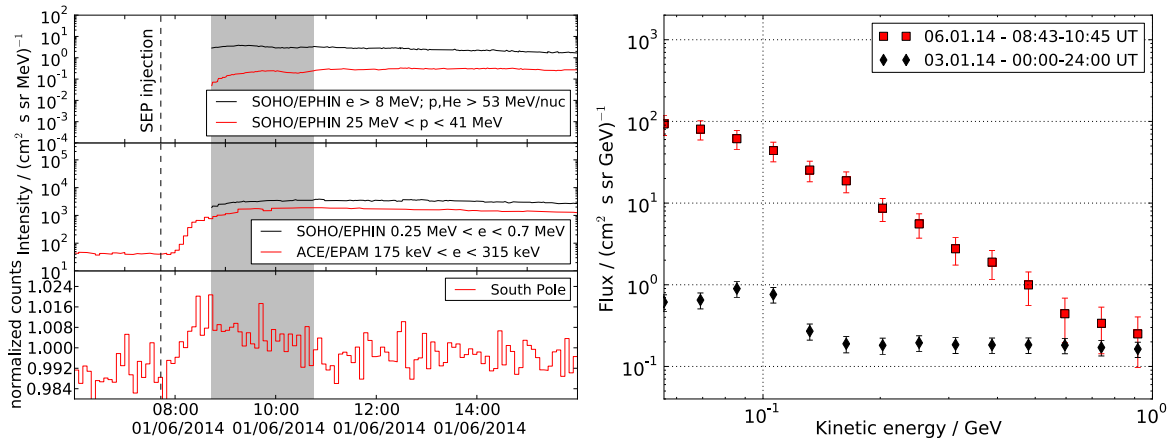
Fig. 13. *Left*: time profile of the event on January 6, 2014. We present the integral channel and protons measured by SOHO/EPHIN (*top*), electrons measured by SOHO/EPHIN and ACE/EPAM (*middle*), and neutron monitor count rates. The dashed lines indicates the injection time of SEPs into IP space (07:43 UT). *Right*: calculated GCR background (black diamonds) and background-subtracted event spectum (red squares).

supported by the fact that no statistically significant increase above the background is observed above this energy (i.e., the higher energy bins of the event and the background spectrum agree when the error bars are taken into account). This finding is supported by GOES measurements, which only show a weaker increase in intensity above 700 MeV compared to significant increases between 400 and 700 MeV (see Fig. 1a in Thakur et al. 2014).

4. Summary and discussion

Ground-level enhancements are solar energetic particle events that show a significant intensity increase at energies that can be measured by ground-based instrumentation, that is, by neutron monitors. The solar energetic particle event on January 6, 2014, which was measured by the South Pole neutron monitors, has opened the discussion in the community of how a GLE is defined[4]. In contrast to previous GLEs with significant count rate increases at several locations, there is no possibility to determine the energy spectra from ground-based measurements for the event on January 6, 2014 (e.g., Matthiä et al. 2009). Since the energy required to penetrate both the magnetosphere and the atmosphere of Earth varies from a few hundred MeV to several GeV based on the cutoff rigidity (i.e., latitudinal and longitudinal position as well as atmospheric pressure), there is an increasing need to derive proton energy spectra from spacecraft measurements in this energy range. Knowledge of the interplanetary energy spectrum of solar events is especially important for investigating particle transport in the magnetosphere and atmosphere as well as for the neutron monitor and the space weather community.

We showed that SOHO/EPHIN is well-suited to provide these proton spectra for the events on May 17, 2012 and January 6, 2014. Although the instrument was designed to measure stopping particles only, that is, protons up to 50 MeV, the telescope provides sufficient information for particles such as protons above 50 MeV that penetrate the instrument to extend the energy range. Using a GEANT 4 simulation, we determined the response function of electrons, protons, and helium for energies from 5 MeV to 100 MeV and from 50 MeV/nucleon to

1 GeV/nucleon for forward- and backward-penetrating particles. As a promising result, the simulation for forward-penetrating particles shows that protons can be unambiguously identified in the energy range from about 100 MeV to below 800 MeV. The calculations for particles (protons, helium, and electrons) penetrating the instrument from behind give a significant background and overlap in the energy range of interest. A clear example for these contributions are the cosmic-ray background spectra displayed in Figs. 11 and 13 with a prominent helium contribution below 120 MeV and a flat spectrum for higher energies due to the combination of forward and backward penetrating protons. The latter are in part produced by hadronic interactions of helium particles in the spacecraft material. To determine quiet-time GCR spectra, more detailed investigations are needed. Fortunately, long averaged spectra of solar energetic particle events tend to follow a power law or a Band function (Tylka et al. 2006; Band et al. 1993) with a spectral index γ above 3 (e.g., Tylka et al. 2006). The simulation indicates that the contribution of the backward-penetrating protons is lower than 20% for such steep spectra and is therefore lower than the contribution of the forward-penetrating protons. Since the response function for protons above 50 MeV is nearly constant (see Fig. 6), we derived a simplified inversion method from measured energy losses to kinetic energy and intensity.

The procedure was successfully applied to the GLE on May 17, 2012 and was validated against the PAMELA measurements. To shed some light on the discussion about the SEP on January 6, 2014, we also applied our method to this event. The resulting background-subtracted spectrum is shown in Fig. 14 in comparison to the background-subtracted spectrum for May 17, 2012. The ratio of the two spectra is also displayed in the figure. During the 2012 event, the intensities at 100 and 600 MeV are two and four times higher than during the 2014 event, indicating that the later spectrum steepens faster than that in May 2012. This softer spectrum results in a lower maximum energy, which is important for detecting an SEP event by ground-based instrumentation. From South Pole measurements there is no doubt that the event was recorded by ground-based measurements at an air pressure of 690 mBar and vertical cutoff rigidities below 1 GV (corresponding to 500 MeV for protons). If South Pole were the only location of a cosmic-ray detector at ground, such as

---

[4]   See Thakur et al. (2014) and http://nest2.nmdb.eu

P. Kühl et al.: Proton intensity spectra during the May, 2012 and January, 2014 SEP events
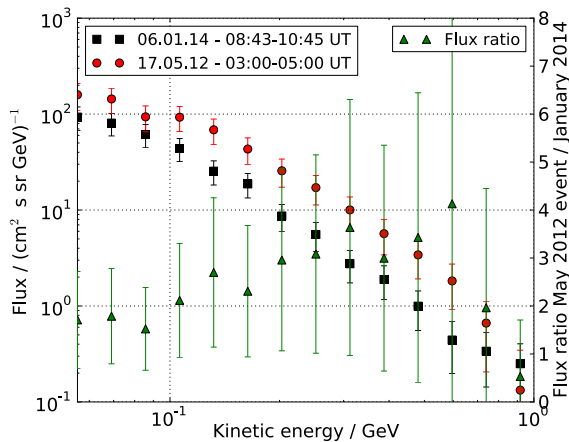

Fig. 14. Background-subtracted spectra for the events in May 2012 (red circles) and January 2014 (black squares) (see Figs. 11 and 13). The ratio of the two events is presented on the right-hand axis (green triangles).

MSL/RAD on Mars, which recorded the January 6 event (Posner 2014, priv. comm.) as well, the event would be counted as a ground-level enhancement, GLE 72. However, on Earth there is a network of neutron monitors, and therefore an SEP event is only called a GLE if more than one station records a significant count rate increase. In contrast to EPHIN, all neutron monitors measure a particle distribution that is altered by the terrestrial magnetic field and its atmosphere, leading to daily and seasonal variation, but also to short-term changes due to the terrestrial magnetic field and the atmospheric shielding that depends on different factors such as the atmospheric pressure.

However, knowing the interplanetary magnetic field direction at Earth and using the EPHIN spectrum in forward-modeling as done in Matthiä et al. (2009) would allow calculating the count rate increase not only for each neutron monitor, but also for other locations, allowing a more detailed investigation and more precise definition of GLEs.

References

Band, D., Matteson, J., Ford, L., et al. 1993, ApJ, 413, 281
Bazilevskaya, G. A., Mayorov, A. G., & Mikhailov, V. V. 2013, 33rd ICRC Proc.
Böhm, E., Kharytonov, A., & Wimmer-Schweingruber, R. F. 2007, A&A, 473, 673
Forbush, S. E. 1946, Phys. Rev., 70, 771
GEANT4 Collaboration 2006, CERN-LHCC 98-44, see also: http://geant4.cern.ch/
Gopalswamy, N., Xie, H., Akiyama, S., et al. 2013, ApJ, 765, L30
Matthiä, D., Heber, B., Reitz, G., et al. 2009, J. Geophys. Res., 114, 8104
Mewaldt, R. A., Looper, M. D., Cohen, C. M. S., et al. 2012, Space Sci. Rev., 171, 97
Moses, D., Droege, W., Meyer, P., & Evenson, P. 1989, ApJ, 346, 523
Müller-Mellin, R., Kunow, H., Fleißner, V., et al. 1995, Sol. Phys., 162, 483
Papaioannou, A., Souvatzoglou, G., Paschalis, P., Gerontidou, M., & Mavromichalaki, H. 2014, Sol. Phys., 289, 423
Picozza, P., Galper, A. M., Castellini, G., et al. 2007, Astropart. Phys., 27, 296
Posner, A., Guetersloh, S., Heber, B., & Rother, O. 2009, Space Weather, 7, 05001
Reames, D. V. 2013, Space Sci. Rev., 175, 53
Shen, C., Li, G., Kong, X., et al. 2013, ApJ, 763, 114
Thakur, N., Gopalswamy, N., Xie, H., et al. 2014, ApJ, 790, L13
Torsti, J., Valtonen, E., Lumme, M., et al. 1995, Sol. Phys., 162, 505
Tylka, A. J., Cohen, C. M. S., Dietrich, W. F., et al. 2006, ApJSS, 164, 536
Warmuth, A. 2007, in The High Energy Solar Corona: Waves, Eruptions, Particles, eds. K.-L. Klein, & A. MacKinnon (Berlin, Heidelberg: Springer), Lect. Notes Phys., 725, 107

4.2 SUPPLEMENTAL MATERIAL I: PHYSICAL MOTIVATION OF THE FIT FUNC-TION

The function used for fitting the relation between kinetic energy and energy loss of penetrating protons is physically motivated by the Bethe-Bloch equation. Fig. 16 shows GEANT4 simulation results of the stopping power as a function of $\beta \cdot \gamma$ for a silicon target as a 2D-histogram (compare to Fig. 6). The dashed line shows the results from the Bethe-Bloch equation (see Eq. 11), which is a good approximation for the average energy loss as a function of primary particle energy. Note that the Bethe-Bloch equation derives the mean energy loss of the Landau distribution and not the most probable energy loss and is thus still in agreement to the simulations at higher energies. A reasonable approach to find a functional relation between the total kinetic energy and the energy loss in a detector at these energies can be therefore be based on this equation.

The Bethe-Bloch equation

$$-\frac{dE}{dx} = \frac{4\pi}{m_e c^2} \cdot \frac{n z_P^2}{\beta^2} \cdot \left(\frac{e^2}{4\pi\epsilon_0}\right)^2 \cdot \left(\ln\left(\frac{2m_e c^2 \beta^2}{I \cdot (1-\beta^2)}\right) - \beta^2\right) \tag{11}$$

includes several material constants (the mean excitation potential I and the elec-
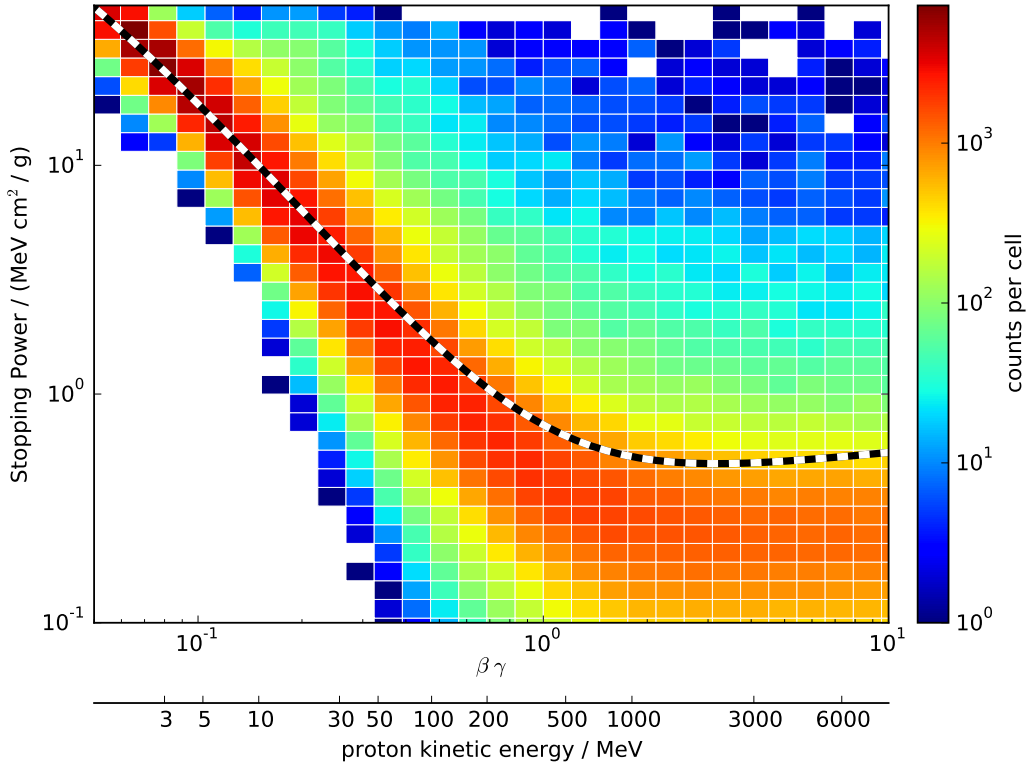

Figure 16: Proton stopping power in silicon as function of $\beta\gamma$ simulated with the GEANT4 toolkit. In the simulation, a proton beam with energies between 1 MeV and 10 GeV was shot on a 1 μm thick silicon target. A second axis with the kinetic energy of the proton has also been added. The dashed line represents results calculated with equation 11.
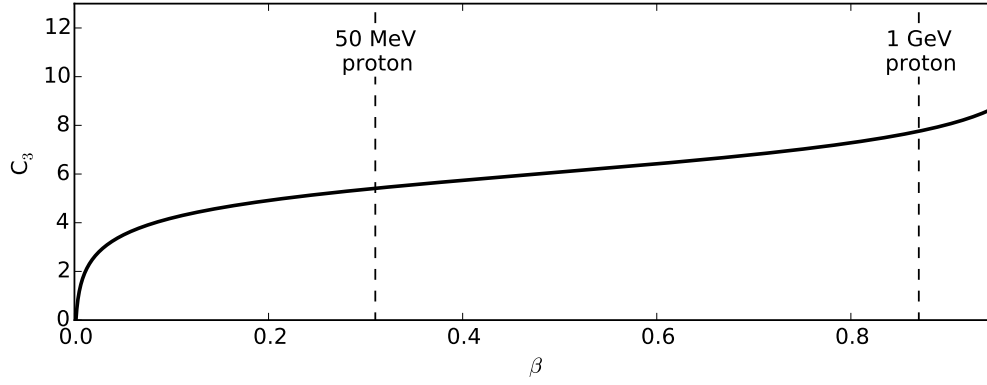
Figure 17: C_3 as function of β. The dashed lines indicate the β values for 50 MeV and 1 GeV protons.

tron density n which depends on the charge z_t, mass m_t and density ρ of the material) as well as quantities based on the primary particle (velocity $\beta = v/c$ and charge z_p).

For non-relativistic particles, their velocity $\beta = \frac{v}{c}$ is given by

$$\beta^2 = \frac{2 \cdot E}{m \cdot c^2} \tag{20}$$

with the mass m being the particles rest mass m_0 and hence constant. Equations 11 and 20 then lead to

$$-\frac{dE}{dx} = \frac{4\pi}{m_e c^2} \cdot \frac{nz_p^2}{\frac{2 \cdot E}{m \cdot c^2}} \cdot \left(\frac{e^2}{4\pi\epsilon_0}\right)^2 \cdot \left(\ln\left(\frac{2m_e c^2 \frac{2 \cdot E}{m \cdot c^2}}{I \cdot (1 - \frac{2 \cdot E}{m \cdot c^2})}\right) - \frac{2 \cdot E}{m \cdot c^2}\right) \tag{21}$$

$$= \frac{C_1}{E} \cdot \left(\ln\left(\frac{C_2 \cdot E}{(1 - \frac{2 \cdot E}{m \cdot c^2})}\right) - \frac{2 \cdot E}{m \cdot c^2}\right) \tag{22}$$

with

$$C_1 := \frac{4\pi}{m_e c^2} \cdot \frac{nz_p^2}{\frac{2}{m \cdot c^2}} \cdot \left(\frac{e^2}{4\pi\epsilon_0}\right)^2 \tag{23}$$

$$C_2 := \frac{2m_e c^2 \frac{2}{m \cdot c^2}}{I}. \tag{24}$$

Defining

$$C_3 := \ln\left(\frac{C_2 \cdot E}{(1 - \frac{2 \cdot E}{m \cdot c^2})}\right), \tag{25}$$

and assuming that C_3 is constant (compare Fig. 17), Eq. 22 can be further simplify to

$$-\frac{dE}{dx} = \frac{C_1}{E} \cdot \left(C_3 - \frac{2 \cdot E}{m \cdot c^2}\right) \tag{26}$$
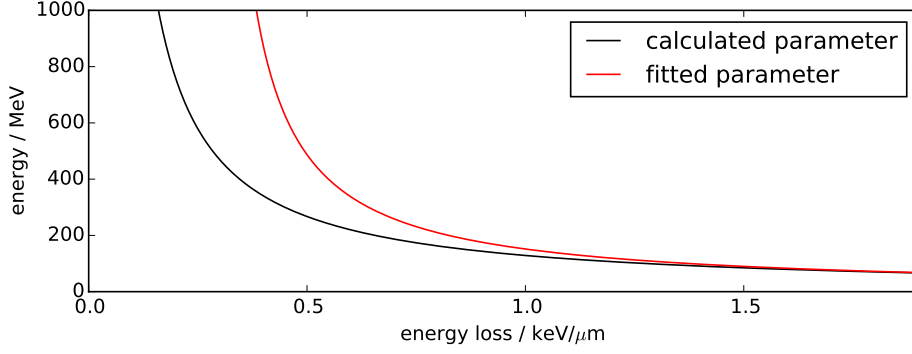
$$= \frac{-C_4}{E} - C_5 \tag{27}$$

Figure 18: Total kinetic energy as a function of the energy loss in silicon. Both, the function based on the calculations in this chapter (black) and the function resulting from the fit to simulation results from Kühl et al. [2015a] (red, see chapter 4.1) are presented.

with

$$C_4 := -C_1 \cdot C_3 \tag{28}$$

$$C_5 := C_1 \cdot \frac{2 \cdot}{m \cdot c^2}. \tag{29}$$

Eq. 27 can be solved for E:

$$E = \frac{C_4}{\frac{dE}{dx} - C_5} \tag{30}$$

Eq. 30 was used in Kühl et al. [2015a] (their Eq. 1) except for an offset parameter a which has been included in the paper.

However, if one calculates the parameter C_4 and C_5 (b and c in the paper, respectively), one finds some differences, especially for the C_5 (c) parameter. In Figure 18, the relations between total kinetic energy of a penetrating particle and its energy loss is shown for both, the calculated parameter (black) and the fitted parameter as presented in Section 4.1 (red). While the low energy part of the function is similar for both the calculated and the fitted parameter, the results differ at higher energies. This discrepancy can be explained by the fact that the parameter C_3 is not a constant but has a slight energy dependency, i.e. its value increases from 5 to 8 for energies between 50 MeV and 1 GeV (see figure 17). Furthermore the mass m is considered to be constant in the calculations which is not correct at high energies (e.g. for a 1 GeV proton).

4.3 SUPPLEMENTAL MATERIAL II: COMBINATION OF DATA SETS

As shown by Kühl et al. [2015a, Section 4.1], EPHIN is capable of measuring the proton energy spectrum from 100 up to 800 MeV using the integral channel. Furthermore, the nominal data products of the instrument which use the coincidence channels allow to derive the energy spectrum from 5 to 50 MeV (cf. Section 3.2). Thus, a combination of both measurement techniques is able to cover the spectrum over more than two orders of magnitude in energy which is especially helpful to study velocity dispersion of SEP events [see Reames, 2009b].

The time of arrival t_{obs} of a particle with the velocity v can by calculated with

$$t_{obs} = t_0 + L_s/v, \tag{31}$$

depending on the particle release time at the Sun t_0 and the path length L_s, which can vary between 1.1 and 2.2 AU for an observer at 1 AU due to different solar wind speeds [Reames, 2009a].

For the May 17th, 2012 SEP event, Carbone et al. [2013] have derived $L_s = 1.69$ AU and $t_0 = 01:41$ UT based on various measurements including a velocity dispersion analysis utilizing PAMELA data. Note, however, that Li et al. [2013] have calculated $L_s = 1.25$ AU for the same event utilizing electron measurements. Whether or not this discrepancies are related to different transport conditions for electrons and protons or to uncertainties in the calculation of the path length remains unclear. Hence, additional data to validate different transport conditions and/or simulations of the SEPs over the entire energy range is required.

In Fig. 19, the travel time of protons for this path length is presented. While relativistic protons with an energy of 1 GeV will reach the Earth in less than 20 minutes after their release at the Sun, 5, 10 and 20 MeV protons need at least 140, 100 and 60 minutes, respectively. However, since any scattering of the particles would increase their effective path length, these times represent the arrival of the earliest particles and hence mark the onset in intensity rather than the time of the maximum intensity.

Figure 20 shows the proton energy spectrum derived from EPHIN data for both stopping (circles) and penetrating particles (squares) for three different time intervals measured on May 17th, 2012 (for an intensity time profile of the event
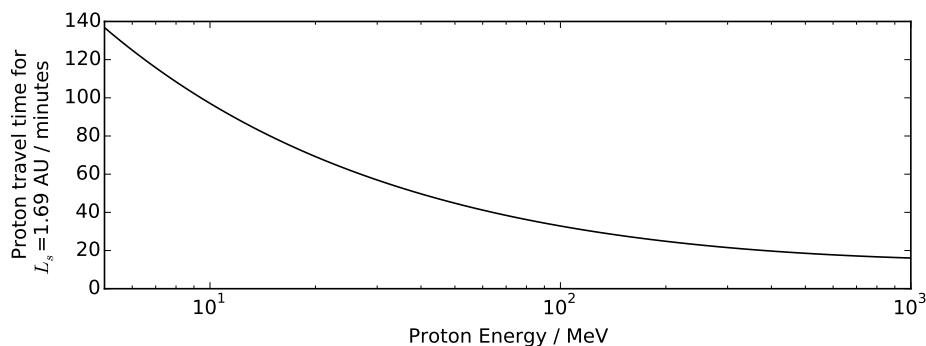

Figure 19: Proton travel time as function of proton energy for a Parker spiral with a length of $L_s = 1.69$ AU disregarding any scattering.
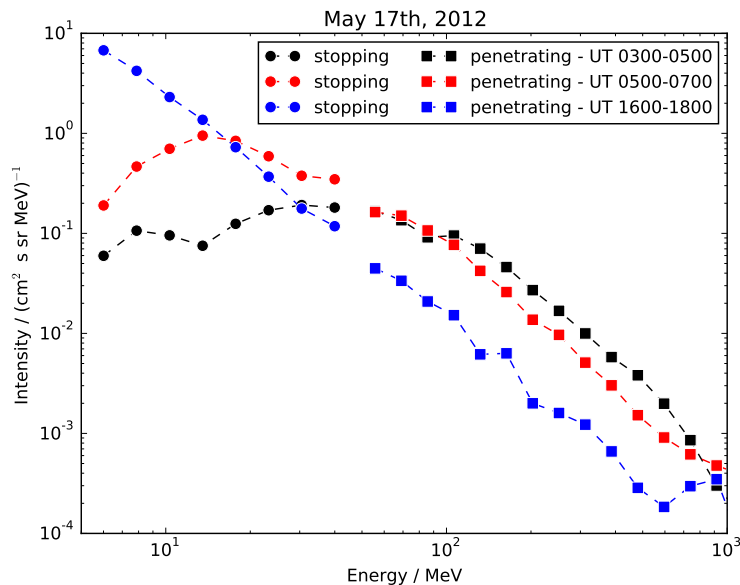
Figure 20: Proton energy spectra for three different time periods during the GLE event on May 17th, 2012 measured with SOHO/EPHIN. In addition to particles stopping in the instrument (i.e. the nominal energy range, circles), results for penetrating particles are presented (squares).

see Fig. 11 in Kühl et al. [2015a], i.e. page 37 in Section 4.1). Note, that no EPHIN data is available between 7:00 and 16:00 UT [see Kühl et al., 2015a]. Due to statistical limitations, the energy spectra can not be measured with time resolution similar to the PAMELA results given by Carbone et al. [2013] during the onset of the event. However, the velocity dispersion can still be seen in the later stages of the event. While the spectrum above 100 MeV has its maximum intensity in the first time interval, the lower energy part of the penetrating particles ($\leqslant$ 100 MeV) and the stopping particles above 20 MeV have a higher intensity in the second time interval. At the lowest energies (5 to 20 MeV) the intensity is the largest in the third time interval. Although neither the onset time nor the actual time of the maximum can be derived as function of energy due to statistical limitations, these measurements can be used to constrain and validate models of SEPs and their interplanetary transport.

Furthermore, the spectrum from 16:00 till 18:00 UT can be represented by a power law up to 800 MeV. The intensity increase above 800 MeV is caused by GCRs and thus not related to the event [Kühl et al., 2015a]. These consistent measurements over two orders of magnitude in energy and almost five orders of magnitude in intensity do not only show the new capabilities of EPHIN but can be used to study acceleration processes of SEP events since the spectral index (i.e. the slope of a power law fitted to the spectrum) measured in the interplanetary medium gives valuable information regarding the acceleration mechanism [e.g. Tripathi et al., 2013]. For a detailed study of the spectral indices of SEP events see Chapter 6.

HIGH ENERGY GALACTIC COSMIC RAY SPECTRA

The modulation of Galactic Cosmic Rayss (GCRs) in the heliosphere can be observed as energy and time dependent variation of the proton intensity at a given point in the heliosphere (as described in Section 2.1; see also Fig. 21). While the AMS and PAMELA instruments provide the measurements in the energy range between 250 MeV and above 1 GeV with unprecedented precision, long term measurements - i.e. on the time scale of the solar activity cycle (11 years) - are not available. Especially the influence of drift effects on a certain particle type can only be observed with continuous measurements over at least two solar cycles [Webber and Lockwood, 1988]. The influence of drift effects can be clearly seen in the GCR spectra presented in Fig. 21. While the maximum of the intensity at several hundreds of MeV during the A^+ solar minimum around 1996 is shaped like a plateau, the following A^- solar minimum around 2010 features a sharp maximum of the intensity (cf. Section 2.1).

The GCR spectra presented in figure 21 have been derived with the method developed by Kühl et al. [2015a, cf. Section 4.1], which is capable of providing energy spectra from 100 MeV up to 1 GeV during Solar Energetic Particle (SEP) events by utilizing the specific properties of the measured particle populations during SEPs. However, properties such as the shape of the energy spectrum and the composition of different particle types differ between SEPs and GCRs. Therefore, some of the arguments given by Kühl et al. [2015a] are not valid for the calculation of GCR spectra and thus an additional study of the application of the method and its limitations for measuring GCRs is required. Furthermore, a comparison with other measurements of the GCR spectra is also necessary for validation purposes. This study and a validation of the method for GCR spectra has been performed in the following publications:

Galactic cosmic ray quiet time spectra from 300 MeV up to above 1 GeV measured with SOHO/EPHIN

P. Kühl, N. Dresing, J. Gieseler, B. Heber and A. Klassen, Proceedings of Science, ICRC2015, id. 224

Own contribution: 90 %

Annual Cosmic Ray Spectra from 250 MeV up to 1.6 GeV from 1995 – 2014 Measured with the Electron Proton Helium Instrument onboard SOHO

P. Kühl, R. Goméz-Herrero and B. Heber, Solar Physics, Volume 291, Issue 3, pp.965-974 (2016), DOI: 10.1007/s11207-016-0879-0
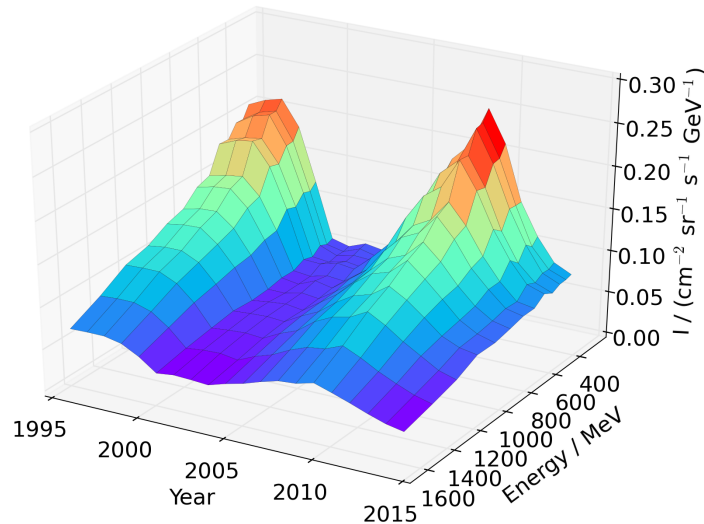
Own contribution: 90 %

Figure 21: Derived GCR proton spectra from 1995 to 2014. The figure is based on data from Kühl et al. [2016]

Short overview of the publications

The first publication is a feasibility study on deriving the GCR spectrum in the energy range from 300 MeV up to above 1 GeV based on EPHIN measurements. A short introduction and a section on the instrumentation and methodology are followed by a discussion on EPHIN spectra in comparison with PAMELA results.

In the second paper, the introduction summarizes GCR modulation with special emphasis on the new opportunities with the AMS and PAMELA instruments as well as drift effects. A short description of the EPHIN instrument is followed by a recap of the method presented in Kühl et al. [2015a] and estimation of the uncertainties for GCR spectra calculated with this method. Furthermore, a method to exclude SEP events from the data set is presented. A comparison with other missions is performed as validation. As a final result, the annual GCR proton spectra from 1995 to 2014 as shown in Fig. 21 have been presented and discussed. The key findings of the publications are:

- based on an error estimation, which utilizes input spectra from the Force Field Solution, EPHIN is capable of measuring GCR proton spectra between 250 and 1600 MeV

- the systematic error of the spectra are less than 20%, the statistical errors are estimated to be "*in the order of ≈ 10%, 2%, and 0.5% for a spectrum of a given day, month, and year, respectively.*"

- various balloon and spacecraft measurements during different phases of the solar cycle are in agreement to the new data under consideration of statistical and systematic errors

- annual GCR proton spectra from 1995 to 2014 and in the energy range from 250 - 1600 MeV are presented and discussed

PoS(ICRC2015)224

Galactic cosmic ray quiet time spectra from 300 MeV up to above 1 GeV measured with SOHO/EPHIN

Kühl, P.[*]**, Dresing, N., Gieseler, J., Heber, B., Klassen, A.**
IEAP, University of Kiel, 24098 Kiel, Germany
E-mail: kuehl@physik.uni-kiel.de

The solar modulation of galactic cosmic rays (GCR) can be studied in detail by long term variations of the GCR energy spectrum (e.g. on the scales of a solar cycle). With almost 20 years of data, the Electron Proton Helium INstrument (EPHIN) aboard SOHO is well suited for these kind of investigations. Although the design of the instrument is optimized to measure proton and helium isotope spectra up to 50 MeV/nucleon the capability exists that allow to determine energy spectra up to above 300 MeV/nucleon. Therefore we developed a sophisticated inversion method to calculate such proton spectra. The method relies on a GEANT4 Monte Carlo simulation of the instrument and a simplified spacecraft model that calculates the energy response function of EPHIN for electrons, protons and heavier ions. In order to determine the energy spectra the resulting inversion problem is solved numerically. As a result we present galactic cosmic ray spectra from 2006-2009. For validation, the derived spectra are compared to those determined by the PAMELA instrument.
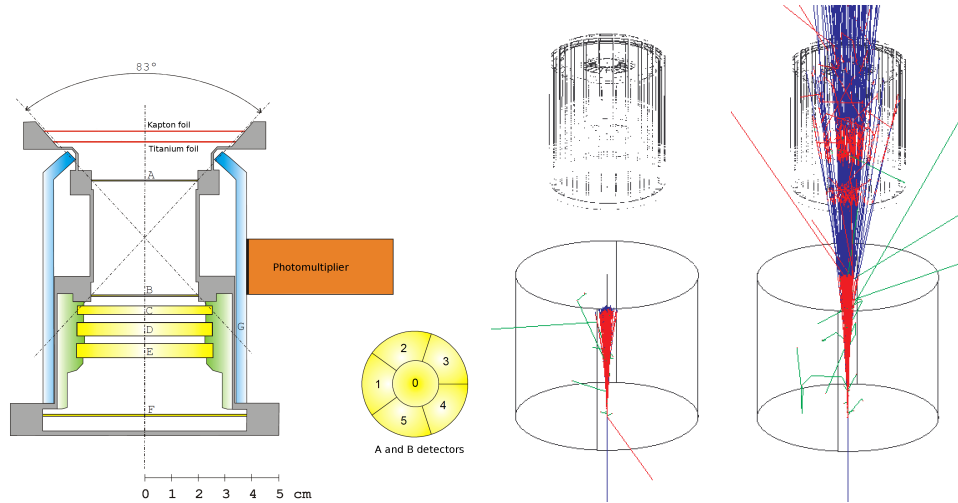
---

[*]Speaker.

Figure 1: Sketch of the EPHIN instrument [Müller-Mellin et al. (1995)] and the instrument as implemented in the GEANT4 simulation including a 10 cm block of aluminium to mimic the spacecraft. Simulated trajectories of a 150 MeV (center) and 200 MeV (right) proton beam including secondary particles created in the shielding are also shown. The colors represent the particle-type, protons (red), electrons (blue) and gammas (green).

1. Introduction

The intensity of galactic cosmic rays (GCR) in the inner heliosphere is well known to vary on time-scales of eleven years, anti-correlated to the solar activity cycle. This modulation of the GCR particles can be described by convection in the solar wind, adiabatic cooling, diffusion and drift effects [Parker (1965)], with the latter one also depending on the alignment of the interplanetary magnetic field and hence on the 22-year cycle of the solar dynamo. To investigate these drift effects, which are often neglected in models such as the force-field solution [Gleeson & Axford (1968)], long-term measurements of the GCR spectrum at energies of several hundreds of MeV are needed. In this work, we show that the Electron Proton Helium Instrument (EPHIN, [Müller-Mellin et al. (1995)]) aboard the Solar and Heliospheric Observatory (SOHO) with its mission life-time of almost 20 years is well suited for these kind of analysis. While the nominal maximum energy at which the instrument can determine spectra for protons is $\approx 50\ MeV$, a simple yet sophisticated inversion method based on GEANT4 simulations [GEANT4 Collaboration (2006)] can be used to derive proton energy spectra in the range between 100 MeV and 1 GeV during solar events [Kühl et al. (2015)]. However, in comparison to solar events, the GCR spectrum features a different spectral shape as well as different fluxes of electrons and helium particles which may corrupt the measurements. Thus, we will discuss the capabilities, limitations and systematic uncertancies of this method. Furthermore, preliminary results of the GCR spectra at several hundreds of MeV based on EPHIN data from 2006 to 2009 are presented in comparison to PAMELA data [Adriani et al. (2013)].
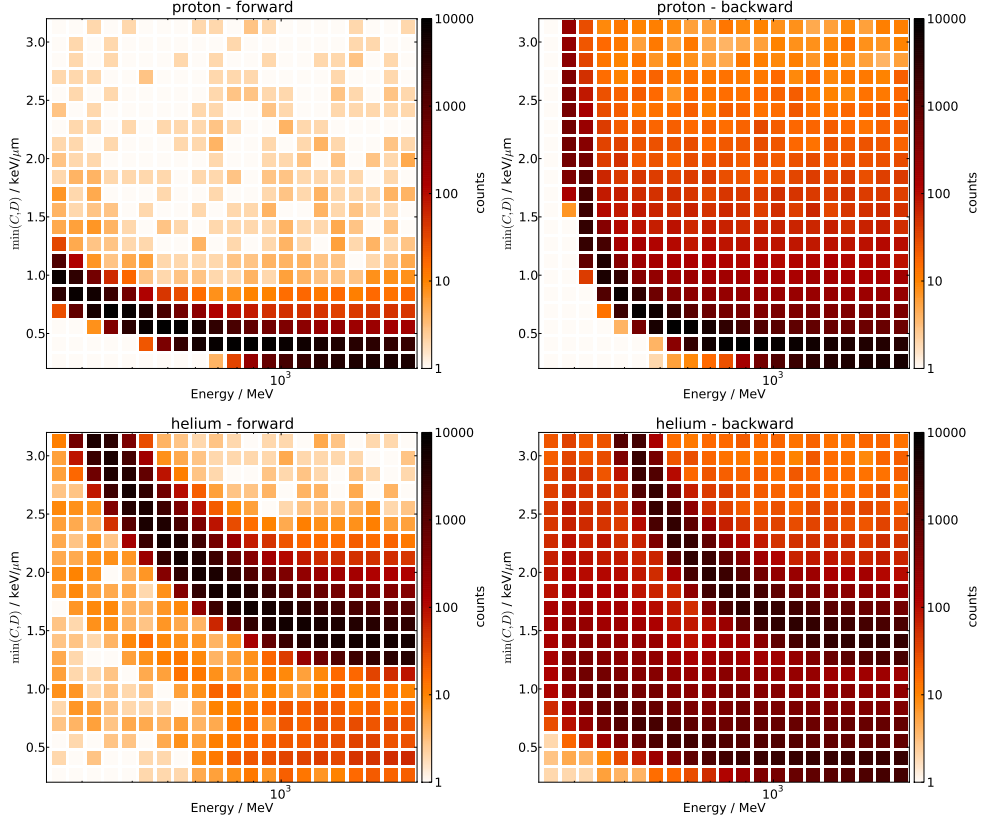
Figure 2: Simulation results for isotropic fluxes of protons (upper row) and helium particles (lower row) in front of (left column) and behind the instrument (right column). For each mono-energetic simulation (horizontal axis), a histogram of the resulting energy losses is shown color-coded.

2. Instrumentation and Inversion Method

A sketch of the EPHIN instrument is shown in fig. 1 (left). The instrument consists of a stack of silicon solid state detectors (SSDs, A-F) surrounded by an anticoincidence (scintilator, G). In this work, we focus on high energy particles that penetrate the entire instrument and deposit energy in every SSD. Since no information of the directionality of the measured particles is known, one can not simply distinguish between particles entering the instrument from the front ("forward particles", entering at detector A, exiting at detector F) and particles entering the instrument from behind ("backward particles", entering at detector F, exiting at detector A). Since backward particles first have to penetrate the entire spacecraft, they will reach the actual instrument with only a fraction of their initial energy which leads to systematic uncertancies in the derived spectra (c.f. [Kühl et al. (2015)] for details). To take this effects into account, a GEANT4 simulation has been set up, including a 10 cm aluminium block behind the instrument to mimic the spacecraft shielding as shown in fig. 1. In addition, the figure includes trajectories of simulated proton beams with
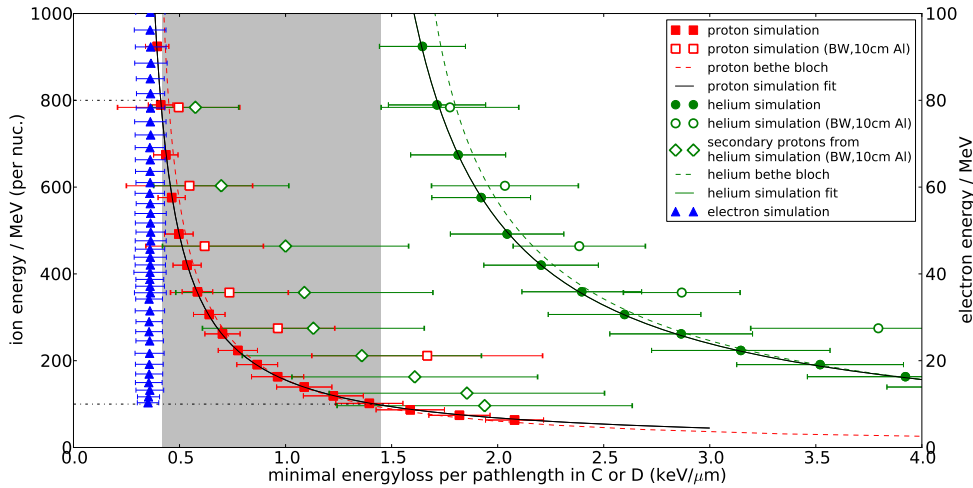
3

Figure 3: Relation between initial total energy and energy loss in the detector for protons (red), helium particles (green) and electrons (blue, right hand axis). The maximum energy of electrons is chosen to be 100 MeV based on measurements [Moses et al. (1989)]. Open symbols represent results from backward simulations, secondary protons caused by helium (green diamonds) are shown individually.

150 MeV and 200 MeV (center, right). The trajectories indicate that a backward proton needs to have an energy of roughly 150-200 MeV to penetrate both the shielding as well as all six SSDs. Hence, the energy response for forward particles (which need to have ≈ 50 MeV to penetrate the detector) differs from the response for backward particles, especially at lower energies.

To calculate the initial total energy of a penetrating particle based on the energy deposition in the detector, mono-energetic simulations with isotropic fluxes of protons, electrons and helium particles in front of (for forward particles) and behind the instrument (backward particles) have been performed individually. Results for protons and helium particles are shown in fig. 2. The figure shows the resulting counts (color-coded) as a function of the energy-loss and the initial total energy. For the energy loss, the minimum of the energy deposition in either the C or D detector is used to reduce noise based on the statistical nature of the energy loss (c.f. [Kühl et al. (2015)]). For both, protons and helium particles, the forward particles form a narrow population with a clear relation between total energy and energy loss, as expected based on the Bethe-Bloch equation. The backward particles on the other hand can cause a wide variety of energy losses due to the interaction in the spacecraft. Furthermore, at low energies the energy loss is enhanced as backward particles at this energies loose a significant fraction of their energy in the shielding. In addition, the distribution of backward helium particles shows a secondary population at typical energy losses of protons, which are caused by secondary protons created in the shielding via nuclear interactions.

 To quantify the relation between energy loss and total energy, the simulation results are summed up in fig. 3, where the initial energy is plotted as a function of the mean energy loss. Results for electrons (blue), protons (red) and helium (green) are shown individually. Backward and forward results are represented by filled and open symbols, respectively. The secondary protons caused by interaction of backward helium in the spacecraft are also shown (green diamonds). From the figure
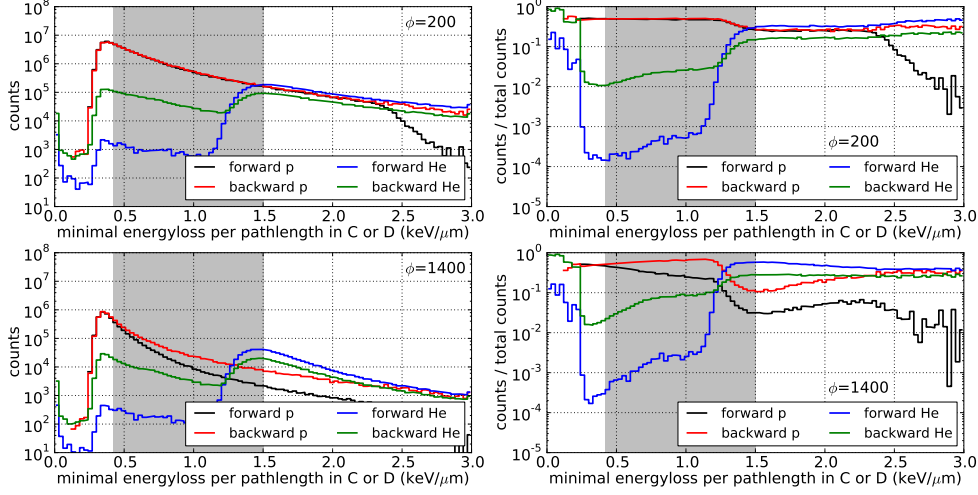
Figure 4: Expected counts (left: total counts, right: normalized counts) as function of energy loss for protons and helium particles entering the instrument from front and behind. Upper row shows results for solar minimum (ϕ=200 MV), lower row for solar maximum (ϕ=1400 MV).

it is clear that 1) energy deposition caused by electrons is limited to ≈ 0.4 keV/μm; 2) helium causes energy depositions above ≈ 1.4 keV/μm (except for secondary protons created by helium interacting in the spacecraft); and 3) that energy losses in the intermediate region (gray shaded in the figure) are almost entirely caused by protons. Furthermore, forward protons can be easily described by an analytic fit (red dashed line) and therefore, measured energy losses between 0.4 and 1.4 keV/μm can be converted into a proton spectrum with energies from ≈ 150 MeV up to over 1 GeV.

Note that energies below 150 MeV are corrupted by helium particles that have energy losses similar to low energy protons (c.f. fig. 3) which results in overestimated fluxes. Furthermore, measured spectra can have a small background of helium contribution in general in any energy bin. To address this issue, the amount of counted particles is estimated. Using the force-field solution [Gleeson & Axford (1968), Usoskin et al. (2011)], the energy spectra based on the particle type and the solar modulation (i.e. the solar modulation potential ϕ) is approximated. These spectra are then used as input for the GEANT4 simulation. The resulting number of particles counted in the simulations are shown in fig. 4 for both forward and backward penetrating particles during both, solar minimum (ϕ=200 MV) and solar maximum (ϕ=1400 MV). From the figure, it is obvious that the number of counts with energy losses below ≈ 1.2 keV/μm caused by helium particles is of the order of serveral % under both solar activity conditions and hence, the helium corruption above ≈ 150 MeV can be neglected.

In addition to the helium corruption, another systematic error is caused by backward penetrating protons. Fig. 3 indicates that the fit used to calculate the initial energy based on the energy loss deviates from the simulation results of the backward protons. The deviation increases to lower energies (especially below ≈ 300 MeV), while both datasets converge at higher energies.
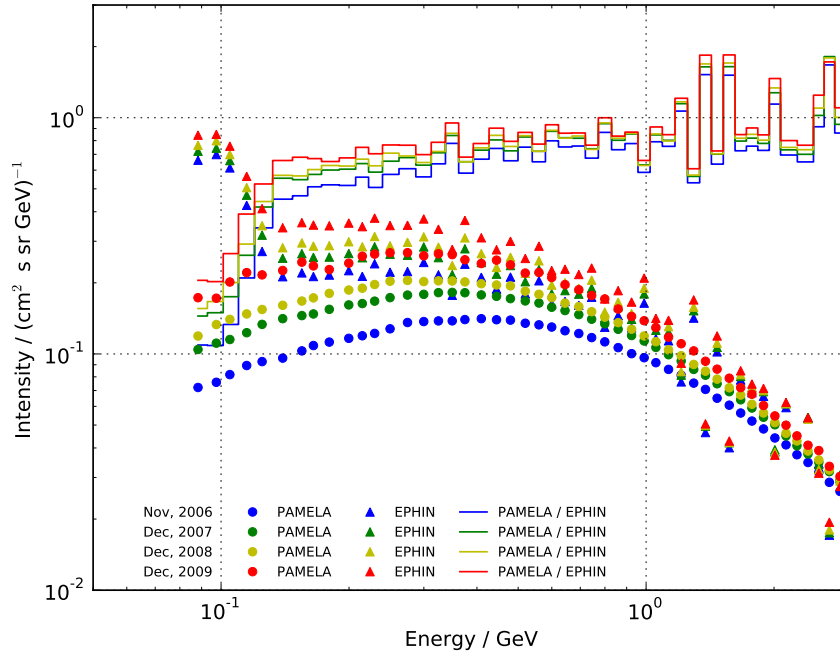
Figure 5: Proton spectra from 2006 to 2009, results from this work based on EPHIN data (triangles) in comparison to PAMELA results (circles, [Adriani et al. (2013)]). The solid lines indicate the ratio of both measurements.

Hence, unless a more sophisticated numerical inversion method is applied [Böhm et al. (2007), Köhler et al. (2011)], the presented method is limited to energies above ≈ 300 MeV for galactic cosmic ray spectra.

3. Results and Discussion

The presented method was applied to EPHIN data of four different time-periods (Nov 2006, Dec 2007, Dec 2008 and Dec 2009). The time-periods are chosen to cover several years in order to investigate the variation of the GCR spectra due to solar modulation. Furthermore, comparable PAMELA data is required to be available for validation. The resulting spectra are shown in fig. 5 in comparison to PAMELA data [Adriani et al. (2013)]. The solid lines represent the intensity ratio of both instruments.

Below ≈ 150 MeV the EPHIN spectra features an increased flux, roughly one order of magnitude higher than the PAMELA data. The increased fluxes show almost no variation over the the four years, indicating that the measured particles should have a high rigidity. Hence, in agreement to section 2, these particles can be identified as high energy helium particles that corrupt the proton spectra at these energies.

6

GCR quiet time spectra measured with SOHO/EPHIN   Kühl, P.

However, the energy range from ≈ 300 MeV up to > 1 GeV is in good agreement to the PAMELA data. While a general offset (EPHIN fluxes are 10-20% larger than PAMELA fluxes) occours, no systematic time- or energy-dependent deviations are found. Note that the variations above 1 GeV are of statistical nature due to the fine binning which was chosen in order to allow direct comparison with the PAMELA data.

In the intermediate energy-range (150-300 MeV), a clear trend with decreasing quality of the EPHIN data towards lower energies can be observed. The ratio indicates that the quality varies with the solar cycle and hence the overall shape of the GCR spectrum. In agreement to section 2, this effect can be identified to be caused by backward protons and the systematic error in the calculation of their total energy.

We conclude that using a simple yet sophisticated inversion method, SOHO/EPHIN is capable of measuring the galactic cosmic ray proton quiet time spectra in the energy range from ≈ 300 MeV up to over 1 GeV. However, for lower energies (e.g. 150-300 MeV) a more complex analysis of the instrument and its data is necessary.

Acknowledgments

References

[Adriani et al. (2013)] Adriani, O. et al., 2013, APJ, 765, 91

[Böhm et al. (2007)] Böhm, E., Kharytonov, A. & Wimmer-Schweingruber, R. F. 2007, A&A, 473, 673-682

[GEANT4 Collaboration (2006)] GEANT4 Collaboration 2006, CERN-LHCC 98-44, see also: http://geant4.cern.ch/

[Gleeson & Axford (1968)] Gleeson, L. J. & Axford, W. I., 1968, APJ, 154, 1011

[Köhler et al. (2011)] Köhler, J. et al., 2011, NIMP, 269, 2641-2648

[Parker (1965)] Parker, E., 1965, Planet. Space Sci., 13:9âĂŞ49

[Usoskin et al. (2011)] Usoskin, I. G. and Bazilevskaya, G. A. and Kovaltsov, G. A., 2011, JGR, 116, 2104

[Kühl et al. (2015)] Kühl, P. et al., 2015, A&A, 576, 120

[Moses et al. (1989)] Moses, D., Droege, W., Meyer, P. & Evenson, P. 1989, ApJ, 346, 52

[Müller-Mellin et al. (1995)] Müller-Mellin, R., Kunow, H., Fleissner, V., et al. 1995, Sol. Phys., 162, 483

CrossMark

Annual Cosmic Ray Spectra from 250 MeV up to 1.6 GeV from 1995 – 2014 Measured with the *Electron Proton Helium Instrument* onboard SOHO

P. Kühl[1] · **R. Gómez-Herrero**[2] · **B. Heber**[1]

Abstract The solar modulation of galactic cosmic rays (GCR) can be studied in detail by examining long-term variations of the GCR energy spectrum (*e.g.* on the scales of a solar cycle). With almost 20 years of data, the *Electron Proton Helium INstrument* (EPHIN) onboard the *SOlar and Heliospheric Observatory* (SOHO) is well suited for this kind of investigation. Although the design of the instrument is optimised to measure proton and helium isotope spectra up to 50 MeV nucleon^{-1}, the capability exists to determine proton energy spectra from 250 MeV up to above 1.6 GeV. Therefore we developed a sophisticated inversion method to calculate such proton spectra. The method relies on a GEANT4 Monte Carlo simulation of the instrument and a simplified spacecraft model that calculates the energy-response function of EPHIN for electrons, protons, and heavier ions. For validation purposes, proton spectra based on this method are compared to various balloon missions and space instrumentation. As a result we present annual galactic cosmic-ray spectra from 1995 to 2014.

1. Introduction

Hess (1912) discovered evidence of a very penetrating radiation later called cosmic rays, coming from outside the atmosphere. When Parker (1958) described the solar wind, theoretical research of cosmic rays began, stimulated by the beginning of *in-situ* space observations which have led to over four decades of important space missions, including the *Voyager*, *Ulysses*, and – more recently – the *Payload for Antimatter Matter Exploration and Light-nuclei Astrophysics* (PAMELA), and the *Alpha Magnetic Spectrometer* (AMS) missions. It is well known that at energies below several GeV the cosmic-ray flux is anti-correlated with

P. Kühl
kuehl@physik.uni-kiel.de

1   Institute for experimental and applied physics, University Kiel, 24118 Kiel, Germany

2   Space Research Group, University of Alcalá, 28871 Alcalá de Henares, Spain

🖄 Springer

the 11-year and 22-year solar-activity cycle due to the solar modulation (Heber and Potgieter, 2006; Heber, Fichtner, and Scherer, 2006). Thanks to the *Voyager* mission, uncertainties about the modulation volume (*i.e.* the heliosphere) as well as the local interstellar spectrum (LIS), became small (Stone *et al.*, 2013). Thus the remaining main question to pose is: How do charged particles propagate through the three-dimensional heliosphere and how do their transport and propagation vary with the particles' energy and the solar activity?

The transport of cosmic rays in the heliosphere can be described by Parker's transport equation (Parker, 1965). Physical processes that determine the measured flux at 1 AU are: i) Outward convection caused by the radially directed solar-wind velocity. ii) Adiabatic deceleration or acceleration depending on the sign of the divergence of the expanding solar wind. iii) Diffusion caused by the irregular heliospheric magnetic field. The diffusion coefficient depends on one's position, on the particles' rigidity (or energy), and on the solar activity (time). iv) Gradient and curvature drifts in the global heliospheric magnetic field, where the drift effects depend not only on the particles' rigidity, and charge but also on the phase of the 22-year solar-activity cycle, *i.e.* the orientation of the solar magnetic field above the solar poles ($A > 0$ or $A < 0$: Webber and Lockwood, 1988).

At 1 AU the different modulation processes manifest themselves in the shape of the measured energy spectra, *i.e.* in the range above 100 MeV nucleon^{-1} to below a few GeV nucleon^{-1}, and its temporal variations (Potgieter, 2013). Thus, in order to investigate these effects in more detail, cosmic-ray energy spectra covering the above-mentioned energy range at all different phases of the 22-year solar magnetic cycle are required. Furthermore, the energy coverage of measurements inside the Earth's magnetosphere depends on the position of the observer, due to the geomagnetic cutoff. Thus an instrument in interplanetary space is preferred. Since currently there is no dedicated instrumentation available, we extended the measurement capabilities of the *Electron Proton Helium INstrument* (EPHIN) onboard the *SOlar and Heliospheric Observatory* (SOHO), which was launched in 1995 and has been located at the Lagrangian point L$_1$ since 1996.

After a brief synopsis of the method and an error analysis, the method is validated in comparison to various other missions. Finally, annual proton spectra from 1995 to 2014 are presented.

2. Instrumentation

A sketch of the EPHIN instrument (Müller-Mellin *et al.*, 1995) is shown in Figure 1. The instrument consists of six silicon solid-state detectors surrounded by a scintillator for anti-coincidence. For particles that deposit their entire energy in the detector stack ("stopping particles"), the type of the particle measured can easily be identified using the dE/d$x - E$ method (Müller-Mellin *et al.*, 1995). However, this method is limited for protons to energies below 50 MeV. Above that energy, protons penetrate through the instrument, depositing only a fraction of their total kinetic energy. In order to overcome this limitation, a new method previously only used during solar events (Kühl *et al.*, 2015c), is adapted in such way that GCR proton spectra in the energy range from 250 MeV up to 1.6 GeV can be obtained.

3. Method

The method applied (for more details see Kühl *et al.*, 2015b, 2015c) relies on energy losses of particles that penetrate the entire instrument (*e.g.* detectors A–F are triggered, *cf.* Figure 1). Sophisticated Geant4 Monte–Carlo simulations (Agostinelli *et al.*, 2003) have been
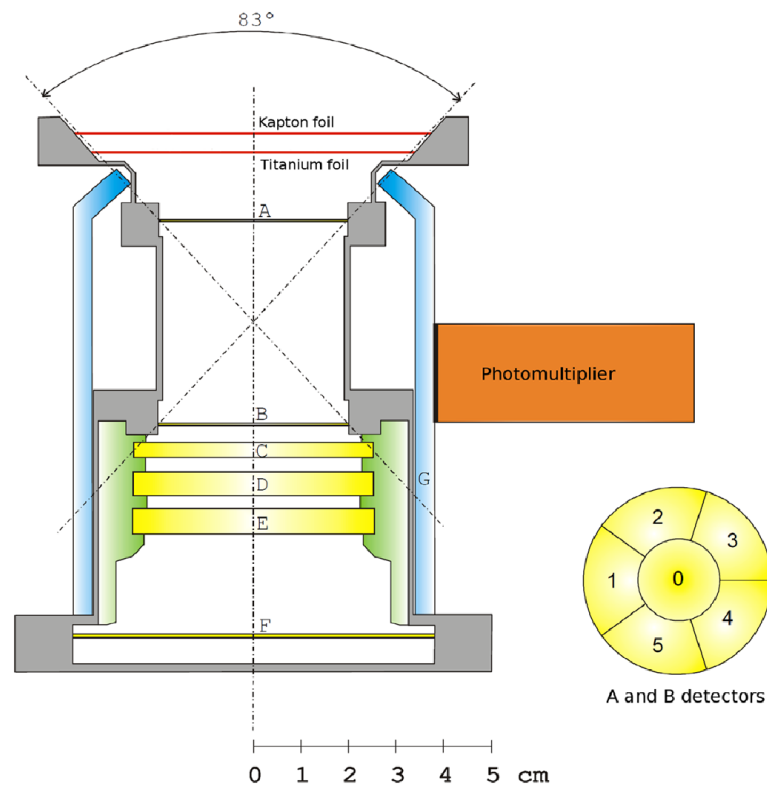
Annual Cosmic Ray Spectra Measured with SOHO/EPHIN

Figure 1 Sketch of the EPHIN instrument (adapted from Gómez-Herrero, 2003).

performed for electrons, protons, and helium ions. In addition to particles entering the instrument at detector A and exiting at detector F ("forward direction"), particles coming from behind the instrument (entering at F, exiting at A; "backward direction") are also considered. For the latter, the shielding of the SOHO spacecraft is taken into account by placing a 10-cm Al layer behind the instrument. The simulation results are summarised in Figure 2, where the simulated energy is presented as a function of the minimum energy loss in either the C or D detector. While the energy loss of electrons (blue triangles) is below $\approx 0.4 \ \mathrm{keV} \, \mu\mathrm{m}^{-1}$ independent of their energy, helium particles (green circles) typically lose more than $\approx 1.5 \ \mathrm{keV} \, \mu\mathrm{m}^{-1}$ and hence intermediate-energy losses are almost entirely caused by protons (red squares). Furthermore, the relation between total kinetic energy and energy loss for forward protons can be described by an analytical function fitted to the simulation results. Using this function, the total kinetic energy of a proton with a given measured energy loss can be estimated. However, especially at lower energies, protons passing the instrument in the backward direction differ significantly from forward-penetrating particles. In addition, secondary protons can be created by backward-directed helium in the shielding (green diamonds).

In order to determine the energy range in which the method can be applied and to estimate the systematic errors, further simulations using realistic proton and helium spectra as simulation input have been performed. The force-field solution (FFS: Gleeson and Axford, 1968; Usoskin, Bazilevskaya, and Kovaltsov, 2011) approximates the GCR spectra at Earth for a given local interstellar spectrum (LIS) and particle type as a function of a single variable, the modulation parameter [ϕ]. The solid lines in Figure 3 show FFS proton spectra for different ϕ: representing different solar-modulation conditions (*e.g.* $\phi = 400$ MV for solar minimum, $\phi = 1200$ MV for solar maximum). Furthermore, helium spectra with the same
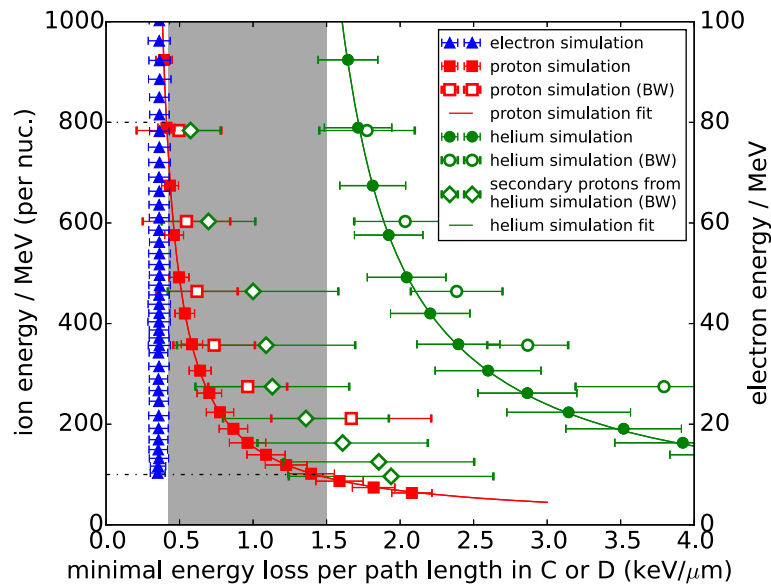
P. Kühl *et al.*

Figure 2 Relation between initial total energy and energy loss in the detector (adapted from Kühl *et al.*, 2015c).
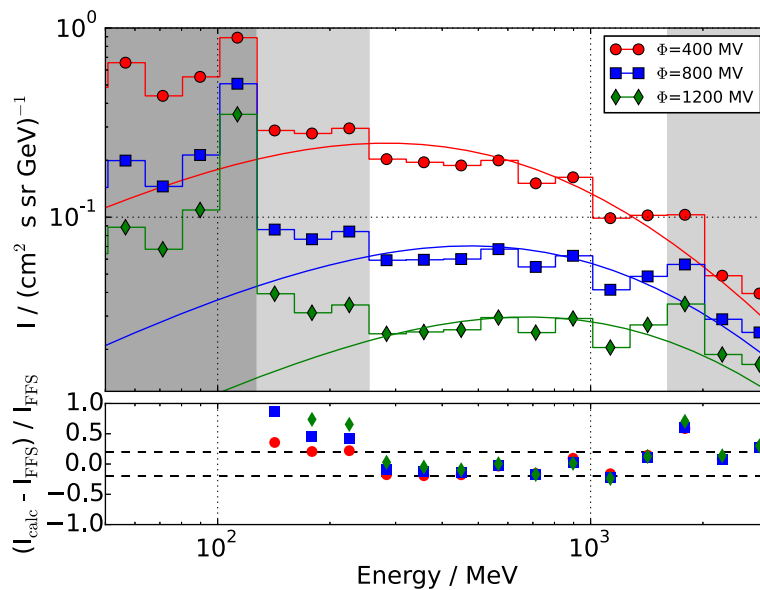
Figure 3 Input proton spectra (FFS, solid lines) and resulting spectra for different solar-modulation conditions. In the bottom panel, the relative deviation between input and model spectra is shown.

ϕ and an energy-independent He/p ratio of 25 % were included in the simulation. The artificial data were then analysed with the method described. The resulting spectra are shown as symbols in Figure 3. In the lower panel, the relative deviation between the resulting and the input spectra are presented. Below 130 MeV (marked by dark-grey shading in the figure), high-energy helium ions cause energy loss similar to that of low-energy protons and hence the intensity is heavily overestimated (Figure 2, *cf.* Kühl *et al.*, 2015b). In the energy range between 130 and 250 MeV (light grey), the intensity is slightly overestimated due to the influence of backward-directed protons (Kühl *et al.*, 2015c). Above 1.6 GeV (light

Annual Cosmic Ray Spectra Measured with SOHO/EPHIN

Figure 4 Example histograms of count rates of detector B for three selected months. The dashed lines show the threshold for solar events.

grey), the energy loss of different energies converges and thus, without any further corrections, the errors increase. However, based on the bottom panel of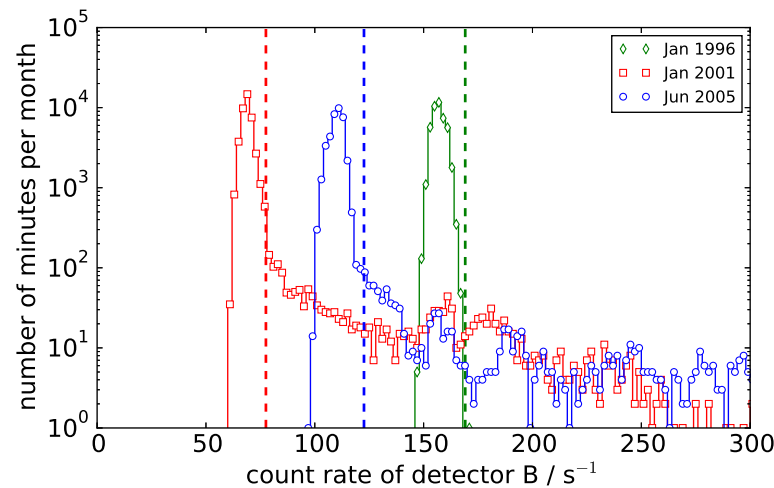 Figure 3, the systematic errors between 250 MeV and 1.6 GeV do not increase above 20 % for all solar-modulation conditions.

The statistical errors are of the order of $\approx 10\,\%$, $2\,\%$, and $0.5\,\%$ for a spectrum of a given day, month, and year, respectively.

In order to derive the GCR spectrum in a given time interval, solar events have to be excluded from the data set as they feature higher fluxes and a different spectral shape (Mewaldt *et al.*, 2012). Therefore, we analysed the count rate of detector B (*cf.* Figure 1) without any coincidence condition, which is available at one-minute resolution. The B-detector is sensitive to particles of low energy (Kühl *et al.*, 2015a) and hence the count rate is expected to rise during solar events. In Figure 4, histograms of the detector B count rate are shown for three different months. All three histograms feature a sharp peak at count rates between 50 and 170 counts per second. Those count rates are caused by the GCR and the variation of the position of the peak can be explained by solar modulation (Kühl *et al.*, 2015a). In addition, the histograms for January 2001 and June 2005 show the occurrence of count rates above 170 counts per second due to solar events. In our analysis, we have fitted a Gaussian to the peak of the count-rate distribution for every single month and excluded time periods, in which the count rates in detector B rose above 3σ over the mean of the Gaussian (dashed lines in Figure 4).

Following a similar approach to that used by Kühl *et al.* (2015c), Morgado *et al.* (2015) have analysed the response of the *Electron, Proton and Alpha Monitor* (EPAM) onboard the *Advanced Composition Explorer* (ACE) and the *Heliosphere Instrument for Spectra, Composition and Anisotropy at Low Energies* (HISCALE) onboard *Ulysses* to penetrating particles, focussing on the possibility of detecting anisotropies and onset times of the May 2012 GLE for particles above 1 GeV. However, those instruments do not have an integral coincidence channel and thus a clearly defined direction of arrival of the measured particles as well as the energy loss in several detectors is not known. Hence, the analysis of penetrating particles is much more complicated and an energy spectrum for penetrating particles cannot be derived.
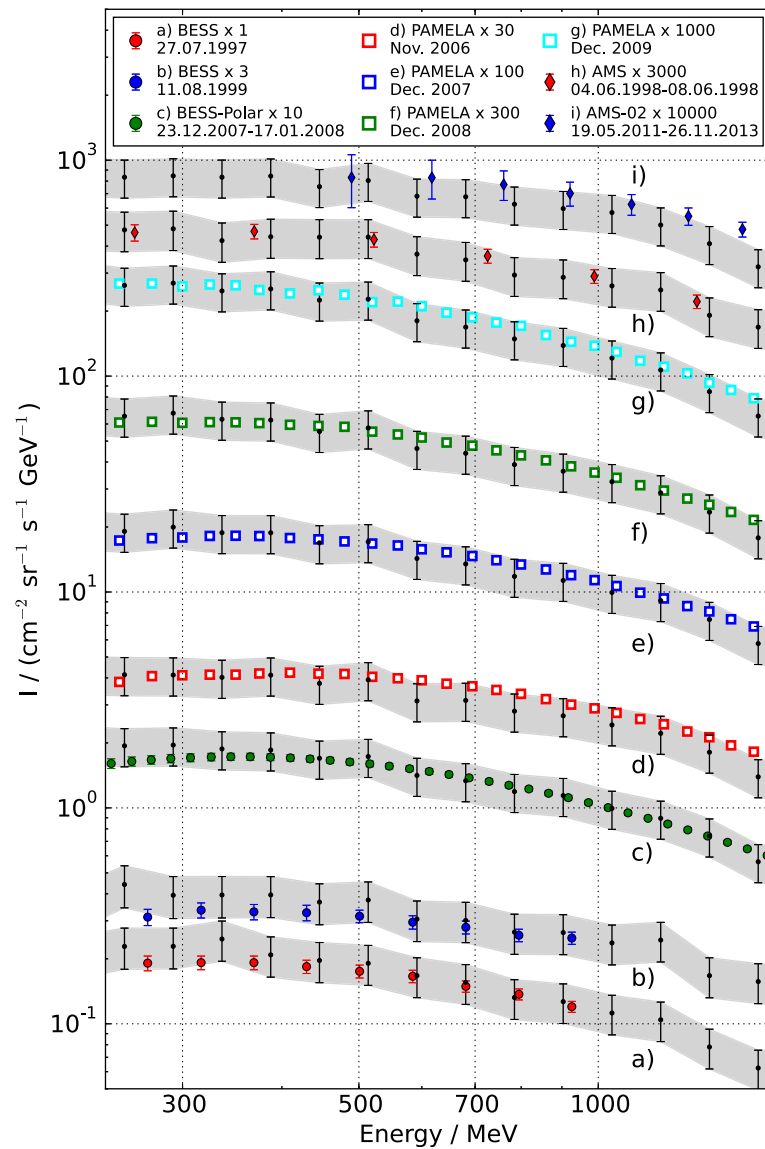
Figure 5 Proton spectra from AMS, AMS-02, BESS, BESS-Polar, and PAMELA in comparison to the derived EPHIN spectra (black). Spectra are scaled in the interest of greater clarity.

4. Results and Conclusion

In order to validate the derived spectra, Figure 5 shows data from various balloon missions (*Balloon-borne Experiment with Superconducting Spectrometer* (BESS): Shikaze *et al.*, 2007, and BESS-Polar: Abe *et al.*, 2016) as well as space-borne instruments (AMS: Alcaraz *et al.*, 2000, AMS-02: Aguilar *et al.*, 2015, and PAMELA: Adriani *et al.*, 2013) in comparison to EPHIN spectra (black) for the same time periods. The different spectra are scaled in the interest of greater clarity. The square sums of the statistical and the systematic error (20 % independent of energy) of EPHIN are shown as an error band (grey). Note that some BESS and BESS-Polar results are not shown, due to either gaps in EPHIN data or solar energetic-particle events in the given time period, masking the GCR spectra.

Based on this figure, EPHIN spectra are in good agreement with the other measurements when taking into account the errors. Since the different time periods cover different phases

Annual Cosmic Ray Spectra Measured with SOHO/EPHIN

Figure 6 A selection of annual proton spectra derived from SOHO/EPHIN data with the method presented.

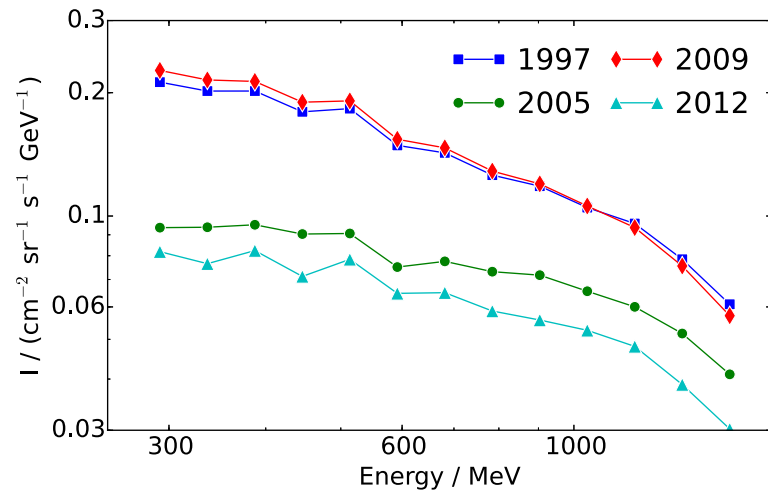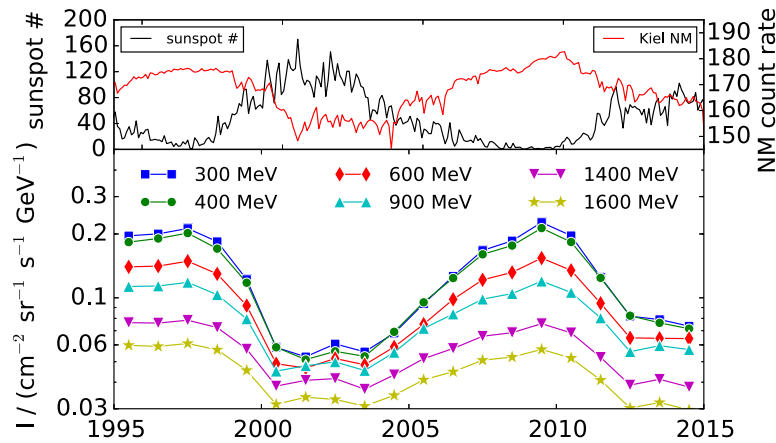**Figure 7** Upper panel: Monthly averaged sunspot number (black, left-hand axis), Kiel neutron-monitor count rate (red, right-hand axis). Lower panel: Proton intensity variations at different energies over the last two decades. The data were derived from SOHO/EPHIN data with the method presented.

of the solar cycle, it can be concluded that the method presented is valid for deriving spectra of galactic cosmic rays consistently.

Based on the method presented, annual GCR proton spectra from 1995 until 2014 have been derived. All annual spectra are available in Table 1.

A selection of spectra at different phases of the solar cycle is presented in Figure 6. While the two spectra at solar minimum (1997 and 2009) were obtained during different polarities ($A > 0$ and $A < 0$, respectively), the other two spectra (2005 and 2012) were obtained during the declining and rising phase of a $A < 0$ polarity phase (Hathaway, 2010). Especially the "record-high" spectrum of 2009 (Mewaldt *et al.*, 2010) represents a particular challenge for models to explain. In order to investigate the solar-cycle dependence in more detail, Figure 7 displays the monthly averaged sunspot number (solarscience.msfc.nasa.gov/SunspotCycle.shtml) and the count rate of the Kiel neutron monitor (www.nmdb.eu, both in the upper panel) in comparison to the yearly averaged derived intensities at selected energies between 300 and 1600 MeV (lower panel). Both the neutron-monitor count rate and the intensities at different energies measured by

Table 1 Annual proton spectra from 300 MeV up to 1.6 GeV from 1995 to 2014. Energy is given in MeV, differential intensity in $[\mathrm{cm^2\,sr\,s\,GeV}]^{-1}$. The systematic errors are approximated to be less than 20 %, statistical errors are less than 1 %.

E \Y	1995	1996	1997	1998	1999	2000	2001	2002	2003	2004
292	0.196	0.200	0.212	0.184	0.122	0.058	0.053	0.061	0.056	0.068
336	0.183	0.190	0.202	0.171	0.115	0.056	0.051	0.059	0.052	0.068
387	0.183	0.190	0.202	0.171	0.118	0.058	0.051	0.056	0.053	0.069
446	0.169	0.171	0.180	0.154	0.107	0.051	0.049	0.054	0.050	0.064
513	0.170	0.174	0.183	0.158	0.111	0.055	0.054	0.059	0.055	0.067
591	0.140	0.141	0.149	0.130	0.092	0.049	0.047	0.052	0.048	0.059
681	0.135	0.136	0.143	0.125	0.090	0.050	0.046	0.055	0.049	0.060
784	0.119	0.121	0.126	0.111	0.082	0.046	0.046	0.051	0.047	0.056
903	0.113	0.114	0.118	0.103	0.080	0.045	0.048	0.050	0.045	0.055
1040	0.101	0.101	0.105	0.096	0.073	0.046	0.048	0.049	0.046	0.054
1198	0.094	0.093	0.096	0.087	0.068	0.043	0.045	0.046	0.043	0.050
1380	0.076	0.076	0.078	0.072	0.057	0.038	0.041	0.042	0.037	0.043
1589	0.060	0.059	0.061	0.057	0.046	0.031	0.034	0.033	0.031	0.035

E \Y	2005	2006	2007	2008	2009	2010	2011	2012	2013	2014
292	0.094	0.127	0.167	0.186	0.227	0.196	0.125	0.082	0.079	0.074
336	0.094	0.122	0.159	0.176	0.215	0.185	0.126	0.077	0.076	0.072
387	0.095	0.124	0.160	0.176	0.213	0.183	0.124	0.082	0.076	0.072
446	0.090	0.113	0.144	0.159	0.190	0.163	0.109	0.071	0.071	0.067
513	0.091	0.117	0.147	0.160	0.191	0.166	0.116	0.078	0.075	0.073
591	0.075	0.098	0.122	0.132	0.154	0.135	0.094	0.065	0.064	0.064
681	0.078	0.097	0.117	0.126	0.147	0.129	0.092	0.065	0.065	0.064
784	0.073	0.086	0.104	0.112	0.129	0.114	0.083	0.059	0.062	0.061
903	0.072	0.084	0.099	0.105	0.120	0.106	0.080	0.056	0.059	0.057
1040	0.066	0.076	0.088	0.093	0.106	0.097	0.075	0.053	0.058	0.058
1198	0.060	0.070	0.080	0.085	0.094	0.085	0.065	0.048	0.049	0.046
1380	0.052	0.058	0.066	0.068	0.076	0.068	0.052	0.039	0.041	0.038
1589	0.041	0.045	0.051	0.053	0.057	0.052	0.041	0.030	0.032	0.030

SOHO/EPHIN are anti-correlated with the solar activity represented by the sunspot number (Heber and Potgieter, 2006; Heber, Fichtner, and Scherer, 2006). Furthermore, the intensity variation due to the solar modulation increases with decreasing energy. This behaviour is expected based on Parker's transport equation (Potgieter, 2013). Note that, similar to the neutron-monitor count rate, the intensity variations show features of drift effects such as the sharp peak in 2009 ($A < 0$) in contrast to the flatter maximum in 1997 ($A > 0$) (Webber and Lockwood, 1988).

Both figures show that the new data set allows us to investigate modulation processes at energies below the one obtained by neutron monitors and above the usual energy range from spacecraft instrumentation. Thus the two decades of data available, together with the unique position of SOHO outside the Earth's magnetosphere, offer the opportunity to validate solar-modulation model studies (*e.g.* Potgieter *et al.*, 2014).

Annual Cosmic Ray Spectra Measured with SOHO/EPHIN

Disclosure of Potential Conflicts of Interest   The authors declare that they have no conflicts of interest.

References

Abe, K., Fuke, H., Haino, S., Hams, T., Hasegawa, M., Horikoshi, A., *et al.*: 2016, Measurements of cosmic-ray proton and helium spectra from the BESS-Polar long-duration balloon flights over Antarctica. *Astrophys. J.* (submitted). arXiv. ADS.

Adriani, O., Barbarino, G.C., Bazilevskaya, G.A., Bellotti, R., Boezio, M., Bogomolov, E.A., *et al.*: 2013, Time dependence of the proton flux measured by PAMELA during the 2006 July-2009 December solar minimum. *Astrophys. J.* **765**, 91. DOI. ADS.

Agostinelli, S., Allison, J., Amako, K., Apostolakis, J., Araujo, H., Arce, P., *et al.*: 2003, GEANT4 – a simulation toolkit. *Nucl. Instrum. Methods Phys. Res., Sect. A* **506**, 250. DOI. ADS.

Aguilar, M., Aisa, D., Alpat, B., Alvino, A., Ambrosi, G., Andeen, K., *et al.*: 2015, Precision measurement of the proton flux in primary cosmic rays from rigidity 1 gv to 1.8 tv with the alpha magnetic spectrometer on the international space station. *Phys. Rev. Lett.* **114**, 171103. DOI.

Alcaraz, J., Alpat, B., Ambrosi, G., Anderhub, H., Ao, L., Arefiev, A., *et al.*: 2000, Cosmic protons. *Phys. Lett. B* **490**, 27. DOI. ADS.

Gleeson, L.J., Axford, W.I.: 1968, Solar modulation of galactic cosmic rays. *Astrophys. J.* **154**, 1011. DOI. ADS.

Gómez-Herrero, R.: 2003, Partículas energéticas en la heliosfera interna (1996 – 2000). Respuesta instrumental y observaciones del sensor ephin embarcado en el observatorio solar y heliosferico soho (esa-nasa). PhD thesis, University of Alcalá.

Hathaway, D.H.: 2010, The solar cycle. *Living Rev. Solar Phys.* **7**, 1. DOI. ADS.

Heber, B., Potgieter, M.S.: 2006, Cosmic rays at high heliolatitudes. *Space Sci. Rev.* **127**, 117. DOI. ADS.

Heber, B., Fichtner, H., Scherer, K.: 2006, Solar and heliospheric modulation of galactic cosmic rays. *Space Sci. Rev.* **125**, 81. DOI. ADS.

Hess, V.F.: 1912, Über Beobachtungen der durchdringenden Strahlung bei sieben Freiballonfahrten. *Phys. Z.* **13**, 1094.

Kühl, P., Banjac, S., Heber, B., Labrenz, J., Müller-Mellin, R., Terasa, C.: 2015a, Extended measurement capabilities of the electron proton helium INstrument aboard SOHO – understanding single detector count rates. *Cent. Eur. Astrophys. Bull.* **39**, 119.

Kühl, P., Dresing, N., Gieseler, J., Heber, B., Klassen, A.: 2015b, Galactic Cosmic Ray Spectra During Solar Cycle 23 and 24 – Measurement Capabilities of the Electron Proton Helium Instrument. In: *34th Int. Cosimic Ray Conf. 2015, Proc. Science*. pos.sissa.it/archive/conferences/236/224/ICRC2015_224.pdf.

Kühl, P., Banjac, S., Dresing, N., Gómez-Herrero, R., Heber, B., Klassen, A., *et al.*: 2015c, Proton intensity spectra during the solar energetic particle events of May 17, 2012 and January 6, 2014. *Astron. Astrophys.* **576**, A120. DOI. ADS.

Mewaldt, R.A., Davis, A.J., Lave, K.A., Leske, R.A., Stone, E.C., Wiedenbeck, M.E., *et al.*: 2010, Record-setting cosmic-ray intensities in 2009 and 2010. *Astrophys. J. Lett.* **723**, L1. DOI. ADS.

Mewaldt, R.A., Looper, M.D., Cohen, C.M.S., Haggerty, D.K., Labrador, A.W., Leske, R.A., Mason, G.M., Mazur, J.E., von Rosenvinge, T.T.: 2012, Energy spectra, composition, and other properties of ground-level events during solar cycle 23. *Space Sci. Rev.* **171**, 97. DOI. ADS.

Morgado, B., Filipe Maia, D.J., Lanzerotti, L., Gonçalves, P., Patterson, J.D.: 2015, The low energy magnetic spectrometer on Ulysses and ACE response to near relativistic protons. *Astron. Astrophys.* **577**, A61. DOI. ADS.

Müller-Mellin, R., Kunow, H., Fleißner, V., Pehlke, E., Rode, E., Röschmann, N., *et al.*: 1995, Costep – comprehensive suprathermal and energetic particle analyser. *Solar Phys.* **162**, 483. DOI. ADS.

Parker, E.N.: 1958, Dynamics of the interplanetary gas and magnetic fields. *Astrophys. J.* **128**, 664. DOI. ADS.

Parker, E.N.: 1965, The passage of energetic charged particles through interplanetary space. *Planet. Space Sci.* **13**, 9. DOI. ADS.

Potgieter, M.S.: 2013, Solar modulation of cosmic rays. *Living Rev. Solar Phys.* **10**, 3. DOI.

Potgieter, M.S., Vos, E.E., Boezio, M., De Simone, N., Di Felice, V., Formato, V.: 2014, Modulation of galactic protons in the heliosphere during the unusual solar minimum of 2006 to 2009. *Solar Phys.* **289**, 391. DOI. ADS.

Shikaze, Y., Haino, S., Abe, K., Fuke, H., Hams, T., Kim, K.C., *et al.*: 2007, Measurements of 0.2 20 GeV/n cosmic-ray proton and helium spectra from 1997 through 2002 with the BESS spectrometer. *Astropart. Phys.* **28**, 154. DOI. ADS.

Stone, E.C., Cummings, A.C., McDonald, F.B., Heikkila, B.C., Lal, N., Webber, W.R.: 2013, Voyager 1 observes low-energy galactic cosmic rays in a region depleted of heliospheric ions. *Science* **341**, 150. DOI. ADS.

Usoskin, I.G., Bazilevskaya, G.A., Kovaltsov, G.A.: 2011, Solar modulation parameter for cosmic rays since 1936 reconstructed from ground-based neutron monitors and ionization chambers. *J. Geophys. Res.* **116**, 2104. DOI. ADS.

Webber, W.R., Lockwood, J.A.: 1988, Characteristics of the 22-year modulation of cosmic rays as seen by neutron monitors. *J. Geophys. Res.* **93**, 8735. DOI. ADS.

5.3 SUPPLEMENTAL MATERIAL I: HEAVY IONS

While most studies of the solar modulation of GCR focus on protons, the interest in heavier nuclei and their intensity variations over the solar cycle is - despite their low abundance - growing due to their significant contribution to the total radiation dose in future long-duration deep space missions [Davis et al., 2001]. It must be noted that the term heavy ions is referring to helium and every ion heavier than helium in the GCR community. While various measurements are available for helium with energies above 1 GeV/nucleon (e.g. AMS [Aguilar et al., 2015], BESS [Sanuki et al., 2000], PAMELA [Adriani et al., 2011] and JACEE [Asakimori et al., 1998]), consistent long-term data for helium and heavier ions in the energy range most sensitive to solar modulation (100-1000 MeV/nucleon) is almost solely available from ACE/CRIS and ACE/SIS [Zhao and Qin, 2013]. Since both of these instruments are limited to energies below 500 MeV/nucleon, an extension of the method presented by Kühl et al. [2015a, 2016] to heavier ions could be used to bridge the energy gap between the different missions. Due to the continuous and concurrent data from both the SOHO and ACE missions over almost two solar cycles, the spectra of heavy ions could not only be used to estimate the radiation dose of future missions but to further study the solar modulation of GCRs including drift effects (see Section 2.1).

In order to explore whether or not energy spectra for heavy ions with energies above 50 MeV/nucleon up to 1 GeV/nucleon can be measured with the EPHIN instrument, Fig. 22 shows a histogram of the minimal energy loss per path length in detector C or D [cf. Kühl et al., 2015a] measured over 20 years (orange line). Based on the histogram derived with the FFS shown in Fig. 4 in Kühl et al. [2015c, see Section 5.1], the local maxima at ≈ 0.4 and ≈ 1.5 keV/μm can be linked to minimal ionizing protons and helium particles, respectively. This is further validated by GEANT4 simulations (coloured dots) and calculations based on the Bethe-Bloch (Eq. 11, dashed lines), which are presented as function of the total kinetic energy (right hand axis). Both the simulations and calculations confirm the two maxima to be caused by protons and helium particles. The simulation results of electrons (blue dots) show the same overlap of energy losses caused by electrons and protons discussed by Kühl et al. [2015a] and - in more detail - by Kühl et al. [2017].

The Bethe-Bloch calculations are also shown for heavier ions than helium, i.e. Boron, Carbon, Nitrogen, Oxygen and Neon. Note that the highest bin in the histogram shows an unusual high amount of counts since it reflects the overflow channel of the EPHIN detectors, i.e. every signal with an energy loss higher than ≈ 43 keV/μm is counted in this bin. Since the energy loss of minimal ionizing Boron (≈ 10 keV/μm) overlaps with the energy loss caused by the more abundant helium with energies of about ≈ 50 MeV/nucleon, an analysis of Boron is difficult. However, utilizing the measurements in more than the two detectors, Helium particles with energies of $\approx$ 50-200 MeV can be identified using the dE/dx-dE/dx method as indicated by Fig. 2 in Kühl et al. [2015a] (see page 31, Section 4.1). Furthermore, an analysis of the Neon peak (≈ 40 keV/μm) is difficult for statistical reasons. However, the histogram shows local maxima at the energy
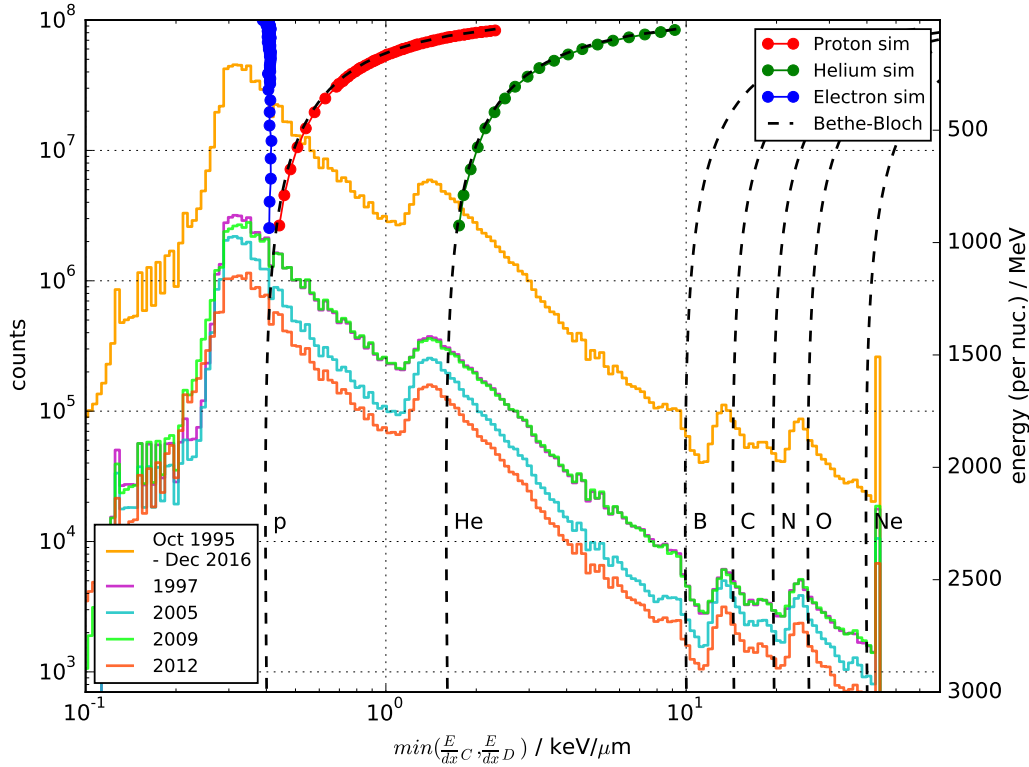
Figure 22: Histogram of the minimal energy loss per path length in detector C or D measured over 20 years (orange) and for four exemplary years. Note, that the highest bin is an overflow channel, i.e. every particle with an energy loss above 43 keV/μm is counted. The total kinetic energy of the particles corresponding to these energy losses are show with respect to the right hand axis based on the Bethe-Bloch equation (dashed lines) and on GEANT4 simulations (coloured dots).

loss of minimal ionizing Carbon, Nitrogen and Oxygen ions. The lower amount of counts for Nitrogen is in agreement to previous results from Mewaldt et al. [1981]; George et al. [2009].

In addition to the 20 year histogram, annual histograms for the years 1997, 2005, 2009 and 2012 are also shown as magenta, cyan, green and red lines, respectively. The energy loss histograms for the solar minimum years 1997 and 2009 are almost identical which is in agreement to the similarity of the proton spectra for these years as shown in Fig. 6 in Kühl et al. [2016, see Section 5.2]. The energy loss histograms of 2005 and 2012 have less counts than the ones of 1997 and 2009 (with 2012 showing the lowest number of counts) which is also consistent with the measured proton spectra. Since this temporal variation is also present at energy losses above 1 and 10 keV/μm, EPHIN is in principle sensitive to the solar modulation of helium and heavier ions, respectively.

 However, whether or not changes in the spectral shape of heavy ions can be observed with EPHIN has yet to be determined. Therefore, Fig. 23 shows the energy loss histograms of the four discussed years normalized to the measurements in 1997. Note that any variation at energy losses below 0.3 - 0.4 keV/μm could be related to the solar modulation not only of protons but also of electrons and
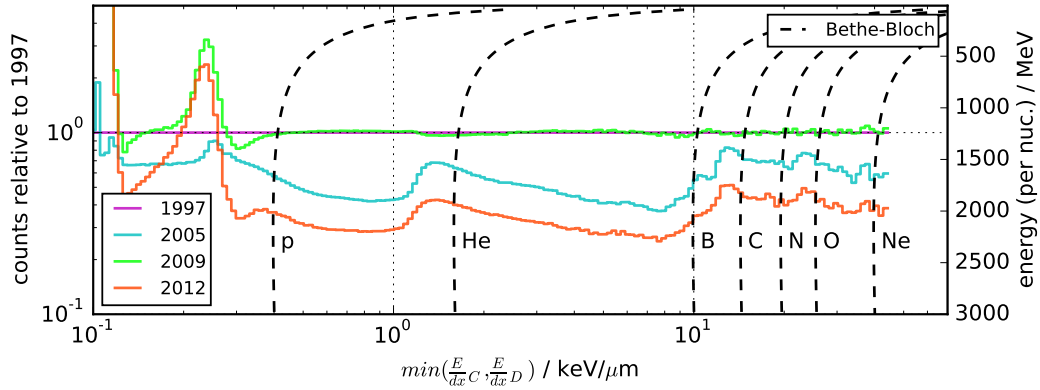
Figure 23: Histograms of the minimal energy loss per path length in detector *C* or *D* for four exemplary years relative to the counts in 1997. The total kinetic energy of the particles corresponding to these energy losses are show with respect to the right hand axis based on the Bethe-Bloch equation (dashed lines).

is therefore not discussed here. From the figure it is evident that not only the proton spectrum but also the energy loss histogram and hence the spectra of Helium, Carbon, Nitrogen and Oxygen measured in 1997 and 2009 are of similar shape. Since the effect of the solar modulation does increase with decreasing energy, the ratio of lower and higher energy particles, i.e. the slope of the histogram, should change depending on the solar cycle. Therefore, calculating the modulated energy spectrum of Helium is in principle possible since a change in the slope of the relative histograms is clearly seen between 2 and 8 keV/μm (e.g. for the years 2009 and 2012). It has to be noted, though, that the calculation of the Helium spectrum is especially complicated during SEP events since protons with energies above 50 MeV can dominate the counts for energy losses up to 3 keV/μm (cf. Fig. 10 in Kühl et al. [2015a, see Chapter 4.1]). For Carbon, Nitrogen and Oxygen an analysis of the histograms is more difficult due to the limited statistics as well as the significant overlap of their energy losses. Nevertheless, a comparison between the 2009 and 2012 histograms indicates that the measured data contains information regarding the energy dependent modulation of ions heavier than Helium as well.

In conclusion, future studies can follow the approach from Kühl et al. [2016] in order to derive the modulated energy spectra for Helium in the energy range from 50 up to above 1000 MeV/nucleon based on EPHIN measurements. For Carbon, Nitrogen and Oxygen however, only qualitative statements regarding the solar modulation of these heavy ions can be drawn while a detailed spectral analysis is not possible.

In the scope of this work, similar studies on heavy ion spectra of GCRs have been performed based on *HELIOS* data and are published in Marquardt et al. [2015a,b].

COMPILATION AND STATISTICAL ANALYSIS OF A SEP CATALOGUE

Ground Level Enhancements (GLEs) - the subclass of Solar Energetic Particle (SEP) events associated with the most energetic solar particles - have been studied in detail due to the continuous measurements of Neutron Monitors (NMs) over more than six decades (see Section 2.2). However, whether or not a SEP event is detected by NMs in order to be classified as a GLE does not only depend on the interplanetary energy spectrum of the particles accelerated during the event but also on the magnetospheric deflection of the particles and their interactions in the atmosphere. This has been also emphasized by Thakur et al. [2016], who found examples of a high energy SEP event not classified as GLE as well as a GLE not accompanied by any significant increase in the intensities above several hundreds of MeV. Thus a detailed statistical analysis of high energy SEP events based on longterm measurements not influenced by either the Earth's magnetosphere or the atmosphere is required in order to disentangle the different effects and to understand the nature of GLEs.

Kühl et al. [2015a] have shown that the energy range of the EPHIN instrument can be successfully extended to higher energies during SEP events by analysing two specific events, on May 17, 2012 and January 6, 2014. However, with more than 20 years of almost continuous data, the new measurement capabilities offer the opportunity of a statistical analysis of SEPs with an high energy component. For that purpose, a method of identification and criteria for a comparable parametrisation of these events have been developed. The identified events (see Fig. 24) are compared with different event lists [Vainio et al., 2013; Gopalswamy et al., 2015] and - if present - the increase caused in the neutron monitor count rates.

This statistical analysis of SEP events has been published in:
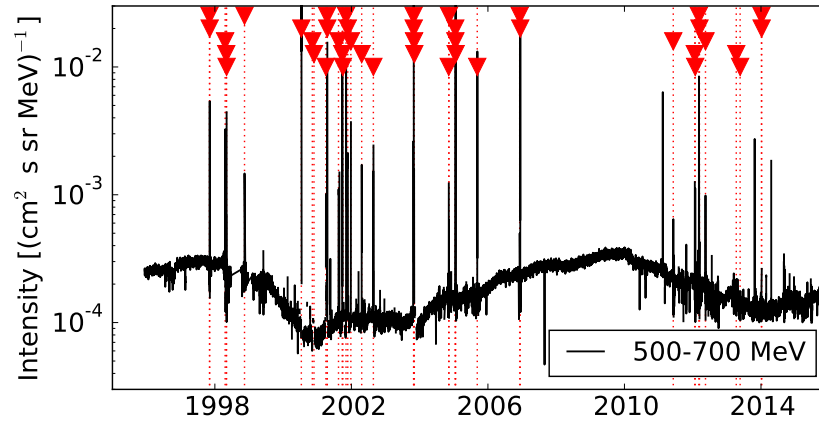
Figure 24: Intensity time profile of 500-700 MeV protons. The identified SEP events with protons above 500 MeV are marked with red triangles.

Short overview of the publication

An introduction of high energy SEP events is followed by a comparison of the new data with IMP8 and GOES data during different phases of a solar event and a new study on the electron contamination of the high energy proton data. Based on the method to identify SEP events introduced by Kühl et al. [2016], a list of 42 events (also shown in Fig. 24) with proton intensity increases above 500 MeV has been compiled and compared to other event lists. A statistical analysis of the spectral properties has been performed, distinguishing between GLEs and other events. For the GLEs, the increase in NM count rate has also been compared to the intensity derived in this study. The key findings of the publication are:

- the high energy data is valid during different event phases (e.g. event onset, declining phase), although statistically limited in the later phases

- the electron contribution to the data falsely interpreted as high energy protons is "*1) negligible below 500 MeV, 2) lower than 20% between 500 and 800 MeV, and 3) seriously uncertain above 800 MeV*"

- 42 SEP events with protons above 500 MeV have been found between 1995 and 2015

- GLEs have a similar distribution of spectral slopes compared to other events but a higher intensity at 500 MeV (typically above $2 \cdot 10^{-3}$ (cm^2 s sr MeV)$^{-1}$)

- a clear correlation between the derived intensity of 500 MeV protons with the relative NM count rate increase has been found for GLEs

CrossMark

Solar Energetic Particle Events with Protons Above 500 MeV Between 1995 and 2015 Measured with SOHO/EPHIN

P. Kühl[1] [ID] **· N. Dresing[1] · B. Heber[1] · A. Klassen[1]**

Abstract The Sun is an effective particle accelerator that produces solar energetic particle (SEP) events, during which particles of up to several GeVs can be observed. These events, when they are observed at Earth with the neutron monitor network, are called ground-level enhancements (GLEs). Although these events with their high-energy component have been investigated for several decades, a clear relation between the spectral shape of the SEPs outside the Earth's magnetosphere and the increase in neutron monitor count rate has yet to be established. Hence, an analysis of these events is of interest for the space weather and for the solar event community.

In this article, SEP events with protons accelerated to above 500 MeV were identified using data obtained with the *Electron Proton Helium Instrument* (EPHIN) onboard the *Solar and Heliospheric Observatory* (SOHO) between 1995 and 2015. For a statistical analysis, onset times were determined for the events and the proton energy spectra were derived and fitted with a power law.

As a result, we present a list of 42 SEP events with protons accelerated to above 500 MeV measured with the EPHIN instrument onboard SOHO. The statistical analysis based on the fitted spectral slopes and absolute intensities is discussed, with special emphasis on whether an event has been observed as a GLE. Furthermore, we are able to determine that the derived intensity at 500 MeV and the observed increase in neutron monitor count rate are correlated for a subset of events.

Keywords Solar cosmic rays · Ground level enhancement · Solar energetic particles

1. Introduction

The first solar energetic particle (SEP) event, which is now called a ground-level enhancement (GLE), was reported by Forbush (1946). GLEs are large SEP events that are observed by ground-based experiments such as neutron monitors (NMs). These detectors measure

P. Kühl
kuehl@physik.uni-kiel.de

[1]   Institute for Experimental and Applied Physics, University Kiel, 24118 Kiel, Germany

⚙ Springer

secondary particles that are produced when ions with energies above several hundred of MeVs create a nuclear cascade in the Earth's atmosphere. Since 1942, 71 GLEs have been reported (see *e.g.* https://gle.oulu.fi/); the largest measured increase above the pre-event background of about 4500 % was observed during GLE 5 on 23 February 1956 (Reames, 2013).

In order to fully understand the physics behind the particles resulting in GLEs, the chain of acceleration in the corona, the injection and transport in interplanetary space, and the propagation through the Earth's magnetosphere and atmosphere have to be understood. To this aim, Mishev, Usoskin, and Kovaltsov (2013) calculated the atmospheric yield function that describes the relationship between the intensity of protons and α-particles near Earth and the neutron monitor count rate, showing significant values for proton energies above 700 MeV. In agreement to these findings, investigations by Gopalswamy and Mäkelä (2014) using the *Geostationary Operational Environmental Satellite* (GOES) measurements of protons with energies above 700 MeV showed a good correlation between the occurrence of above 700 MeV SEPs and GLEs during Solar Cycles 23 and 24. However, in an extended study, Thakur *et al.* (2016) have reported two exceptions out of the 16 GLEs observed during Solar Cycles 23 and 24. The event of 6 May 1998 caused a GLE, but did not cause an increase in measurements above 700 MeV in GOES, and the 8 November 2000 event caused an increase of above 100 % with respect to the pre-event background in the GOES channel, but no increase in the neutron monitor network.

This dilemma, when a solar energetic particle event with a proton intensity increase at energies above 700 MeV observed in the near-Earth environment is recorded as a GLE and *vice versa*, also depends on the measurement capabilities of the available instruments. While NMs are a valuable tool to investigate GLEs, they have several limitations that are due to the indirect nature of detection. By measuring the count rate of secondary particles at the ground, a count which is created by interactions of high-energy particles with the atmosphere, NMs do not provide any direct information regarding the interplanetary spectrum of particles. In addition, the Earth's magnetosphere and hence the resulting geomagnetic cutoff rigidity (Lockwood and Debrunner, 1999) can vary over time, further increasing the uncertainties in the analysis of NM data. In addition to simulations of these magnetospheric and atmospheric effects, knowledge of the energy spectrum outside of the magnetosphere is therefore required. We recently showed that the *Electron Proton Helium Instrument* (EPHIN) is capable of measuring proton energy spectra up to 1 GeV (Kühl *et al.*, 2015a,b; Kühl, Gómez-Herrero, and Heber, 2016; Heber *et al.*, 2015), providing the necessary data for this type of investigation.

In this article, this new data are used to identify SEP events with protons above 500 MeV during the time period of 1995 to 2015. A detailed comparison with other event lists is carried out. Furthermore, a statistical analysis of the events based on their spectral properties and on the neutron monitor count rate increase for events resulting in GLEs is presented.

The article is structured as follows. In Section 2 the instrumentation and data are described. In Section 3 we identify events and compile an event list. Finally, in Section 4, we present a statistical analysis of the event list by analyzing the proton spectra, while in Section 5 we summarize our results.

2. Instrumentation and Data

2.1. Validation of High-Energy Proton Channels During Different Event Phases

The EPHIN instrument (Müller-Mellin *et al.*, 1995) onboard the *Solar and Heliospheric Observatory* (SOHO) consists of a stack of six silicon semiconductors labeled A to F that
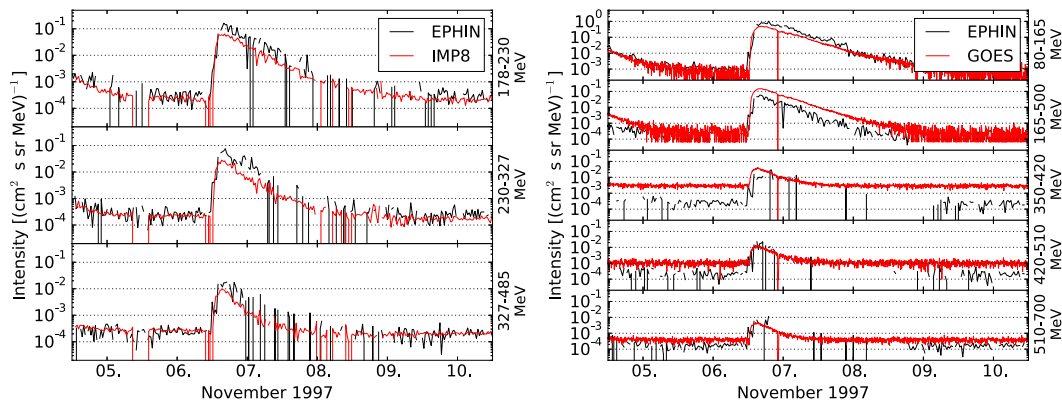
Figure 1 Proton intensities of the November 1997 GLE measured in different energy channels by IMP-8/GME (left panels, red curves) and GOES-9/EPS and GOES-9/HEPAD (right panels, red curves). For comparison, intensities for the same energy channels derived in this study from SOHO/EPHIN data (black curves) are presented.

are surrounded by an anticoincidence detector. The nominal energy range, between 5 and 50 MeV for protons, was extended to energies from 100 MeV to above 1 GeV with a method first presented by Kühl *et al.* (2015a). The method is based on particles that penetrate the entire detector stack, depositing only a fraction of their kinetic energy in the instrument. For these penetrating particles, the energy deposition in detectors C and D is taken as a measurement of the energy losses of these particles. It has been shown that for energy losses in a certain range, a reliable particle identification is possible for the penetrating particles. The energy losses can then be converted back into total kinetic energy with an uncertainty between 10 % (at 100 MeV) and 20 % (at 1 GeV, *cf.* Figure 9 in Kühl *et al.*, 2015a). For a more detailed description of the method, we refer to Kühl *et al.* (2015a) and Kühl, Gómez-Herrero, and Heber (2016).

The method has been successfully validated for the solar energetic particle events on 17 May 2012 and 6 January 2014 (Kühl *et al.*, 2015a). Kühl, Gómez-Herrero, and Heber (2016) have proven that the method is also applicable in the absence of solar events to derive galactic cosmic-ray (GCR) spectra from 250 MeV up to 1.6 GeV.

In this article, the method is used to identify solar energetic particle events with protons accelerated to at least 500 MeV. To apply this method to the entire SEP event, a further validation of the method during the entire solar event (including the rising and declining phases) is necessary since Kühl *et al.* (2015a) have only calculated event spectra for certain time periods. Since the method individually reconstructs the energy for every detected particle, it provides the opportunity of defining any arbitrary energy channel between ≈ 100 MeV up to above 1 GeV. Hence, intercalibration and comparison with other missions can be achieved rather easily.

For this purpose, Figure 1 shows the intensity of different energy channels during the 6 November 1997 SEP event (GLE 55) measured by the *Goddard Medium Energy Experiment* (GME: McGuire, von Rosenvinge, and McDonald, 1986) onboard the *Interplanetary Monitoring Platform 8* (IMP-8) in the left panels and by the *Energetic Particle Sensor* (EPS: Onsager *et al.*, 1996) and the *High Energy Proton and Alpha Detector* (HEPAD: Hanser, 2011) onboard GOES-9 in the right panels. In addition, the measured SOHO/EPHIN intensities in the same energy range are shown (black curves in both panels). The figure clearly shows that all three instruments measure the SEP event and that the intensity *vs.* time profiles are in agreement within a factor of two.
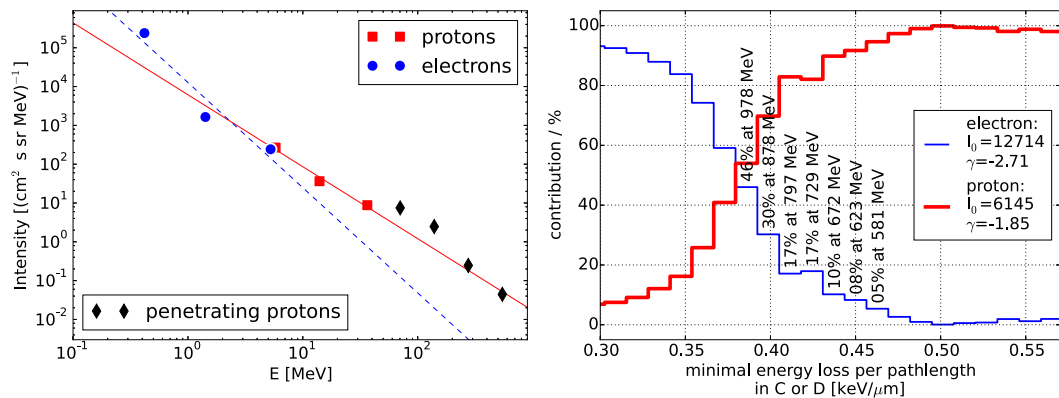
Figure 2 Left panel: proton (red squares) and electron (blue circles) spectra from the nominal data products and power law fits (lines) for GLE 69 on 20 January 2005 from 09:00 – 11:00 UT. For the same time period, the spectra of protons penetrating the instrument was also derived (black diamonds). Right panel: simulation results showing the contribution of protons and electrons for different energy losses based on the extrapolated spectra. The extrapolation was made with a power-law fit for both particle spectra with the fit results given in the legend. For some exemplary energy losses, the electron contribution and the proton energy related to that energy loss are shown by the text included in the vertical direction.

However, EPHIN systematically measures higher intensities around the maximum and in the decay phase of the event when compared to the IMP-8 instrument in all three channels. In contrast, the intensities are in agreement before and after the event. Hence we attribute the differences during the event to the so-called ring switching (for details see Müller-Mellin *et al.*, 1995).

It is important to note that the pre-event background measured by GOES is an order of magnitude higher than the backgrounds given by EPHIN and the IMP-8 instrument, as has been described by Sandberg *et al.* (2014). Furthermore, the 30-minute averaged data from SOHO/EPHIN have statistical limitations, especially in the decay phase of the event.

2.2. Electron Contamination of the High-Energy Proton Measurements

Kühl *et al.* (2015a) have mentioned a possible influence of electron fluxes above 10 MeV on the high-energy proton data during solar events, but this issue has not been quantified yet. Heber *et al.* (2015) showed that there are discrepancies in the derived proton spectrum during GLE 69 between SOHO and neutron monitors above 700 MeV, while GOES and SOHO agree with each other at lower energies. The increased flux above 700 MeV is believed to be caused by electrons above 10 MeV that are associated with the same SEP event that causes similar energy losses in the detector compared to those of high-energy protons. Therefore, the influence of electrons on the derived proton flux above 700 MeV has to be taken into account, and a study of this effect is necessary before a detailed analysis of the spectral properties can be performed.

For this purpose, Figure 2 (left panel) presents electron (blue circles) and proton (red squares) spectra based on the nominal data products from the EPHIN instrument during the GLE 69 on 20 January 2005 from 09:00 – 11:00 UT. The event has one of the highest electron contributions of the events investigated in this study and can therefore be considered as the worst-case scenario. The spectra were fitted with a power law and have been extrapolated to higher energies. We note that although the derived proton spectra based on the penetrating particles (black diamonds) are in agreement with the power law fitted to the proton spectrum

below 50 MeV, a softening in the proton spectrum at higher energies (*e.g.* a double power law) would increase the electron contribution. Using the fitted spectra as input for a Geometry and Tracking 4 (GEANT4) Monte Carlo simulation (GEANT4 collaboration, 2006) of the instrument, we derived the contribution of both protons and electrons to energy losses in the C and D detectors. As a result, Figure 2 (right) shows the contribution of electrons (blue) and protons (red) dependent on the energy loss. For some illustrative energy losses, the electron contribution and the proton energy related to that energy loss are shown by the text included in the vertical direction. The figure shows that the electron contribution to the high-energy proton spectra is: 1) negligible below ≈ 500 MeV, 2) lower than 20 % in the energy range from 500 to 800 MeV, and 3) very strong above 800 MeV. Hence, proton intensities above 800 MeV should be considered as upper limits during solar events.

3. Identification Method of > 500 MeV Proton Events

3.1. Event Detection

In order to identify SEPs with protons accelerated to energies above 500 MeV, a histogram of hourly intensities in a defined $500 - 700$ MeV range from 1995 to 2015 is presented in Figure 3. The histogram indicates that most of the time, the measured intensity is in the range of $0.7 - 4 \cdot 10^{-4}$ (cm^2 s sr MeV)$^{-1}$. In agreement with Kühl, Gómez-Herrero, and Heber (2016), these intensities correspond to the GCR background. The variation of the peak position over different years as indicated by annual histograms can be explained by solar modulation (Heber and Potgieter, 2006; Heber, Fichtner, and Scherer, 2006). While intensities below this main population correspond to either GCR depressions during the passages of interplanetary coronal mass ejections (Forbush decreases, Cane, 2000) or instrumental effects such as a high dead time of the electronics, higher intensities are related to SEPs.

In this study, events have been identified by requiring that at least two hourly averaged intensities in a six-hour interval are above a threshold of $4 \cdot 10^{-4}$ (cm^2 s sr MeV)$^{-1}$. Using this identification technique, we identified 42 solar particle events in the time between the start of the mission (December 1995) and 1 October 2015. It has to be noted that communication with SOHO was lost for several months during 1998 and, hence, no EPHIN data are available for this time period.

3.2. The Event List

Figure 4 presents the time profile of the proton intensity in the energy range from 500 to 700 MeV over the past 20 years. In agreement with Figure 3, the variation of the GCR

Figure 3 Histograms of the hourly proton intensities in the energy range from 500 to 700 MeV based on SOHO/EPHIN data. Shown are a histogram of the entire mission, as well as three annual histograms, as indicated in the inset.
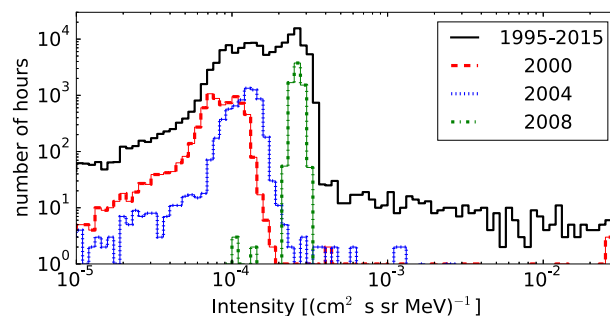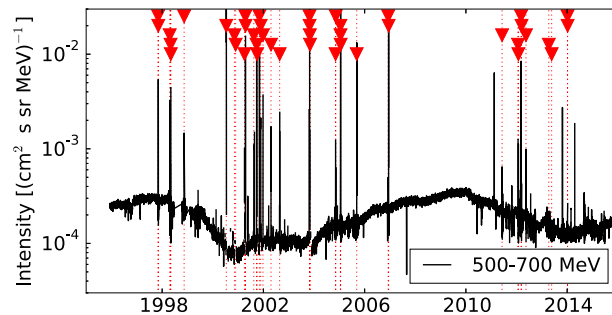
Figure 4 Time profile of the proton intensity in the energy range of 500 to 700 MeV averaged over six hours for the past 20 years. The dashed vertical lines and the arrows indicate the dates of the SEP events found in this study.

background intensity lies between 0.7 and $4 \cdot 10^{-4}$ $(\mathrm{cm}^2\,\mathrm{s}\,\mathrm{sr}\,\mathrm{MeV})^{-1}$ over Solar Cycles 23 and 24. The dates of the events identified in this study are marked as red triangles. We note that some intensity increases shown in the figure were not selected as events since they were caused by photons from the flare (in the range of the extreme-ultraviolet to hard X-rays) depositing energy in the detector stack. Since these photon peaks are typically short lived, they do not increase the intensity over two hours and are therefore not identified by the algorithm. Of the 42 events, 32 events occurred during Solar Cycle 23 and only ten in Solar Cycle 24. As expected, the occurrence of the solar events is clearly more likely during solar maxima (around 2002 and 2014, Nymmik, 1999).

The dates and times when the events passed the threshold are listed in columns two and three of Table 1. We note that these numbers mark the time when the event was identified by the algorithm, and they are not to be confused with onset times. The onset times are derived in Section 4.1. Columns five to eight give the corresponding events from other studies, namely GLEs (taken from http://gle.oulu.fi/), SEPServer (Vainio *et al.*, 2013), GOES (major sep list, http://cdaw.gsfc.nasa.gov/CME_list/sepe/), and Gopalswamy *et al.* (2015), respectively. The exact times of the GLEs were taken from the Neutron Monitor Database (NMDB, http://www.nmdb.eu/nest/gle_list.php). GLE 68 is listed at 00:00 UT by the NMDB, while Cliver (2006) related this GLE to a flare peaking at 09:52 UT. Hence, for this event, the time from Cliver (2006) was adopted.

Events 35, 36, and 41 are listed as sub-GLEs in the Oulu GLE database (https://gle.oulu.fi/), and event 42 was suggested to be a GLE by Thakur *et al.* (2014). However, they are not officially confirmed to be GLEs, and therefore they are not marked as GLEs in our table.

The table clearly shows that the 42 events include all GLEs during the SOHO age (GLE 55 to GLE 72) with the exception of GLE 58, during which SOHO had a data gap. Since GLEs are known to be caused by events during which particles are accelerated to above 500 MeV (Cliver *et al.*, 1983; Plainaki *et al.*, 2009; Shen *et al.*, 2013), this is a validation of the event identification method.

Because the SEPServer list is based on data from 1996 to 2010, it also includes the majority of the events found in this study. The GOES list features every single event found in this study. Gopalswamy *et al.* (2015) have derived a list of 37 large solar events for Solar Cycle 24 that occurred until the end of 2014. Only ten of these events were detected by our method, suggesting that the other 27 events did not accelerate protons to energies above 500 MeV. In their analysis, Gopalswamy *et al.* (2015) identified eight GLE candidates from their list. Of these eight events, only three are found to have increased fluxes above 500 MeV based on this study (events 33, 38, and 40).

Table 1 Event list compiled in this article. The columns represent the event number (column 1), the date (column 2), and the time (column 3) when the intensity threshold was surpassed, the onset time (column 4), corresponding event numbers of the GLE (http://gle.oulu.fi/, Sub-GLE are also marked) (column 5), SEPServer (Vainio *et al.*, 2013) (column 6), GOES (http://cdaw.gsfc.nasa.gov/CME_list/sepe/) (column 7), and Gopalswamy *et al.* (2015) (column 8) event lists. A *p* in the onset time indicates that the time corresponds to the day before the date given in column 1. For details see text.

No.	Date	Time	Onset	GLE No.	SEPS	GOES	Gopalswamy
01	04-11-1997	15:00	06:00	–	2	1	–
02	06-11-1997	13:00	12:45	55	3	2	–
03	20-04-1998	20:00	–	–	6	3	–
04	02-05-1998	18:00	15:00	56	7	4	–
05	06-05-1998	13:00	08:30	57	8	5	–
06	14-11-1998	09:00	06:15	–	12	11	–
07	14-07-2000	12:00	10:30	59	32	21	–
08	09-11-2000	01:00	23:30p	–	38	28	–
09	26-11-2000	18:00	–	–	–	30	–
10	03-04-2001	04:00	01:00	–	45	33	–
11	15-04-2001	16:00	15:00	60	49	36	–
12	18-04-2001	04:00	02:45	61	50	37	–
13	16-08-2001	03:00	00:30	–	–	42	–
14	24-09-2001	23:00	14:00	–	58	44	–
15	01-10-2001	22:00	–	–	59	45	–
16	04-11-2001	17:00	16:30	62	63	48	–
17	23-11-2001	05:00	21:00p	–	64	51	–
18	26-12-2001	07:00	06:30	63	65	52	–
19	21-04-2002	06:00	02:00	–	72	63	–
20	24-08-2002	04:00	02:15	64	80	71	–
21	28-10-2003	13:00	14:00	65	88	78	–
22	29-10-2003	22:00	21:15	66	–	79	–
23	02-11-2003	20:00	17:15	67	90	81	–
24	05-11-2003	06:00	02:00	–	–	82	–
25	07-11-2004	21:00	15:45	–	97	90	–
26	10-11-2004	11:00	03:15	–	99	92	–
27	16-01-2005	14:00	–	–	101	93	–
28	17-01-2005	16:00	13:45	68	–	94	–
29	20-01-2005	09:00	06:45	69	–	95	–
30	08-09-2005	20:00	–	–	–	102	–
31	06-12-2006	23:00	–	–	–	104	–
32	13-12-2006	04:00	03:00	70	112	105	–
33	07-06-2011	09:00	07:15	–	–	110	4
34	23-01-2012	12:00	05:30	–	–	115	9
35	28-01-2012	04:00	18:30p	–	–	116	10
36	07-03-2012	04:00	–	–	–	117	11
37	13-03-2012	19:00	17:45	–	–	118	12
38	17-05-2012	03:00	01:45	71	–	119	13
39	11-04-2013	12:00	07:45	–	–	131	25
40	22-05-2013	20:00	14:00	–	–	133	27
41	06-01-2014	10:00	–	–	–	137	31
42	08-01-2014	00:00	21:00p	–	–	138	32

Figure 5 Proton spectrum with power-law fit for event 2 (GLE 55) from 13:15 to 15:15 UT. Note that only energies below 800 MeV have been used for the fit because of possible electron contamination at higher energies.
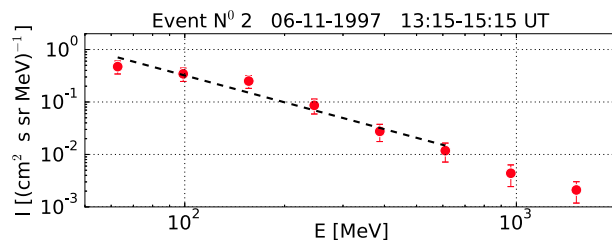

Table 2 Energy bins used for the spectra.

Lower bin edge [MeV]	49	78	124	195	308	486	766	1207
Upper bin edge [MeV]	78	124	195	308	486	766	1207	1903
Geometric mean [MeV]	62	98	155	245	387	610	962	1516

4. Statistical Event Analysis

4.1. Onset Times

For a study of the spectral properties of the events, we took into account only those events for which an onset time based on a 100 to 1000 MeV proton channel could be derived. The chosen broader energy interval in comparison to the 500 to 700 MeV interval allows us to determine the onset with a time resolution of 15 minutes. For 34 of the 42 events, it was possible to derive the onset time by requiring an intensity increase above a threshold defined as the average intensity during the previous six hours plus three times the standard deviation of that time interval. These 34 events include all GLEs and sub-GLEs except for event 41, since EPHIN had a data gap during the early stage of the event (Kühl *et al.*, 2015a). Hence, no onset could be determined for this event, and it is excluded from the following analysis. All determined onset times are listed in column four of Table 1.

4.2. Event Spectra

Since the statistics of EPHIN data for event 25 are limited, it was excluded from the following study, although an onset time was derived. For the remaining 33 events, the high-energy proton spectrum was calculated in a time interval of two hours, starting 30 minutes after the onset. The time lag of 30 minutes is necessary to reflect the different travel times of 100 MeV and 1000 MeV protons. While the latter can reach the spacecraft after about ten minutes (depending on the length of the Parker spiral and the diffusion in the interplanetary medium), the 100 MeV protons can be delayed by up to half an hour because of their lower velocity. The interval length of two hours was selected for statistical reasons. As an example, Figure 5 shows the derived spectrum for event 2 (GLE 55). In the figure, the geometric mean of the energy range is shown. The exact energy bins are given in Table 2.

Mewaldt *et al.* (2012) have shown that the proton spectra of GLE events can be reproduced by a double-power law (described by Band *et al.*, 1993) with a spectral break at several MeV. Since we only analyze energies above 100 MeV, a single power-law function

$$I(E) = I_0 \cdot (E/E_0)^{\gamma}, \tag{1}$$

where the intensities $I(E)$ and I_0 are measured in $[(\text{cm}^2\,\text{s\,sr\,MeV})^{-1}]$ and the energies E, E_0 in [MeV], was fitted for every single event. Based on the approximation of the electron

Table 3 Results of the power law fit to the proton spectra. The columns represent the event number (*cf.* Table 1, column 1), the fitted spectral indices $[\gamma]$ (column 2), and intensities at 500 MeV $[I_{500}]$ (in units of $[(\text{cm}^2\,\text{s}\,\text{sr}\,\text{MeV})^{-1}]$, column 3) of the events. Since the fit was performed as a linear regression between the logarithm of the energy and the logarithm of the intensity, the goodness of the fits is represented by the adjusted coefficient of determination $[R^2]$ (column 4). For details see text.

No.	γ	$[I_{500}]$	R^2	No.	γ	$[I_{500}]$	R^2
01	-2.20 ± 0.16	(8.77 ± 1.00) e–4	0.97	21	-3.15 ± 0.25	(2.07 ± 0.15) e–2	0.97
02	-1.70 ± 0.24	(2.08 ± 0.33) e–2	0.95	22	-2.49 ± 0.11	(3.70 ± 0.15) e–2	1.00
04	-2.12 ± 0.15	(2.31 ± 0.21) e–3	0.96	23	-2.70 ± 0.22	(1.50 ± 0.11) e–2	0.98
05	-2.84 ± 0.26	(1.15 ± 0.12) e–3	0.93	24	-2.67 ± 0.17	(3.45 ± 0.30) e–4	0.98
06	-2.44 ± 0.24	(1.52 ± 0.18) e–3	0.91	26	-1.51 ± 0.11	(9.92 ± 1.94) e–4	0.97
07	-2.24 ± 0.15	(1.74 ± 0.11) e–1	0.97	28	-3.20 ± 0.08	(6.12 ± 0.14) e–3	0.93
08	-2.78 ± 0.31	(1.32 ± 0.14) e–1	0.97	29	-2.12 ± 0.13	(2.53 ± 0.14) e–1	0.99
10	-3.24 ± 0.12	(5.59 ± 0.23) e–4	0.98	32	-1.95 ± 0.15	(3.56 ± 0.26) e–2	0.98
11	-2.13 ± 0.03	(7.77 ± 0.10) e–2	0.99	33	-1.83 ± 0.31	(9.85 ± 3.15) e–4	0.85
12	-2.01 ± 0.12	(3.79 ± 0.31) e–3	0.97	34	-3.78 ± 0.40	(2.45 ± 0.27) e–4	0.78
13	-2.57 ± 0.09	(2.38 ± 0.10) e–3	0.99	35	-2.22 ± 0.24	(1.65 ± 0.25) e–3	0.93
14	-3.30 ± 0.33	(4.39 ± 0.47) e–4	0.93	37	-2.75 ± 0.25	(1.84 ± 0.18) e–3	0.94
16	-2.90 ± 0.20	(1.06 ± 0.07) e–2	0.98	38	-1.87 ± 0.17	(4.47 ± 0.57) e–3	0.97
17	-2.22 ± 0.05	(5.55 ± 0.21) e–4	1.00	39	-2.19 ± 0.09	(3.40 ± 0.26) e–4	0.99
18	-3.21 ± 0.07	(5.39 ± 0.11) e–3	0.99	40	-2.93 ± 0.19	(5.55 ± 0.43) e–4	0.92
19	-3.84 ± 0.10	(2.35 ± 0.06) e–3	0.97	42	-3.60 ± 0.03	(4.93 ± 0.04) e–4	1.00
20	-2.58 ± 0.08	(4.41 ± 0.15) e–3	1.00				

contribution described above (*cf.* Figure 2), only energies below 800 MeV were taken into account for the fit because of possible electron contamination at higher energies. As an example, the fit for event 2 is shown in Figure 5.

Table 3 presents the spectral indices $[\gamma]$ and intensities at 500 MeV $[I_{500}]$ resulting from the fits of the 33 events. The fit was performed as a linear regression between the logarithm of the energy and the logarithm of the intensity. Hence, the goodness of the fits can be represented by the adjusted determination coefficient $[R^2]$, which is also given in Table 3.

4.3. Statistical Analysis of > 500 MeV Proton Events

In Figure 6 the spectral index of the analyzed events is shown as a function of the proton intensity at 500 MeV derived from the proton spectrum fits. GLEs are shown as red squares, the remaining events are plotted as black circles. The numbers in the symbols correspond to those in Tables 1 and 3. The dark gray and light gray shaded areas correspond to the varying GCR background level at 500 MeV during solar maximum and solar minimum, respectively (*cf.* Figure 3). At the top and at the right-hand side of the figure, histograms of both quantities are also shown individually.

The fit results of events 24, 34, and 39 show that the proton intensity at the energy of 500 MeV is slightly lower than the threshold used for the event identification based on the $500 - 700$ MeV channel. This can be explained by statistical errors of the channel intensity and the fit results. However, it should be noted that these events occurred during solar maximum and hence might still have caused an increase above the GCR background.

Figure 6 Bottom left: spectral index [γ] as a function of intensity at 500 MeV derived from the proton spectrum fits. GLEs are marked as red squares, other events as black circles. All numbers correspond to those in Tables 1 and 3. The gray shaded areas (see text) mark the GCR background level in terms of intensity. Top and right: histograms of the intensity at 500 MeV and the spectral index [γ], respectively. The solid red line corresponds to GLEs. Other events are represented by a dashed black line.
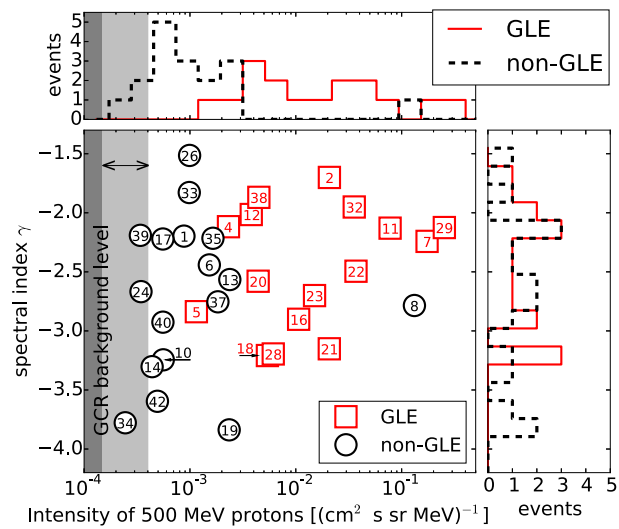
Event 08 shows a much higher intensity than and a similar spectral index as several GLEs, but still shows no increases in the neutron monitor count rates, which is in agreement with findings of Thakur *et al.* (2016). Hence, this event is of special interest in terms of understanding which physical processes determine whether an SEP event with a certain spectral shape is observed by the neutron monitor network. Therefore, an extensive study using not only the spectral data at high energies, but also simulations of the asymptotic viewing directions of neutron monitors is in preparation.

The majority of the GLEs feature spectral indices that are uniformly distributed between -2 and -3, which is in good agreement with the results of Mewaldt *et al.* (2012). The spectral indices of events not related to GLEs are also uniformly distributed, but in a wider range between -2 and -4. The spectral index of event 20 ($\gamma = -2.58$) is identical with the findings of Tylka *et al.* (2006).

However, the intensity of 500 MeV protons is typically higher during GLE-related events than during events without GLEs. Furthermore, this intensity is above $2 \cdot 10^{-3}$ $(\mathrm{cm^2\,s\,sr\,MeV})^{-1}$ for all GLEs (except for event 5), which is consistent with the results of Nitta *et al.* (2012). In their study, these authors showed that the GOES/HEPAD P9 channel ($420-510$ MeV) typically exceeds $2 \cdot 10^{-3}$ $(\mathrm{cm^2\,s\,sr\,MeV})^{-1}$ during GLEs with only GLE 57 and GLE 68, corresponding to events 05 and 28 in our list, having lower fluxes. Thakur *et al.* (2016) also found GLE 57 to be an especially small event. While the results of this work do confirm the results of previous studies regarding the low intensity of GLE 57, the intensity of GLE 68 is found to be higher than the results of Nitta *et al.* (2012). However, in their study, Nitta *et al.* (2012) noted that the onset determination and hence the analysis of this particular event is troublesome.

The five GLEs with the highest flux in our analysis (events 29, 07, 11, 22, and 32, corresponding to GLEs 69, 59, 60, 66, and 70) are also considered to be among the largest GLEs in the SOHO era (*cf.* Table 1 in McCracken, Moraal, and Shea, 2012). The relative increases in neutron monitor count rate for GLEs given by McCracken, Moraal, and Shea (2012) are shown as a function of the intensity at 500 MeV derived in this study in Figure 7. Some GLEs from Table 1 are not shown here, as they have not been investigated by Mc-Cracken, Moraal, and Shea (2012). The figure indicates a correlation between the intensity at 500 MeV and the relative increase in NM count rate, with the exception of events whose intensities are below 10^{-2} $(\mathrm{cm^2\,s\,sr\,MeV})^{-1}$ (events 12, 18, and 38) and event 29, which has a significantly higher increase in NM count rate than the measured intensity at 500 MeV.

Figure 7 Relative increase of the neutron monitor count rate as a function of intensity at 500 MeV based on the fit. The increase in the NM count rates is taken from McCracken, Moraal, and Shea (2012). The numbers correspond to Tables 1 and 3.
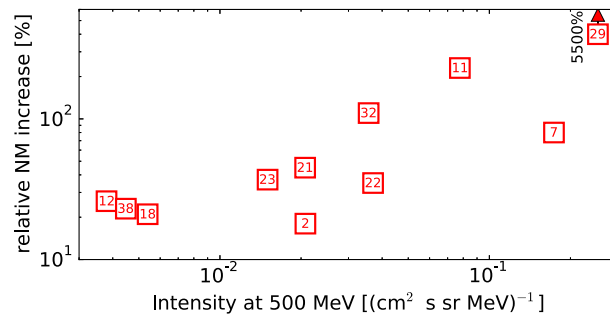
Furthermore, it has to be noted that the scattering of the relative NM count rate increase for a given intensity at 500 MeV is rather high. The reasons for these deviations remain unclear, especially since the spectral shape of the events (*e.g.* the fitted γ) are rather similar for most of them (*cf.* Figure 6). Possible explanations are the asymptotic viewing direction of each neutron monitor (McCracken and Freon, 1962; Smart, Shea, and Flückiger, 2000) or changes in the cutoff rigidities that are due to geomagnetic disturbances during the SEP events (Danilova, 1999), which may differ from event to event.

5. Summary

We investigate SEP events with protons with energies above 500 MeV based on the extended measurement range of SOHO/EPHIN described by Kühl *et al.* (2015a) and Kühl, Gómez-Herrero, and Heber (2016).

We show that the new and unique data product is valid during any stage of the solar event (*e.g.* onset, maximum, and decay phase) by comparison with results from IMP8 and GOES. Furthermore, additional simulations of the instrument show that the electron contribution to the high-energy proton data is: 1) negligible below 500 MeV, 2) lower than 20 % between 500 and 800 MeV, and 3) seriously uncertain above 800 MeV.

Based on the energy interval from 500 to 700 MeV, 42 SEP events with protons accelerated to above 500 MeV have been identified during the last 20 years of the SOHO mission. The compiled event list (see Table 1) was compared to various other event lists, including the GLE list.

For events with clear onset times, the proton intensity spectra were derived in a time interval of two hours, starting 30 minutes after the onset time. The spectral indices [γ] derived from the power-law fit in the energy range below 800 MeV and the intensity at 500 MeV of the events were compared (see Figure 6 and Table 3).

Based on this comparison, various results from the literature such as typical intensity increases above $2 \cdot 10^{-3}$ $(cm^2\,s\,sr\,MeV)^{-1}$ at 500 MeV (Nitta *et al.*, 2012) were validated. Furthermore, certain non-GLE and GLE events with surprisingly high and low intensity, respectively, were found, in agreement with Thakur *et al.* (2016).

Comparing the derived intensities at 500 MeV with the relative increase of the neutron monitor count rates during GLEs (McCracken, Moraal, and Shea, 2012), a clear correlation was found, with the exception of events with a very low intensity at 500 MeV and GLE 69, which shows a particularly strong increase in the neutron monitor count rate.

This work was carried out within the framework of the bilateral BMBF-NRF-project 'Astrohel' (01DG15009) funded by the Bundesministerium für Bildung und Forschung. The responsibility of the contents of this work is with the authors.

Disclosure of Potential Conflicts of Interest   The authors declare that they have no conflicts of interest.

References

Band, D., Matteson, J., Ford, L., Schaefer, B., Palmer, D., Teegarden, B., Cline, T., Briggs, M., Paciesas, W., Pendleton, G., Fishman, G., Kouveliotou, C., Meegan, C., Wilson, R., Lestrade, P.: 1993, BATSE observations of gamma-ray burst spectra. I – Spectral diversity. *Astrophys. J.* **413**, 281. DOI.

Cane, H.V.: 2000, Coronal mass ejections and Forbush decreases. *Space Sci. Rev.* **93**, 55. DOI.

Cliver, E.W.: 2006, The unusual relativistic solar proton events of 1979 August 21 and 1981 May 10. *Astrophys. J.* **639**, 1206. DOI.

Cliver, E.W., Kahler, S.W., Cane, H.V., Koomen, M.J., Michels, D.J., Howard, R.A., Sheeley, N.R. Jr.: 1983, The GLE-associated flare of 21 August, 1979. *Solar Phys.* **89**, 181. DOI. ADS.

Danilova, O.: 1999, The GLE of May 2, 1998: An effect of disturbed magnetosphere on solar cosmic rays. In: *Int. Cosmic Ray Conf.* **6**, 399. ADS.

Forbush, S.E.: 1946, Three unusual cosmic-ray increases possibly due to charged particles from the Sun. *Phys. Rev.* **70**, 771. DOI.

GEANT4 collaboration: 2006, An object-oriented toolkit for simulation in hep. CERN-LHCC 98-44. See also http://geant4.cern.ch/.

Gopalswamy, N., Mäkelä, P.: 2014, Latitudinal connectivity of ground level enhancement events. In: Hu, Q., Zank, G.P. (eds.) *Outstanding Problems in Heliophysics: From Coronal Heating to the Edge of the Heliosphere*, Astron. Soc. Pacific Conf. Ser. **484**, 63. ADS.

Gopalswamy, N., Mäkelä, P., Yashiro, S., Xie, H., Akiyama, S., Thakur, N.: 2015, High-energy solar particle events in cycle 24. *J. Phys. Conf. Ser.* **642**(1), 012012. DOI.

Hanser, F.A.: 2011, EPS/HEPAD calibration and data handbook. Tech. rep. goesn-eng-048d. Available at www.ngdc.noaa.gov/stp/satellite/goes/documentation.html. DOI.

Heber, B., Fichtner, H., Scherer, K.: 2006, Solar and heliospheric modulation of galactic cosmic rays. *Space Sci. Rev.* **125**, 81. DOI. ADS.

Heber, B., Potgieter, M.S.: 2006, Cosmic rays at high heliolatitudes. *Space Sci. Rev.* **127**, 117. DOI. ADS.

Heber, B., Dresing, N., Herbst, K., Klassen, A., Kühl, P., Gómez-Herrero, R.: 2015, Proton energy spectra during ground level enhancements as measured by EPHIN aboard SOHO. In: *Proc. Science ICRC 2015*.

Kühl, P., Gómez-Herrero, R., Heber, B.: 2016, Annual cosmic ray spectra from 250 MeV up to 1.6 GeV from 1995 – 2014 measured with the electron proton helium instrument onboard SOHO. *Solar Phys.* **291**, 965. DOI.

Kühl, P., Banjac, S., Dresing, N., Gómez-Herrero, R., Heber, B., Klassen, A., *et al.*: 2015a, Proton intensity spectra during the solar energetic particle events of May 17, 2012 and January 6, 2014. *Astron. Astrophys.* **576**, A120. DOI. ADS.

Kühl, P., Dresing, N., Gieseler, J., Heber, B., Klassen, A.: 2015b, Galactic cosmic ray spectra during solar cycle 23 and 24 – Measurement capabilities of the electron proton helium instrument. In: *Proc. Science ICRC 2015*.

Lockwood, J.A., Debrunner, H.: 1999, Solar flare particle measurements with neutron monitors. *Space Sci. Rev.* **88**, 483. DOI. ADS.

McCracken, K.G., Freon, A.: 1962, Asymptotic directions and cut-off rigidities in the geomagnetic field. *J. Phys. Soc. Japan* **17**, AII, 455. ADS.

McCracken, K.G., Moraal, H., Shea, M.A.: 2012, The high-energy impulsive ground-level enhancement. *Astrophys. J.* **761**, 101. DOI.

McGuire, R.E., von Rosenvinge, T.T. McDonald, F.B.: 1986, The composition of solar energetic particles. *Astrophys. J.* **301**, 938. DOI.

Mewaldt, R.A., Looper, M.D., Cohen, C.M.S., Haggerty, D.K., Labrador, A.W., Leske, R.A., Mason, G.M., Mazur, J.E., von Rosenvinge, T.T.: 2012, Energy spectra, composition, and other properties of ground-level events during solar cycle 23. *Space Sci. Rev.* **171**, 97. DOI.

Mishev, A.L., Usoskin, I.G., Kovaltsov, G.A.: 2013, Neutron monitor yield function: New improved computations. *J. Geophys. Res.* **118**, 2783. DOI. ADS.

Müller-Mellin, R., Kunow, H., Fleißner, V., Pehlke, E., Rode, E., Röschmann, N., *et al.*: 1995, Costep – Comprehensive suprathermal and energetic particle analyser. *Solar Phys.* **162**, 483.

Nitta, N.V., Liu, Y., DeRosa, M.L., Nightingale, R.W.: 2012, What are special about ground-level events? Flares, CMEs, active regions and magnetic field connection. *Space Sci. Rev.* **171**, 61. DOI. ADS.

Nymmik, R.: 1999, Relationships among solar activity SEP occurrence frequency, and solar energetic particle event distribution function. In: *Int. Cosmic Ray Conf.*, **6**, 280. ADS.

Onsager, T., Grubb, R., Kunches, J., Matheson, L., Speich, D., Zwickl, R.W., Sauer, H.: 1996, Operational uses of the GOES energetic particle detectors. In: Washwell, E.R. (ed.) *GOES-8 and Beyond*, *Proc. SPIE* **2812**, 281. DOI.

Plainaki, C., Mavromichalaki, H., Belov, A., Eroshenko, E., Yanke, V.: 2009, Modeling the solar cosmic ray event of 13 December 2006 using ground level neutron monitor data. *Adv. Space Res.* **43**, 474. DOI. ADS.

Reames, D.V.: 2013, The two sources of solar energetic particles. *Space Sci. Rev.* **175**, 53. DOI. ADS.

Sandberg, I., Jiggens, P., Heynderickx, D., Daglis, I.A.: 2014, Cross calibration of NOAA GOES solar proton detectors using corrected NASA IMP-8/GME data. *Geophys. Res. Lett.* **41**, 4435. DOI. ADS.

Shen, C., Li, G., Kong, X., Hu, J., Sun, X.D., Ding, L., Chen, Y., Wang, Y., Xia, L.: 2013, Compound twin coronal mass ejections in the 2012 May 17 GLE event. *Astrophys. J.* **763**, 114. DOI. ADS.

Smart, D.F., Shea, M.A., Flückiger, E.O.: 2000, Magnetospheric models and trajectory computations. *Space Sci. Rev.* **93**, 305. DOI. ADS.

Thakur, N., Gopalswamy, N., Xie, H., Mäkelä, P., Yashiro, S., Akiyama, S., Davila, J.M.: 2014, Ground level enhancement in the 2014 January 6 solar energetic particle event. *Astrophys. J. Lett.* **790**, L13. DOI. ADS.

Thakur, N., Gopalswamy, N., Mäkelä, P., Akiyama, S., Yashiro, S., Xie, H.: 2016, Two exceptions in the large SEP events of solar cycles 23 and 24. *Solar Phys.* **291**, 513. DOI.

Tylka, A.J., Cohen, C.M.S., Dietrich, W.F., Lee, M.A., Maclennan, C.G., Mewaldt, R.A., Ng, C.K., Reames, D.V.: 2006, A comparative study of ion characteristics in the large gradual solar energetic particle events of 2002 April 21 and 2002 August 24. *Astrophys. J. Suppl.* **164**, 536. DOI. ADS.

Vainio, R., Valtonen, E., Heber, B., Malandraki, O.E., Papaioannou, A., Klein, K.-L., Afanasiev, A., Agueda, N., Aurass, H., Battarbee, M., Braune, S., Dröge, W., Ganse, U., Hamadache, C., Heynderickx, D., Huttunen-Heikinmaa, K., Kiener, J., Kilian, P., Kopp, A., Kouloumvakos, A., Maisala, S., Mishev, A., Miteva, R., Nindos, A., Oittinen, T., Raukunen, O., Riihonen, E., Rodríguez-Gasén, R., Saloniemi, O., Sanahuja, B., Scherer, R., Spanier, F., Tatischeff, V., Tziotziou, K., Usoskin, I.G., Vilmer, N.: 2013, The first SEPServer event catalogue ∼68-MeV solar proton events observed at 1 AU in 1996 – 2010. *J. Space Weather Space Clim.* **3**(27), A12. DOI.

SUMMARY & OUTLOOK

Measurements of the energy spectra of interplanetary particles are crucial in order to understand the physical processes related to the acceleration of these particles as well as their propagation in the heliosphere. This applies in particular to the energy range from 100 MeV up to above 1 GeV since both the solar modulation of Galactic Cosmic Rayss (GCRs) and the larger Solar Energetic Particle (SEP) events can be observed in this energy regime. Unfortunatelly, instruments capable of providing these measurements are rare. Although principally capable of performing these measurements, the AMS and PAMELA instruments can only supply this data at energies above several hundred MeV and with limited time coverage due to magnetospheric effects. Furthermore, data from both missions is only available for six and eleven years, respectively, and hence, studies of drift effects and their role in the solar modulation as well as statistical analyzes based on a large number of SEP events are not possible with these instruments.

In order to overcome these limitations and to bridge the energy gap between AMS and PAMELA on the one side and the various instruments with measurements below 100 MeV on the other side, an extension of the energy range of Electron Proton Helium Instrument (EPHIN) aboard the Solar and Heliospheric Observatory (SOHO) has been achieved in this thesis. For this purpose a GEANT4 simulation of the instrument was set up in order to analyze the response of the instrument to electrons, protons and helium particles that penetrate the entire instrument. Based on these results, a method to identify particle types and their initial total kinetic energy based on measured energy losses in the detector has been developed.

In a first study the method has been applied to the May 17th, 2012 and January 6th, 2014 SEP events [Kühl et al., 2015a]. It has been shown that the proton spectrum for the former event is in agreement to previous results from PAMELA in the energy range from 100 to 800 MeV. Furthermore, a combination of the new method with the nominal data products of the instrument has been presented, allowing EPHIN to measure the continuous proton spectrum from 5 MeV up to above 800 MeV during SEP events.

Furthermore, the possibility of deriving the GCR proton spectra has been explored [Kühl et al., 2015c, 2016]. Both, simulations with expected GCR spectra based on the Force-Field Solution (FFS) as well as comparisons with various different missions (AMS, BESS and PAMELA) have shown that the new method enables EPHIN to measure the GCR protons spectrum in an energy range from 250 MeV to 1.6 GeV with a systematic uncertainty of less than 20%. The annual spectra between 1995 and 2014 have been published for protons and analysed with special emphasis on drift effects. It has been also shown that the method can be extended to Helium, while modulation of other heavy ions (i.e. Boron, Carbon, Nitrogen, Oxygen and Neon) can only be studied qualitatively.

The continuous data from EPHIN has been also used to identifiy SEP events with an increase in the proton intensity above 500 MeV between 1995 and 2015 [Kühl et al., 2017]. Therefore, the high energy data has been further validated by comparison with measurements from GOES and IMP8 during different phases of a SEP event (e.g. during the onset and in the declining phase). The electron contamination has been analysed and estimated to be negligible below 500 MeV and lower than 20% between 500 and 800 MeV. In total, 42 events with an increase in the proton intensity above 500 MeV have been identified. The onset times for the events have been derived and a statistical analysis based on the spectral properties of the events has been performed, showing that GLEs have similar spectral slopes compared to other events but a higher intensity at 500 MeV. In addition, a correlation between the calculated intensities and the increases in the NM count rates for those events related to GLEs has been found.

In future studies, the presented method can be applied to Helium particles from 100 MeV to above 1 GeV measured by EPHIN whose energy losses can be clearly distinguished from those of heavier ions. The analysis of the latter, however, is restricted due to the limited statistics and a significant overlap of the energy losses caused by different ions. An extension of the EPHIN energy range of electrons is not possible since there is no clear dependence between the energy loss and the total energy of electrons between 10 and 100 MeV [Kühl et al., 2015a].

Furthermore, the method can be easily applied to other instruments that measure the energy loss in one or two detectors in a coincidence condition that surpresses low energy (<10 MeV) electrons. Hence, previous and current instruments such as STEREO/HET [von Rosenvinge et al., 2008] as well as future instruments like SOLAR ORBITER/HET [Gómez-Herrero et al., 2017] can adopt the method in order to extend their measurement capabilities.

K. Abe, H. Fuke, S. Haino, et al. Measurements of cosmic-ray proton and helium spectra from the BESS-Polar long-duration balloon flights over Antarctica. *ArXiv 1506.01267 e-prints*, June 2015.

O. Adriani, G. C. Barbarino, G. A. Bazilevskaya, et al. PAMELA Measurements of Cosmic-Ray Proton and Helium Spectra. *Science*, 332:69, April 2011. doi: 10.1126/science.1199172.

O. Adriani, G. C. Barbarino, G. A. Bazilevskaya, et al. Time Dependence of the Proton Flux Measured by PAMELA during the 2006 July-2009 December Solar Minimum. *Astrophys. J.*, 765:91, March 2013. doi: 10.1088/0004-637X/765/2/91.

S. Agostinelli, J. Allison, K. Amako, et al. GEANT4 - a simulation toolkit. *Nuclear Instruments and Methods in Physics Research A*, 506:250–303, July 2003. doi: 10.1016/S0168-9002(03)01368-8.

M. Aguilar, D. Aisa, B. Alpat, et al. Precision Measurement of the Helium Flux in Primary Cosmic Rays of Rigidities 1.9 GV to 3 TV with the Alpha Magnetic Spectrometer on the International Space Station. *Physical Review Letters*, 115 (21):211101, November 2015. doi: 10.1103/PhysRevLett.115.211101.

M. Aguilar, D. Aisa, B. Alpat, et al. Precision measurement of the proton flux in primary cosmic rays from rigidity 1 gv to 1.8 tv with the alpha magnetic spectrometer on the international space station. *Phys. Rev. Lett.*, 114:171103, Apr 2015. doi: 10.1103/PhysRevLett.114.171103. URL link.aps.org/doi/10.1103/PhysRevLett.114.171103.

J. Alcaraz, B. Alpat, G. Ambrosi, et al. Cosmic protons. *Physics Letters B*, 490: 27–35, September 2000. doi: 10.1016/S0370-2693(00)00970-9.

K. Asakimori, T. H. Burnett, M. L. Cherry, et al. Cosmic-Ray Proton and Helium Spectra: Results from the JACEE Experiment. *Astrophys. J.*, 502:278–283, July 1998. doi: 10.1086/305882.

M. J. Aschwanden. GeV Particle Acceleration in Solar Flares and Ground Level Enhancement (GLE) Events. *Space Sci. Rev.*, 171:3–21, October 2012. doi: 10.1007/s11214-011-9865-x.

S. Banjac, R. Gómez-Herrero, B. Heber, P. Kühl, and C. Terasa. EPHIN anisotropy measurement capability. *Journal of Physics Conference Series*, 632(1):012048, August 2015. doi: 10.1088/1742-6596/632/1/012048.

G. A. Bazilevskaya, A. G. Mayorov, and V. V. Mikhailov. Comparison of solar energetic particle events observed by PAMELA experiment and by other instruments in 2006-2012. *33nd ICRC Proceedings*, 2013.

H. Bethe. Zur theorie des durchgangs schneller korpuskularstrahlen durch materie. *Annalen der Physik*, 397(3):325–400, 1930. ISSN 1521-3889. doi: 10.1002/andp.19303970303. URL http://dx.doi.org/10.1002/andp.19303970303.

V. Bindi. Solar Energetic Particles measured by AMS-02. *Proceedings of Science*, ICRC2015, 2015.

P. Blasi. The origin of galactic cosmic rays. *Astron. Astrophys. Rev.*, 21:70, November 2013. doi: 10.1007/s00159-013-0070-7.

F. Bloch. Zur Bremsung rasch bewegter Teilchen beim Durchgang durch Materie. *Annalen der Physik*, 408:285–320, 1933. doi: 10.1002/andp.19334080303.

N. Bohr. Ii. on the theory of the decrease of velocity of moving electrified particles on passing through matter. *Philosophical Magazine Series 6*, 25(145):10–31, 1913. doi: 10.1080/14786440108634305. URL http://dx.doi.org/10.1080/14786440108634305.

N. Bohr. Lx. on the decrease of velocity of swiftly moving electrified particles in passing through matter. *Philosophical Magazine Series 6*, 30(178):581–612, 1915. doi: 10.1080/14786441008635432. URL http://dx.doi.org/10.1080/14786441008635432.

G. E. Brueckner, R. A. Howard, M. J. Koomen, et al. The Large Angle Spectroscopic Coronagraph (LASCO). *Solar Phys.*, 162:357–402, December 1995. doi: 10.1007/BF00733434.

R. A. Burger, M. S. Potgieter, and B. Heber. Rigidity dependence of cosmic ray proton latitudinal gradients measured by the Ulysses spacecraft: Implications for the diffusion tensor. *J. Geophys. Res.*, 105:27447–27456, December 2000. doi: 10.1029/2000JA000153.

R. A. Caballero-Lopez and H. Moraal. Limitations of the force field equation to describe cosmic ray modulation. *Journal of Geophysical Research (Space Physics)*, 109:A01101, January 2004. doi: 10.1029/2003JA010098.

H. V. Cane and I. G. Richardson. Interplanetary coronal mass ejections in the near-Earth solar wind during 1996-2002. *Journal of Geophysical Research (Space Physics)*, 108:1156, April 2003. doi: 10.1029/2002JA009817.

R. Carbone, N. Thakur, M. Martucci, et al. PAMELA Observation of the 2012 May 17 GLE Event. *Proceedings of 33th International Cosmic Ray Conference (ICRC 2013)*, 2:1351–1354, 2013.

E. W. Cliver. A Revised Classification Scheme for Solar Energetic Particle Events. *Central European Astrophysical Bulletin*, 33:253–270, 2009.

E. W. Cliver. Flare vs. Shock Acceleration of High-energy Protons in Solar Energetic Particle Events. *Astrophys. J.*, 832:128, December 2016. doi: 10.3847/0004-637X/832/2/128.

C. Corti, V. Bindi, C. Consolandi, and K. Whitman. Solar Modulation of the Local Interstellar Spectrum with Voyager 1, AMS-02, PAMELA, and BESS. *Astrophys. J.*, 829:8, September 2016. doi: 10.3847/0004-637X/829/1/8.

W. Curdt and B. Fleck. Solar and Galactic Cosmic Rays Observed by SOHO. *Central European Astrophysical Bulletin*, 39:109–118, 2015.

A. J. Davis, R. A. Mewaldt, C. M. S. Cohen, et al. Solar minimum spectra of galactic cosmic rays and their implications for models of the near-earth radiation environment. *J. Geophys. Res.*, 106:29979–29988, December 2001. doi: 10.1029/2000JA000325.

J.-P. Delaboudinière, G. E. Artzner, J. Brunaud, et al. EIT: Extreme-Ultraviolet Imaging Telescope for the SOHO Mission. *Solar Phys.*, 162:291–312, December 1995. doi: 10.1007/BF00733432.

M. Desai and J. Giacalone. Large gradual solar energetic particle events. *Living Reviews in Solar Physics*, 13:3, December 2016. doi: 10.1007/s41116-016-0002-5.

V. Domingo, B. Fleck, and A. I. Poland. The SOHO Mission: an Overview. *Solar Phys.*, 162:1–37, December 1995. doi: 10.1007/BF00733425.

J. F. Drake, M. Opher, M. Swisdak, and J. N. Chamoun. A Magnetic Reconnection Mechanism for the Generation of Anomalous Cosmic Rays. *Astrophys. J.*, 709: 963–974, February 2010. doi: 10.1088/0004-637X/709/2/963.

U. Fano. Penetration of Protons, Alpha Particles, and Mesons. *Annual Review of Nuclear and Particle Science*, 13:1–66, 1963. doi: 10.1146/annurev.ns.13.120163.000245.

L. A. Fisk and M. A. Lee. Shock acceleration of energetic particles in corotating interaction regions in the solar wind. *Astrophys. J.*, 237:620–626, April 1980. doi: 10.1086/157907.

S. E. Forbush. Three Unusual Cosmic-Ray Increases Possibly Due to Charged Particles from the Sun. *Physical Review*, 70:771–772, November 1946. doi: 10.1103/PhysRev.70.771.

GEANT4 collaboration. An object-oriented toolkit for simulation in hep. *CERN-LHCC 98-44*, page see also: http://geant4.cern.ch/, 2006.

J. S. George, K. A. Lave, M. E. Wiedenbeck, et al. Elemental Composition and Energy Spectra of Galactic Cosmic Rays During Solar Cycle 23. *Astrophys. J.*, 698:1666–1681, June 2009. doi: 10.1088/0004-637X/698/2/1666.

J. Giacalone and M. Neugebauer. The Energy Spectrum of Energetic Particles Downstream of Turbulent Collisionless Shocks. *Astrophys. J.*, 673:629-636, January 2008. doi: 10.1086/524008.

L. J. Gleeson and W. I. Axford. Cosmic Rays in the Interplanetary Medium. *Astrophys. J. Lett.*, 149:L115, September 1967. doi: 10.1086/180070.

L. J. Gleeson and W. I. Axford. The Compton-Getting Effect. *Astrophys. Space Sci.*, 2:431–437, December 1968a. doi: 10.1007/BF02175919.

L. J. Gleeson and W. I. Axford. Solar Modulation of Galactic Cosmic Rays. *Astrophys. J.*, 154:1011, December 1968b. doi: 10.1086/149822.

L. J. Gleeson and I. H. Urch. A Study of the Force-Field Equation for the Propagation of Galactic Cosmic Rays. *Astrophys. Space Sci.*, 25:387–404, December 1973. doi: 10.1007/BF00649180.

R. Gómez-Herrero. *Partículas energéticas en la heliosfera interna (1996-2000). Respuesta instrumental y observaciones del sensor EPHIN embarcado en el Observatorio Solar y Heliosferico SOHO (ESA-NASA).* PhD thesis, University of Alcalá, 2 2003.

R. Gómez-Herrero, J. Rodríguez-Pacheco, R. F. Wimmer-Schweingruber, et al. The Solar Orbiter Mission: an Energetic Particle Perspective. *ArXiv e-prints*, January 2017.

N. Gopalswamy, P. Mäkelä, S. Yashiro, et al. High-energy solar particle events in cycle 24. *Journal of Physics Conference Series*, 642(1):012012, September 2015. doi: 10.1088/1742-6596/642/1/012012.

B. Heber and M. S. Potgieter. Cosmic Rays at High Heliolatitudes. *Space Sci. Rev.*, 127:117–194, December 2006. doi: 10.1007/s11214-006-9085-y.

B. Heber, H. Fichtner, and K. Scherer. Solar and Heliospheric Modulation of Galactic Cosmic Rays. *Space Sci. Rev.*, 125:81–93, August 2006. doi: 10.1007/s11214-006-9048-3.

B. Heber, M. S. Potgieter, S. E. S. Ferreira, et al. An overview of Jovian electrons during the distant Ulysses Jupiter flyby. *Planetary Space Science*, 55:1–11, January 2007. doi: 10.1016/j.pss.2006.06.018.

B. Heber, C. Wallmann, D. Galsdorf, et al. Forbush decreases associated to Stealth Coronal Mass Ejections. *Central European Astrophysical Bulletin*, 39:75–82, 2015.

K. Herbst, A. Kopp, B. Heber, et al. On the importance of the local interstellar spectrum for the solar modulation parameter. *Journal of Geophysical Research (Space Physics)*, 115:D00I20, July 2010. doi: 10.1029/2009JD012557.

K. Herbst, R. Muscheler, and B. Heber. The new local interstellar spectra and their influence on the production rates of the cosmogenic radionuclides ^{10}Be and ^{14}C. *Journal of Geophysical Research (Space Physics)*, 122:23–34, January 2017. doi: 10.1002/2016JA023207.

V. F. Hess. Über Beobachtungen der durchdringenden Strahlung bei sieben Freiballonfahrten. *Phys. Z.*, 13:1094–1091, November 1912.

J. R. Jokipii and D. A. Kopriva. Effects of particle drift on the transport of cosmic rays. III - Numerical models of galactic cosmic-ray modulation. *Astrophys. J.*, 234:384–392, November 1979. doi: 10.1086/157506.

M.-B. Kallenrode. Current views on impulsive and gradual solar energetic particle events. *Journal of Physics G Nuclear Physics*, 29:965–981, May 2003.

A. Kopp, T. Wiengarten, H. Fichtner, et al. Cosmic-Ray Transport in Heliospheric Magnetic Structures. II. Modeling Particle Transport through Corotating Interaction Regions. *Astrophys. J.*, 837:37, March 2017. doi: 10.3847/1538-4357/aa603b.

A. Kountine. The alpha magnetic spectrometer on the international space station. *International Journal of Modern Physics E*, 21(08):1230005, 2012. doi: 10.1142/S0218301312300056. URL http://www.worldscientific.com/doi/abs/10.1142/S0218301312300056.

M. B. Krainev and M. S. Kalinin. On the GCR intensity and the inversion of the heliospheric magnetic field during the periods of the high solar activity. *ArXiv e-prints*, November 2014.

P. Kühl, N. Dresing, P. Dunzlaff, et al. Spectrum of galactic and Jovian electrons. *Proceedings of 33th International Cosmic Ray Conference (ICRC 2013)*, 5:3480–3483, 2013a.

P. Kühl, N. Dresing, P. Dunzlaff, et al. Simultaneous Analysis of Recurrent Jovian Electron Increases and Galactic Cosmic Ray Decreases. *Central European Astrophysical Bulletin*, 37:643–648, 2013b.

P. Kühl, S. Banjac, N. Dresing, et al. Proton intensity spectra during the solar energetic particle events of May 17, 2012 and January 6, 2014. *Astron. Astrophys.*, 576:A120, April 2015a. doi: 10.1051/0004-6361/201424874.

P. Kühl, S. Banjac, B. Heber, et al. Extended Measurement Capabilities of the Electron Proton Helium INstrument aboard SOHO - Understanding single detector count rates. *Central European Astrophysical Bulletin*, 39:119–124, 2015b.

P. Kühl, N. Dresing, J. Gieseler, B. Heber, and A. Klassen. Galactic cosmic ray quiet time spectra from 300 MeV up to above 1 GeV measured with SOHO/EPHIN. *Proceedings of Science - International Cosmic Ray Conference*, 2015c.

P. Kühl, R. Gómez-Herrero, and B. Heber. Annual Cosmic Ray Spectra from 250 MeV up to 1.6 GeV from 1995 - 2014 Measured with the Electron Proton Helium Instrument onboard SOHO. *Solar Phys.*, 291:965–974, March 2016. doi: 10.1007/s11207-016-0879-0.

P. Kühl, N. Dresing, B. Heber, and A. Klassen. Solar Energetic Particle Events with Protons Above 500 MeV Between 1995 and 2015 Measured with SOHO/EPHIN. *Solar Phys.*, 292:10, January 2017. doi: 10.1007/s11207-016-1033-8.

H. Kunow, G. Wibberenz, G. Green, R. Müller-Mellin, and M.-B. Kallenrode. *Energetic Particles in the Inner Solar System*, page 152. Springer-Verlag Berlin Heidelberg, 1991.

L. Landau. On the energy loss of fast particles by ionization. *J. Phys.(USSR)*, 8:201–205, 1944.

D. Lario. Advances in modeling gradual solar energetic particle events. *Advances in Space Research*, 36:2279–2288, 2005. doi: 10.1016/j.asr.2005.07.081.

J. A. Le Roux and M. S. Potgieter. The simulation of complete 11 and 12 year modulation cycles for cosmic rays in the heliosphere using a drift model with global merged interaction regions. *Astrophys. J.*, 442:847–851, April 1995. doi: 10.1086/175487.

C. Li, K. A. Firoz, L. P. Sun, and L. I. Miroshnichenko. Electron and Proton Acceleration during the First Ground Level Enhancement Event of Solar Cycle 24. *Astrophys. J.*, 770:34, June 2013. doi: 10.1088/0004-637X/770/1/34.

B. Lifter, K. Scissors, and H. Sprucener. On the Influence of the Solar Bi-Cycle on Comic Ray Modulatio. In *34th COSPAR Scientific Assembly*, volume 34 of *COSPAR Meeting*, 2002.

J. A. Lockwood and H. Debrunner. Solar flare particle measurements with neutron monitors. *Space Sci. Rev.*, 88:483–500, April 1999. doi: 10.1023/A: 1005159816103.

M.S. Longair. *High Energy Astrophysics: Volume 1, Particles, Photons and their Detection*. Cambridge University Press, 1992. ISBN 9780521383745. URL https://books.google.de/books?id=CJwRAQAAIAAJ.

R. Manuel, S. E. S. Ferreira, M. S. Potgieter, R. D. Strauss, and N. E. Engelbrecht. Time-dependent cosmic ray modulation. *Advances in Space Research*, 47:1529–1537, May 2011. doi: 10.1016/j.asr.2010.12.007.

J. Marquardt, B. Heber, M. Hörlöck, P. Kühl, and R. F. Wimmer-Schweingruber. GEANT 4 simulation of the Helios cosmic ray telescope E6: Feasibility of chemical composition studies. In *Journal of Physics Conference Series*, volume 632 of *Journal of Physics Conference Series*, page 012016, August 2015a. doi: 10.1088/1742-6596/632/1/012016.

J. Marquardt, B. Heber, P. Kühl, and R. Wimmer. The chemical composition of galactic cosmic rays during solar minimum of solar cycle 20/21 - Helios E6 results. In *34th International Cosmic Ray Conference (ICRC2015)*, volume 34 of *International Cosmic Ray Conference*, page 123, July 2015b.

D. Matthiä, K. Herbst, B. Heber, T. Berger, and G. Reitz. ^{10}Be Production in the Atmosphere by Galactic Cosmic Rays. *Space Sci. Rev.*, 176:333–342, June 2013. doi: 10.1007/s11214-011-9817-5.

C. J. Mertens, M. M. Meier, S. Brown, R. B. Norman, and X. Xu. NAIRAS aircraft radiation model development, dose climatology, and initial validation. *Space Weather*, 11:603–635, October 2013. doi: 10.1002/swe.20100.

R. A. Mewaldt, J. D. Spalding, E. C. Stone, and R. E. Vogt. The isotropic composition of cosmic ray B, C, N, and O nuclei. *Astrophys. J. Lett.*, 251:L27–L31, December 1981. doi: 10.1086/183686.

A. L. Mishev, L. G. Kocharov, and I. G. Usoskin. Analysis of the ground level enhancement on 17 May 2012 using data from the global neutron monitor network. *Journal of Geophysical Research (Space Physics)*, 119:670–679, February 2014. doi: 10.1002/2013JA019253.

H. Moraal. Cosmic-Ray Modulation Equations. *Space Sci. Rev.*, 176:299–319, June 2013. doi: 10.1007/s11214-011-9819-3.

R. Müller-Mellin, H. Kunow, V. Fleißner, et al. Costep - comprehensive suprathermal and energetic particle analyser. *Solar Physics*, 162:483–504, December 1995.

K. Nakamura and Particle Data Group. Review of Particle Physics. *Journal of Physics G Nuclear Physics*, 37(7):075021, July 2010. doi: 10.1088/0954-3899/37/7A/075021.

R. Nymmik. Relationships among solar activity SEP occurrence frequency, and solar energetic particle event distribution function. *International Cosmic Ray Conference*, 6:280, 1999.

E. Parker. Extension of the Solar Corona into Interplanetary Space. *J. Geophys. Res.*, 64:1675–1681, November 1959. doi: 10.1029/JZ064i011p01675.

E. N. Parker. Dynamics of the Interplanetary Gas and Magnetic Fields. *Astrophys. J.*, 128:664, November 1958. doi: 10.1086/146579.

E. N. Parker. The passage of energetic charged particles through interplanetary space. *Planetary Space Science*, 13:9–49, January 1965. doi: 10.1016/0032-0633(65)90131-5.

P. Picozza, A. M. Galper, G. Castellini, et al. PAMELA A payload for antimatter matter exploration and light-nuclei astrophysics. *Astroparticle Physics*, 27:296–315, April 2007. doi: 10.1016/j.astropartphys.2006.12.002.

M. S. Potgieter. Solar modulation of cosmic rays. *Living Rev. Solar Phys.*, 10(3), 2013. doi: 10.1007/lrsp-2013-3. URL www.livingreviews.org/lrsp-2013-3.

M. S. Potgieter, E. E. Vos, M. Boezio, et al. Modulation of Galactic Protons in the Heliosphere During the Unusual Solar Minimum of 2006 to 2009. *Solar Phys.*, 289:391–406, January 2014. doi: 10.1007/s11207-013-0324-6.

E. Quémerais and P. Lamy. Two-dimensional electron density in the solar corona from inversion of white light images - Application to SOHO/LASCO-C2 observations. *Astron. Astrophys.*, 393:295–304, October 2002. doi: 10.1051/0004-6361:20021019.

D. V. Reames. Energetic particles from solar flares and coronal mass ejections. In R. Ramaty, N. Mandzhavidze, and X.-M. Hua, editors, *American Institute of Physics Conference Series*, volume 374 of *American Institute of Physics Conference Series*, pages 35–44, June 1996. doi: 10.1063/1.50970.

D. V. Reames. Particle acceleration at the Sun and in the heliosphere. *Space Sci. Rev.*, 90:413–491, October 1999. doi: 10.1023/A:1005105831781.

D. V. Reames. Solar Release Times of Energetic Particles in Ground-Level Events. *Astrophys. J.*, 693:812–821, March 2009a. doi: 10.1088/0004-637X/693/1/812.

D. V. Reames. Solar Energetic-Particle Release Times in Historic Ground-Level Events. *Astrophys. J.*, 706:844–850, November 2009b. doi: 10.1088/0004-637X/706/1/844.

D. V. Reames. The Two Sources of Solar Energetic Particles. *Space Sci. Rev.*, 175: 53–92, June 2013. doi: 10.1007/s11214-013-9958-9.

I. G. Richardson, G. Wibberenz, and H. V. Cane. The relationship between recurring cosmic ray depressions and corotating solar wind streams at $\leqslant$ 1 AU: IMP 8 and Helios 1 and 2 anticoincidence guard rate observations. *J. Geophys. Res.*, 101:13483–13496, June 1996. doi: 10.1029/96JA00547.

T. Sanuki, M. Motoki, H. Matsumoto, et al. Precise Measurement of Cosmic-Ray Proton and Helium Spectra with the BESS Spectrometer. *Astrophys. J.*, 545: 1135–1142, December 2000. doi: 10.1086/317873.

M. A. Shea and D. F. Smart. A summary of major solar proton events. *Solar Physics*, 127(2):297–320, 1990. ISSN 1573-093X. doi: 10.1007/BF00152170. URL http://dx.doi.org/10.1007/BF00152170.

Y. Shikaze, S. Haino, K. Abe, et al. Measurements of 0.2 20 GeV/n cosmic-ray proton and helium spectra from 1997 through 2002 with the BESS spectrometer. *Astroparticle Phys.*, 28:154–167, September 2007. doi: 10.1016/j.astropartphys.2007.05.001.

H. Sierks. *Kosmische Teilchen im Sonnensystem - Messung geladener Teilchen mit dem Kieler Instrument EPHIN an Bord der SOHO-Raumsonde - Ideal und Wirklichkeit*. Phd thesis, Christian-Albrechts-Universität zu Kiel, 1997.

A. Skutlartz and S. Hagmann. Triple-differential probabilities for the emission of δ electrons in 10-mev f^{q+} + Ne($q = 6, 8, 9$). *Phys. Rev. A*, 28:3268–3276, Dec 1983. doi: 10.1103/PhysRevA.28.3268. URL http://link.aps.org/doi/10.1103/PhysRevA.28.3268.

E. C. Stone, A. M. Frandsen, R. A. Mewaldt, et al. The Advanced Composition Explorer. *Space Sci. Rev.*, 86:1–22, July 1998. doi: 10.1023/A:1005082526237.

E. C. Stone, A. C. Cummings, F. B. McDonald, et al. Voyager 1 Explores the Termination Shock Region and the Heliosheath Beyond. *Science*, 309:2017–2020, September 2005. doi: 10.1126/science.1117684.

E. C. Stone, A. C. Cummings, F. B. McDonald, et al. An asymmetric solar wind termination shock. *Nature*, 454:71–74, July 2008. doi: 10.1038/nature07022.

E. C. Stone, A. C. Cummings, F. B. McDonald, et al. Voyager 1 Observes Low-Energy Galactic Cosmic Rays in a Region Depleted of Heliospheric Ions. *Science*, 341:150–153, July 2013. doi: 10.1126/science.1236408.

J. D. Sullivan. Geometrical factor and directional response of single and multi-element particle telescopes. *Nuclear Instruments and Methods*, 95:5, 1971. doi: 10.1016/0029-554X(71)90033-4.

N. Thakur, N. Gopalswamy, H. Xie, et al. Ground Level Enhancement in the 2014 January 6 Solar Energetic Particle Event. *ArXiv e-prints*, June 2014.

N. Thakur, N. Gopalswamy, P. Mäkelä, et al. Two Exceptions in the Large SEP Events of Solar Cycles 23 and 24. *Solar Phys.*, 291:513–530, February 2016. doi: 10.1007/s11207-015-0830-9.

S. C. Tripathi, P. A. Khan, A. M. Aslam, et al. Investigation on spectral behavior of Solar transients and their interrelationship. *Astrophys. Space Sci.*, 347:227–233, October 2013. doi: 10.1007/s10509-013-1519-x.

I. G. Usoskin, G. A. Bazilevskaya, and G. A. Kovaltsov. Solar modulation parameter for cosmic rays since 1936 reconstructed from ground-based neutron monitors and ionization chambers. *Journal of Geophysical Research (Space Physics)*, 116:A02104, February 2011. doi: 10.1029/2010JA016105.

R. Vainio, E. Valtonen, B. Heber, et al. The first SEPServer event catalogue ˜68-MeV solar proton events observed at 1 AU in 1996-2010. *Journal of Space Weather and Space Climate*, 3(27):A12, March 2013. doi: 10.1051/swsc/2013030.

A. Vogt, P. Dunzlaff, B. Heber, et al. Jovian Electrons In The Inner Heliosphere: A Parameter Study On Intensity Profiles Near Earth. In *34th International Cosmic Ray Conference (ICRC2015)*, volume 34 of *International Cosmic Ray Conference*, page 207, July 2015.

T. T. von Rosenvinge, D. V. Reames, R. Baker, et al. The High Energy Telescope for STEREO. *Space Sci. Rev.*, 136:391–435, April 2008. doi: 10.1007/s11214-007-9300-5.

B.A. Weaver and A.J. Westphal. Energy loss of relativistic heavy ions in matter. *Nuclear Instruments and Methods in Physics Research Section B: Beam Interactions with Materials and Atoms*, 187(3):285 – 301, 2002. ISSN 0168-583X. doi: http://dx.doi.org/10.1016/S0168-583X(01)01143-0. URL http://www.sciencedirect.com/science/article/pii/S0168583X01011430.

D. F. Webb and T. A. Howard. Coronal Mass Ejections: Observations. *Living Reviews in Solar Physics*, 9:3, December 2012. doi: 10.12942/lrsp-2012-3.

W. R. Webber and J. A. Lockwood. Characteristics of the 22-year modulation of cosmic rays as seen by neutron monitors. *J. Geophys. Res.*, 93:8735–8740, August 1988. doi: 10.1029/JA093iA08p08735.

T. Wiengarten, J. Kleimann, H. Fichtner, et al. Cosmic Ray Transport in Heliospheric Magnetic Structures. I. Modeling Background Solar Wind Using the CRONOS Magnetohydrodynamic Code. *Astrophys. J.*, 788:80, June 2014. doi: 10.1088/0004-637X/788/1/80.

J. P. Wild, S. F. Smerd, and A. A. Weiss. Solar Bursts. *Annual Review of Astron and Astrophys*, 1:291, 1963. doi: 10.1146/annurev.aa.01.090163.001451.

L.-L. Zhao and G. Qin. An observation-based GCR model of heavy nuclei: Measurements from CRIS onboard ACE spacecraft. *Journal of Geophysical Research (Space Physics)*, 118:1837–1848, May 2013. doi: 10.1002/jgra.50235.

ACKNOWLEDGMENTS

ERKLÄRUNG

Ich versichere an Eides Statt, dass ich die vorliegende Dissertation in Form und Inhalt eigenständig angefertigt habe. Abgesehen von der Beratung durch meine Betreuer und der angegebenen Literatur wurde die Arbeit ohne fremde Hilfe erstellt. Ich versichere, dass ich keine andere als die angegebene Literatur verwendet habe. Diese Versicherung bezieht sich auch auf alle in dieser Arbeit enthaltenen Grafiken und bildlichen Darstellungen.

Die Arbeit als Ganzes wurde bisher keiner anderen Prüfungsbehörde vorgelegt. Teile der Arbeit wurden bereits in Fachzeitschriften veröffentlicht und sind als solche gekennzeichnet. Die Quellennachweise der in den einzelnen Veröffentlichungen referenzierten Inhalte finden sich in der jeweiligen Veröffentlichung selbst und werden nicht zusätzlich im Quellennachweis dieser Arbeit aufgeführt. Für das Einbinden der Veröffentlichungen in diese Arbeit wurde die ausdrückliche Genehmigung der publizierenden Fachzeitschrift eingeholt.

Ich erkläre abschließend, dass die Arbeit unter Einhaltung der Regeln guter wissenschaftlicher Praxis der Deutschen Forschungsgemeinschaft entstanden ist.

Kiel, Oktober 2017

<div style="text-align: right">

Patrick Kühl

</div>